A COMBINED CFD AND STRUCTURAL ANALYSIS OF BLOOD FLOW IN PATHOLOGIC AORTIC GEOMETRIES

DIPLOMA THESIS

Submitted for achievement of the degree

Diplom-Ingenieur (Dipl.-Ing.)

under guidance of

Univ.-Prof.Dr. techn. H. Schima[1,2]

Univ.-Prof.Dr. techn. H. Kuhlmann[3]

Univ.-Prof.Dr. techn. J. Aiginger[4]

[1]Center for Medic. Physics and Biomed. Eng., Dept. of Cardiac Surg., Med. Univ. of Vienna, Austria
[2]Ludwig-Boltzmann-Cluster for Cardiovascular Surgery
[3]Department of Fluid Mechanics and Heat Transfer, TU Vienna, Austria
[4]Institute of Atomic and Subatomic Physics, TU Vienna, Austria

handed in at the

Vienna University of Technology

Faculty of Physics

Institute of Atomic and Subatomic Physics

by

Daniel Fechtig

Alois Fischill Straße 7

4540 Pfarrkirchen

Austria

Vienna, April 2011

Abstract

It is known from clinical practice that stenotic bicuspid aortic valves (BAV) are frequently associated with DeBakey Type I aortic dissections. Beside eventual histopathologic reasons, biomechanical causes are considered as potential reason. We investigated the potential effects of the disturbed flow field on the aortic wall by CFD simulation.

Methods: Pulsatile blood flow distribution through the human aorta at rest and exercise was numerically assessed for normal valves and different BAV configurations, together with 3 sizes of aortic dissected layers. A stiff model of the ventricular outflow tract, the open valve and the aortic arch was digitized with 1.5mio cells. Newtonian conditions were assumed, using the Transition-SST-k-ω-solver of ANSYS®. Besides global hemodynamic values, jet velocity, wall pressure, wall shear stress and ram pressure within the dissected area were calculated. Subsequently, a comparative durability approval analysis and assessment of potential dissection force based on predicted blood pressure values and incremental solutions of generalized Hooke´s law of elasticity is discussed in context with aortic failure stress data.

Results: Whereas a normal AV provides systolic jet velocities of 1.2m/s, wall pressures of only 117mmHg and a ram pressure of less than 8mmHg, BAV with an opening relation of 21:6mm show systolic jet velocities of 4.4m/s, wall pressures of 160mmHg and ram pressures of up to 45mmHg ram pressure at the ascending aorta proximal of the brachiocephalic trunk. This resulted e.g. in a pulsatile peak force of 0,288N on the delaminated wall layer of an assumed size of 48mm^2. For the normal AV, this force would be only 0,051N. Comparison of quantitative interrelations between physiologic and increased aortic wall stress with tissue weakening processes reveal significantly increased risk of dissection.

Conclusion: The increase of jet velocity caused by stenotic BAV leads to a significantly increased wall pressure and ram pressure, which may be a cause or at least a promoting factor of development and propagation of ascending aortic dissection.

Zusammenfassung

Zahlreiche klinische Studien belegen durch das gemeinsame gehäufte Auftreten einen kausalen Zusammenhang zwischen stenosierten bikuspidalen Aortenklappen und DeBakey Typ I Aortendissektionen. Neben histo-pathologischen Faktoren werden eventuelle biomechanische Gründe als potentielle Auslöser dieser
Krankheit angenommen. Mit Hilfe von numerischen CFD Simulationen untersuchten wir potentielle Effekte des durch die Klappenstenose veränderten Strömungsfeldes auf die Aortenwand.

Methoden: Das pulsatile Geschwindigkeitsfeld der Blutströmung durch die menschliche Aorta in Ruhe und unter Arbeitsbedingungen wurde numerisch für normale Klappen und verschiedene Typen von bikuspidalen Aortenklappen zusammen mit 3 verschiedenen Größen von Aortendissektionen simuliert. Ein steifes Modell des links-ventrikulären Ausflusstrakts, der jeweils offenen Klappe und des Aortenbogens wurde durch ein Netz mit ca. 1.5Mio Zellen diskretisiert. Das Blut wurde als Newtonsche Flüssigkeit approximiert, Turbulenz wurde mit Hilfe des Transition-SST-k-ω-Solvers von ANSYS® modelliert. Neben globalen hemodynamischen Observablen wurden die Geschwindigkeit des Blut-Jets, Wanddruck, Wandschubspannung und der Staudruck zwischen den bereits dissektierten Arterienlamellen berechnet und visualisiert. Anschließend wurde basierend auf den berechneten Druckwerten unter Ausnutzung des generalisierten Hooke´schen Gesetzes mit Hilfe einer inkrementellen Prozedur eine vergleichende Festigkeitsüberprüfung der Aortenwand und unter Zuhilfenahme von elementaren hydrostatischen Überlegungen die potentielle Dissektionskraft auf die verschieden großen Lamellen durchgeführt um diese dann im Kontext mit experimentellen Materialversagenswerten diskutieren zu können.

Resultate: Normale Aortenklappen erreichen systolische Blutgeschwindigkeiten von ca. 1.2m/s, Wanddrücke von 117mmHg und Staudrücke welche allesamt nicht größer als 8mmHg werden, stenosierte bikuspidale Aortenklappen mit einem ellipsoiden Öffnungsverhältnis von 21:6mm hingegen belasten die Wand der aorta ascendens proximal des truncus brachiocephalicus mit systolischen Jets von bis zu 4.4m/s, Wanddrücken um 160mmHg und Staudrücken bis zu 45mmHg. Das Resultat im bikuspidalen Fall sind pulsatile Kraftspitzen von 0.288N auf die delaminierten Wandschichten mit einer Fläche von 48mm^2. Im Falle normaler Aortenklappen fallen die Kraftspitzen mit 0,051N deutlich geringer aus. Ein Vergleich zwischen quantitativen und qualitativen Zusammenhängen zwischen physiologischen und pathologischen Wandspannungen mit belastungsinduzierten Ermüdungserscheinungen der Aortenwand lässt ein signifikant erhöhtes Dissektionsrisiko der Aortenwand im bikuspidalen Fall vermuten.

Schlussfolgerungen: Die durch stenosierte bikuspidale Aortenklappen verursachte erhöhte Strömungsgeschwindigkeit des Blutes führt zu signifikant erhöhten Wanddrücken und Staudrücken, was mit hoher Wahrscheinlichkeit die Ursache, zumindest aber einen begünstigenden Faktor bei Bildung und Vergrößerung von Dissektionen der aorta ascendends darstellt.

Danksagungen

> Für die Zukunft ist es wichtig, stärker als bisher, gemeinsam vorzugehen und sich gegenseitig zu unterstützen und zwar auf europäischer, nationaler, regionaler und natürlich auf persönlicher Ebene.
>
> Liese Prokop
> *Internationaler Landfrauentag 2002*

Es gibt Ereignisse im Leben, die einem Menschen völlig unerwartet begegnen. Oftmals sind dies erfreuliche Dinge, die unser Leben eine gewisse Zeit lang bereichern, oft sind es Tragödien die uns vor vermeintlich unlösbare Probleme stellen. Abseits von diesen relativen Ereignissen gibt es aber den für viele unerwarteten Tod, absolut und unumkehrbar.

Obiges Zitat habe ich aus zweierlei Gründen dieser Danksagung vorangestellt: Die ehemalige Weltklasseleichtathletin und österreichische Politikerin Liese Prokop starb völlig unerwartet und ohne warnende Vorzeichen an einem Riss der Aorta. In Prokop´s Rede am Landfrauentag 2002 spricht sie von 'gemeinsam vorgehen'. Transkribiert in die Sprache der modernen Wissenschaft bedeutet das nichts anderes als 'Interdisziplinäre Forschung'. Ich bin fest davon überzeugt, dass viele Probleme nur dann zu lösen sind, wenn man sie gemeinsam von vielen verschiedenen Seiten aus analysiert. Dies habe ich nicht zuletzt durch die teamorientierte interdisziplinäre Tätigkeit während meiner Diplomarbeit erkannt.

Ich möchte mich deshalb bei jenen Menschen bedanken, die mich während und nach des Verfassens der vorliegenden Arbeit unterstützt, motiviert und mit sanftem Druck angespornt haben. Diese Menschen haben mir auch dabei geholfen, den zukünftigen beruflichen Weg zu erkennen, der ohne Zweifel in der interdisziplinären Forschungstätigkeit verlaufen wird. Es würde mich persönlich stolz machen, durch meine Fähigkeiten einen Beitrag zur besseren Früherkennung und Vorhersage von lebensgefährdenden Krankheiten liefern zu können.

Ein ganz besonderer Dank gilt meinen Betreuern Prof. Heinrich Schima, Prof. Hendrik Kuhlmann und Prof. Johannes Aiginger, die mir die Möglichkeit gegeben haben, diese interdisziplinäre Arbeit am Zentrum für Medizinische Physik und Biomedizinische Technik durchzuführen und mich dabei in vielen Belangen wertvoll unterstützt haben.

Die gesamte Software und Hardware, sowie der Arbeitsplatz zur Strömungsberechnung wurden von der Research Group on Cardiovascular Dynamics and Artificial Organs unter der Leitung von Herrn Prof. Schima zur Verfügung gestellt. Schon zu Beginn meiner Arbeit wurde ich dort aufs freundlichste in das Team eingebunden. Dies gab mir die Möglichkeit, vom großen Know-how der Arbeitsgruppe zu profitieren.

Ein offenes Ohr für Fragen aus Gebieten der numerischen Strömungsmechanik fand ich während des Dissertantenseminars am Department of Fluid Mechanics and Heat Transfer, unter der Leitung von Herrn Prof. Kuhlmann.

Da es sich nicht rein um ein Thema der physikalischen Methoden in der Medizin handelte, möchte ich Herrn Prof. Aiginger danken, der die Betreuung trotzdem übernommen hat, in der sicheren Gewissheit, dass dies die Begutachtung und Beurteilung um ein gutes Stück

erschweren wird. Kritik und Lob während der Gespräche mit ihm werde ich mir gewissenhaft zu Herzen nehmen und nicht vergessen.

Never change a winning team! Marcus Granegger, Christoph Wirrmann, Thomas Schlöglhofer, Philipp Aigner, Francesco Moscato, Matthias Arras, Michael Baumann, Johann Horvat, Zeno Deckert, Verena Gschlad, Martin Stoiber and Christian Grasl werde ich als Kollegen und Freunde nicht vergessen. Neben der vitalen Zusammenarbeit am Institut möchte ich mich auch für die abwechslungsreiche Freizeitgestaltung mit ihnen bedanken.

Vielen Dank an Prof. Wolfgang Birkfellner für die gemeinsamen Rennradtouren nach Tulln.

Danke an meine Freundin, an meine Familie und meine Freunde, die mir den nötigen Ausgleich zum Studium geboten haben und mich mit ihrer Geduld und positiven Energie, ihren motivierenden Worten und bedingungslosen Unterstützung inspiriert haben. Ich habe euch sehr viel zu verdanken!

Contents

1. Introduction

1.1. Introduction english

Two of the major supporting mechanisms of human life are mainly determined by fluid flow: The mechanism of breathing (compressible fluid flow) and blood flow (incompressible fluid flow). The latter is responsible for maintaining a physiologic inner milieu of the human organism and serves as the main transport mechanism of breathing gases (oxygen, carbon dioxide and nitrogen) and nutrients to every corner of the body. Dysfunctions, malformations and diseases of the arterial system are therefore unintermideately responsible for severe physical and mental nuisances and not uncommonly lead to sudden death. Aortic dissection, with a suggested incidence of 2.6-3.5 cases per 100000 persons per year [35] is communicated as one of the most lethal one, since it almost inevitably leads to death shortly after it´s first break out. Among others (long-standing arterial hypertension, connective tissue disorders, vascular inflammation, trauma, iatrogenetic factors), bicuspid aortic valve disease is frequently reported to be a major predisposing factor of aortic dissection [16,17,19].

The severity of impact and the sudden occurance without former symptomes shows the importance of causal predictability, to allow clinicians prudence surgery. A deeper understanding of the underlying mechanism of dissection formation would firstly help researchers in the field of cardiovascular surgery techniques to develope functionally specified and safer geometries for heart valve implantations and arterial wall replacements and would secondly give clinical guidance on how valve implantations and arterial wall replacements should be positioned to achieve optimized durability. The discussion among causal underlying mechanisms causing aortic dissection is still speculative and controversial. Some investigators are convinced of genetic (histopathologic) reasons, others believe that altered hemodynamics influence regional wall mechanics and lead to tissue disintegration. Such definite positions between different opinions frequently lead to nothing more than obscured statements.

I am convicted that interdisciplinary research would most probably lead to a better understanding of how things are going on. As it can be seen in observations of public incidence, a nearly infinite variety of boundary conditions may lead to a single, well defined disease. Accordingly, a wide range of different views onto a disease would be required to gain more insight into it´s determining mechanism. One of these views, including hemodynamics and structural mechanics, is article of this study.

Actual clinical observations [69] showed, that DeBakey Type I dissection (ascending aortic dissection) is frequently concomitant with stenotic bicuspid aortic valve (BAV) disease. The aim of this study is to show, whether altered hemodynamics resulting from the stenotic orifice area are predisposing the ascending aortic wall for aortic dissection, or not.

To obtain a quantitative and qualitative statement, two major questions have to be an-

swered: how the aortic dissection develops and how it finally propagates. The former may be answered by observations of altered fluid flow characteristics at the ascending aortic wall, a subsequent stress and strain analysis for the aortic wall and linkage to weakening mechanisms of aortic tissue. From a fluid dynamical standpoint, propagation of aortic dissections can only be determined by sufficiently high ram pressures between the dissected layers. Therefore, quantification of ram pressures in already dissected aortic geometries may answer the latter.

The first step towards accomplishing the preliminary stated goals was to assess the hemodynamic properties of aortic flow in physiologic and pathologic conditions which probably are responsible for structural damaging of aortic tissue by computational fluid flow prediction (CFD). Pulsatile blood flow was predicted within different Type I-dissected and non-dissected (healthy) aortic models with non-stenotic completely open, Type 0 lateral, Type 0 anterior-posterior and Type 1 L/R [7] bicuspid aortic valve disease.

The development of aortic dissection was then investigated by performing a stress-strain analysis based on incremental generalized elastic theory. An accelerated weakening process due to regionally elevated aortic wall stress could be found by applying methods of long life fatigue testing used in mechanical engineering.

Elevated ram pressures between the already dissected medial layers caused by high systolic velocity jets found in all stenotic bicuspid aortic valve models where used to calculate forces which tend to tear the dissected layers further apart.

Chapter 2 and 3 provide an overview of continuum mechanics (fluid and structural dynamics) and the mechanisms of blood circulation in the human body. An emphasize lies on the linkage and interaction between physiologic/pathophysiologic processes and physical laws.

Chapter 4 (and partially appendix E) outlines basic principles and methodologies of the methods (CFD, durability approval) used within the thesis. The primary goal was to provide a well-structured practical and theoretical manual of the CFD workflow for future investigations.

The predicted velocity fields, pressure distributions and wall shear stress distributions at rest and exercise and the findings based on durability approval, long life fatigue testing and ram pressure calculations for a variety of aortic geometries can be found in Chapter 5 and appendix E.

At this point it should be mentioned, that every simplified model of nature has strictly limited validity and significance. A major aim of each person designing models should therefore be to honestly clarify and state the whole spectrum of limitations and errors. Honest models, as simply as they may be, can help to understand how nature behaves or not behaves.

1.2. Introduction german

Zwei der Mechanismen, die für das menschliche Leben von essentieller Bedeutung sind, basieren hauptsächlich auf Strömungsphänomenen: Die Atmung (kompressible Strömung) und Blutzirkulation (inkompressible Strömung). Letztere zeichnet sich verantwortlich für die Aufrechterhaltung eines konstanten inneren Milieus im menschlichen Körper und dient zusätzlich dem Transport von Atemgasen (Sauerstoff, Kohlendioxid und Stickstoff) und Nährstoffen in jeden erdenklichen Winkel des Organismus. Fehlfunktionen, Fehlbildungen

und Krankheiten des arteriellen Systems führen deshalb unmittelbar zu schweren physischen und mentalen Schäden, schlimmstenfalls nicht selten aber zum plötzlichen Tod.

Innerhalb der manigfaltigen Erkrankungen des arteriellen Systems wird die Aortendissektion mit einer Inzidenz von ca. 2.6-3.5 Fällen pro 100000 Personen pro Jahr [35] als eine der gefährlichsten und desaströsesten eingestuft, da zwischen erstem Auftreten und dem meist unausweichlich eintretendem Tod der Betroffenen häufig nur wenige Sekunden oder Minuten vergehen. Neben allgemein diskutierten Risikofaktoren wie chronischer arterieller Bluthochdruck, Bindegewebserkrankungen, Traumata, iatrogenischen Faktoren werden häufig bikuspidale Aortenklappen als prädisponierende Faktoren in Zusammenhang mit Dissektionen der Aorta erwähnt [16,17,19].

Die erwähnte Schwere und das plötzliche Auftreten ohne warnende Vorzeichen zeigt, wie wichtig eine kausale Vorhersagbarkeit ist, um Klinikern eine vorbeugende Behandlung zu ermöglichen. Ein tieferes Verständnis der den Aortendissektionen zugrundeliegenden Mechanismen würde erstens Forschern im Bereich kardiovaskulärer Erkrankungen bei der Entwicklung hoch spezialisierter und sicherer Präventiv- und Operationstechniken helfen (künstliche Herzklappen zur Implantation, Implantation von künstlichem und körpereigenem Aortenwandersatz bei Aortenaneurysma und Aortenriss) und würde weiters Klinikern Anleitungen bieten, wie solche Techniken in vivo am besten appliziert und positioniert werden, um bestmöglichen Halt und Langlebigkeit zu gewährleisten.

Die äußerst spekulative und kontroversielle Diskussion bezüglich den kausalen Mechanismen, die letzlich zu einer ausgebildeten und lebensbedrohlichen Aortendissektion führen wird durch Argumente und Vermutungen zweier strikt getrennter Lager geführt. Manche Investigatoren sind überzeugte Verfechter von genetischer (histopathologischer) Prädisposition der Aortenwand, andere wiederum machen die veränderten hämodynamischen Verhältnisse und deren möglichen Effekt auf die arterielle Wandmechanik verantwortlich für eine für die Aortendissektion typische strukturelle Desintegration der verschiedenen Wandschichten (tunica intima, tunica media, tunica adventitia). Viele dieser Aussagen führen trotz oder gerade wegen ihrer klar definierten und eingeschränkten Positionen häufig zu nichts Anderem als einer Verdeckung der wahren Verhältnisse.

Deshalb bin ich persönlich überzeugt, dass interdisziplinäre Forschung zu einem besseren Verständnis einer großen Anzahl von Krankheiten führen würde. Was die Inzidenz und Varietät von Krankheiten in der Bevölkerung betrifft, so führt nicht selten eine nahezu undendlich große Manigfaltigkeit von Randbedingungen zu einer scharf definierten Pathologie. Es lässt sich deshalb unschwer erkennen, dass zur Determinierung aller einer Krankheit zugrundeliegenden Mechanismen auch möglichst viele verschiedene Sichtweisen herangezogen werden sollten. Eine dieser Sichtweisen, welche die globale und lokale Hämodynamik und Strukturmechanik einschließt ist Gegenstand der vorgelegten Arbeit.

Aktuelle klinische Studien [69] haben gezeigt, dass DeBakey Typ I Dissektionen (Dissektionen der aorta ascendens) so gut wie immer in Verbindung mit stenosierten bikuspidalen Aortenklappen auftreten. Das vorrangige Ziel dieser Arbeit ist es zu zeigen, ob die durch die stenosierte Aortenklappe veränderten Strömungsverhältnisse die Wand der aorta ascendens für Aortendissektionen prädispositionieren (oder dies nicht tun).

Um quantitative und qualitative Aussagen bezüglich dieser möglichen Zusammenhänge treffen zu können, müssen zwei grundlegende Fragen beantwortet werden: wie entsteht die

Aortendissektion und wie breitet sie sich anschließend aus. Die Entstehung der Dissektion könnte durch die Visualisierung der vorherrschenden Strömungsverhältnisse bzw. Druckverhältnisse, sowie einer anknüpfenden Festigkeitsanalyse (ähnlich den Untersuchungen zur Bauteilermüdung im Maschinenbau) der arteriellen Wandstruktur erklärt werden (auftretende Spannungen und Verformungen). Von einem rein strömungsmechanischen Standpunkt betrachtet, propagiert eine bereits entstandene Dissektion nur dann, falls der Staudruck zwischen den dissektierten Wandschichten hinreichend groß wird. Daher sollte es zur Beantwortung der Frage bezüglich der Ausbreitung der Dissektion genügen, die in den pathologischen Klappengeometrien auftretenden Staudrücke zu berechnen.

Der erste Schritt um die oben erwähnten Ziele zu erfüllen war es, die verschiedenen hämodynamischen Observablen und Eigenschaften der Blutströmung in der Aorta in physiologischen als auch in pathologischen Bedingungen unter Zuhilfenahme numerischer Lösungsstrategien (Computational Fluid Dynmamics CFD) vorherzusagen, da diese möglicherweise für die strukturelle Desintegration der Aortenwand verantwortlich sind. In verschiedenen Kombinationen von DeBakey Typ I-dissektierten und nicht-dissektierten Aortengeometrien mit einhergehenden Typ 0 lateral, Typ 0 anterior-posterior und Typ I L/R [7] bikuspidalen Aortenklappen wurde dazu die zeitlich aufgelöste pulsierende Strömung eines vollen Herzschlages simuliert.

Die Entstehung der Aortendissektion wurde anschließend mit Hilfe einer selbst entwickelten, auf der generalisierten linearen Elastizitätstheorie basierenden inkrementellen Spannungs-Verformungsberechnung untersucht. Die im pathologischen Fall lokal erhöhten Spannungs-Verformungswerte an der betroffenen Aortenwand beschleunigen (den rein strukturmechanischen Standpunkt betreffenden) Alterungs(-Ermüdungs)Prozess der arteriellen Struktur. Die durch den Hochgeschwindigkeits-Blut-Jet beträchtlich erhöhten Staudrücke zwischen den bereits dissektierten Lamellen der tunica media wurden in allen Geometrien mit stenosierten bikuspidalen Aortenklappen gefunden und wurden zur Berechnung von dynamischen Kraftspitzen, welche die dissektierten Media-Schichten weiter auseinander zu reißen trachten, herangezogen.

Kapitel 2 und 3 bieten einen Überblick über das weite Feld der Kontinuumsmechanik (Strömungslehre und Strukturdynamik) und die der Blutzirkulation zugrundeliegenden Mechanismen im menschlichen Organismus. Dabei liegt ein Hauptaugenmerk an der Sichtbarmachung der tiefen Wechselwirkung zwischen physiologisch/pathologischen Prozessen des Menschen und vermeintlich unbelebten physikalischen Gesetzmäßigkeiten.

Kapitel 4 (teilweise auch Appendix E) behandeln Prinzipien und das methodische Arbeiten der in dieser Arbeit verwendeten Methoden (CFD und Festigkeitsnachweis). Vor allem für zukünftige Applikationen und Forschungsarbeiten auf diesem Gebiet wurde primär darauf geachtet, die Ausführungen klar zu strukturieren, um zusätzlich ein praktisches und theoretisches CFD-Manual vorlegen zu können.

Die berechneten Geschwindigkeitsfelder, Druckverhältnisse und Wandschubspannungen in Ruhe und Arbeitsbedingungen, sowie alle aus der Festigkeitsanalyse (und Dauerfestigkeitsbetrachtung) erhaltenen Resultate für eine große Varietät von Aortengeometrien sind in Kapitel 5 und Appendix E zu finden.

Nach diesen einleitenden Betrachtungen und Überlegungen sollte erwähnt werden, dass ein einfaches Modell eines beliebig komplexen natürlichen Systems nur eine streng limitierte

Gültigkeit und Wertigkeit innehaben kann. Eines der größten und wichtigsten Ziele und Aufgaben jeder Person die solche Modelle zum Zwecke weiterer Forschung und Anwendung entwickelt ist daher die ehrliche Klassifikation, Beschreibung und Anführung des gesamten dem Modell innewohnenden Fehlerspektrums. Ehrliche Modelle, so einfach sie auch sein mögen, können durchaus einen gewissen Beitrag zum Verständnis der Natur beitragen.

2. Fundamentals of Continuum Mechanics: Fluid Dynamics

Continuum mechanics deals with matter at length scales large compared to the molecular and atomic scale. The microscopic features of matter are the underlying determiners of macroscopic characteristics. One example occurring in fluid dynamics is the description of viscous forces between fluid layers and the coefficient of elasticity in structure dynamics. Matter consists of molecules, molecules are a cluster of atoms. Describing the motion of a fluid or a solid on a microscopic scale would require solutions of all equations of motion of every single molecule (and also the equations for every single 2- body, 3- body, n- body interaction). To simplify this procedure of solving all discrete equations, a continuum approximation is applied on the matter (liquid or solid) of interest. If the number of molecules is large enough, mean values of all physical quantities (pressure, velocity, temperature,...) are built upon the discrete physical quantities of the single molecules. As long as the fluctuations in physical quantities of the single molecules are smaller than the precision one desires, this approximation holds true. Starting from empirically observable phenomenons and experiments in a macroscopic view, mathematical models for the mechanical behavior of matter are built.

2.1. Characteristics of Fluids

The microscopic theory of molecular forces describes the characteristics of liquids (e.g.: water, blood). These forces of molecular interaction are of electromagnetical nature, are strongly repulsive if the atoms are very close together, slightly attractive when they are away a little distance from each other and quickly die out when the distance between the atoms get´s larger [42]. The kinetic energy of the molecules depends on the temperature of matter (thermal oscillations of molecules). Since the total Energy ($E_{tot} = E_{pot} + E_{kin}$) of a system is a conserved quantity, it can be used to judge whether the state of matter is liquid, solid or gasous. In other words, the relation between the depth of the minimum of the potential energy between two molecules (binding energy) and the average kinetic energy due to thermal motion determines the state of matter. In fluid matter (containing liquids and gases), the minimum of the intermolecular potential is very shallow. So, the thermal motion of the molecules is able to overcome the forces of attraction between them. In contrast to a solid, molecules of liquids are not bound to each other. Therefore, molecules are able to move freely around in space. As a consequence, fluid deforms continously when a shear stress (external load) of any (small) magnitude is applied on it. Solids deform, but not continously as fluids do. Fluids 'flow'. An important characteristic arising from the thermal motion of the molecules is the viscosity of fluids (see appendix B). Additionally, fluids moisten walls

if comming in contact with them. Consequently, fluid motion stagnates at the interface between solid wall and fluid (no-slip condition at walls). Fluid viscosity and the ability to moisten walls are the main determiners of typical flow characteristics observable in every day life (and within this text). Important physical properties (with the units used throughout the text in parenthesis) of fluids are the temperature T (°C), density ρ (kg/m^2) and dynamic viscosity = first coefficient of viscosity η (Pa·s). Other properties can be found in [40].

2.2. Governing Equations of Fluid Flow

Since the behavior of fluids is described by the continuum hypothesis, the motion of a fluid can be determined exactly by the conservation laws of mass, momentum and energy, which can be stated in differential and in integral form.

2.2.1. Equation of Mass Conservation

Mass is a conserved quantity. If matter, i.e. a small amount of fluid flows away from a point, there must be a decrease in the amount that was left behind. Thus, a local time rate of change in the fluid´s density must strictly go along with an equal change of mass density flux in space. This physical principle called 'conservation of matter' get´s a clear mathematical form by relating the divergence of the flux of the fluid´s mass density $\rho\vec{v}$ to the local time-rate-of-change of fluid density:

$$\nabla \cdot (\rho\vec{v}) = -\frac{\partial\rho}{\partial t} \tag{2.1}$$

Here, ∇ stands for the vector operator 'del' which consists (in 3 dimensions) of the three spatial partial first derivatives. When operating on a vector field $\vec{v}$ (dot product), it yields a scalar quantity called divergence of the vector field. $\vec{v}$ denotes the velocity field of a certain volume of fluid. ρ in equation 2.1 and throughout this text represents the density of the observed fluid volume. In general, ρ will be dependent on time and the spatial coordinates $\vec{x} = (x_1, x_2, x_3)^T$ of the spacevector $\vec{x}$. For the special case of incompressible fluids, where ρ is a constant,this equation yields:

$$\nabla \cdot \vec{v} = 0 \tag{2.2}$$

That means, velocity $\vec{v}$ in incompressible fluid flow maintains divergence-free (no sources, no sinks) in the entire fluid volume.

2.2.2. Linear Momentum Equation

According to Newton´s law of motion (force density formulation), the time rate of change of momentum density of a fluid volume equals the sum of force densities acting on it:

$$\rho\vec{a} = \vec{f} \tag{2.3}$$

The forces acting on such a volume (see appendix B) are divided into surface forces (acting purely onto the surface of the fluid element by the surroundings through direct contact; they are proportional to the extent of the area on which they are acting; e.g. pressure forces and forces due to friction), volume forces (such as gravitational forces; they arise from an action at a distance without physical contact; they are resulting from a certain force field, e.g. the gravitational field or the magnetic field) and line forces (e.g. surface tension forces, appearing at the interface between liquid and gas). If surface forces are acting tangential to the surface, they usually are denoted as shear forces, in contrast to normal forces acting perpendicular to the surface. In fluid dynamics, acceleration $\vec{a}$ of the fluid volume on the left hand side of equation 2.3 is split into a local acceleration part and a convective acceleration part (see appendix B). Neglecting forces due to gravitation and electromagnetism, pressure forces and frictional forces (viscous forces) are the only forces determining the right hand side of equation 2.3. Thence, together with the fundamental principle of mass conservation, the momentum equation derived out of Newton´s second law of motion successfully describes the dynamical behavior of fluids in space and time. The incompressible formulation for Newtonian fluids (constant viscosity) reads:

$$\rho(\underbrace{\frac{\partial \vec{v}}{\partial t}}_{local\ acceleration} + \underbrace{(\vec{v} \cdot \nabla)\vec{v}}_{convective\ acceleration}) = - \underbrace{\nabla p}_{pressure\ force} + \underbrace{\eta \Delta \vec{v}}_{viscous\ force} \tag{2.4}$$

Equation 2.2 and equation 2.4 are also known as the 'Navier Stokes Equations' of incompressible fluid flow. A complete derivation of the governing equations of fluid flow is given in appendix B.

Special cases of flow situations (e.g.: steady flow, unsteady flow, laminar steady flow, inviscid steady flow, inviscid unsteady flow and circulatory flow) where particular terms in the Navier Stokes equations can be neglected due to physical reasoning are described in (appendix C). If the nonlinear term (convective acceleration) in $\vec{v}$ is not negligible small, a solution is only possible by numerical solving techniques [43]. According to the nonlinearity, small derivations in the boundary conditions of a flow problem can lead to completely different solutions of the governing equations of motion. The same situation arrises for example with the track of a single ball placed on top of a steep hill, which can be pushed lightly into it´s left side or either into it´s right side. Indeed, this small deviation in boundary condition leads to a completely different track of the ball. And so it is in fluid motion. Only a small elevation of a single parameter (e.g. velocity, density, viscousity of the fluid, diameter of the tube) alters a straight forward motion of the fluid particles into a swirling and chaotic motion. This chaotic motion caused by the nonlinear convective term is called turbulence, which occures only if the convective term get´s sufficient high in relation to the viscous forces of fluid motion. Turbulence emerges not because of a sudden change in geometry. The fundamental trigger of this irregular, chaotic motion has not been discovered until now. It is even unclear, whether a linear (laminar) motion switches smoothely or suddenly into a nonlinear, turbulent motion [38]. Experimentally checked first by Osborne Reynolds, the appearance of turbulence in flow of a straight long pipe (with constant radius of the pipe, constant density and viscousity of the fluid, burnished inner surface of the pipe) can be triggered by a slow and constant rising of the inlet velocity to a certain level. Moreover, the

appearance of turbulence is strongly related to the relation between pipe radius (R), density (ρ) and viscosity (η) of the fluid and average flow velocity (U). These parameters form the dimensionless Reynoldsnumber, which relates inertial forces (in a steady flow arising from convective acceleration) to frictional forces (viscous forces). The Reynolds number (among other dimensionless parameters) can be derived out of dimensional analysis (see appendix D) of the Navier Stokes equations:

$$Re \equiv \frac{URp}{\eta} \tag{2.5}$$

Critical values of Re associated with the transition of laminar to turbulent pipe flow are given in the next chapter, related to the discussion of arterial blood flow.

2.3. Governing Equations in a Cylindrical Coordinate Frame

In a cylindrical coordinate frame with position vectors defined by:

$$x = r\cos\theta,\ y = r\sin\theta,\ z \tag{2.6}$$

the incompressible Navier Stokes equations for Newtonian fluids (neglecting gravity) in vector element notation can be written as mass conservation:

$$\frac{\partial u}{\partial r} + \frac{1}{r}\frac{\partial v}{\partial \theta} + \frac{\partial w}{\partial z} + \frac{u}{r} = 0 \tag{2.7}$$

and momentum conservation:

$$\rho\left(\frac{\partial u}{\partial t} + u\frac{\partial u}{\partial r} + \frac{v}{r}\frac{\partial u}{\partial \theta} - \frac{v^2}{r} + w\frac{\partial u}{\partial z}\right) = -\frac{\partial p}{\partial r} + \eta\left[\frac{\partial}{\partial r}\left(\frac{1}{r}\frac{\partial}{\partial r}(ru)\right) + \frac{1}{r^2}\frac{\partial^2 u}{\partial \theta^2} - \frac{2}{r^2}\frac{\partial v}{\partial \theta} + \frac{\partial^2 u}{\partial z^2}\right] \tag{2.8}$$

$$\rho\left(\frac{\partial v}{\partial t} + u\frac{\partial v}{\partial r} + \frac{v}{r}\frac{\partial v}{\partial \theta} + \frac{uv}{r} + w\frac{\partial v}{\partial z}\right) = -\frac{1}{r}\frac{\partial p}{\partial \theta} + \eta\left[\frac{\partial}{\partial r}\left(\frac{1}{r}\frac{\partial}{\partial r}(rv)\right) + \frac{1}{r^2}\frac{\partial^2 v}{\partial \theta^2} + \frac{2}{r^2}\frac{\partial u}{\partial \theta} + \frac{\partial^2 v}{\partial z^2}\right] \tag{2.9}$$

$$\rho\left(\frac{\partial w}{\partial t} + u\frac{\partial w}{\partial r} + \frac{v}{r}\frac{\partial w}{\partial \theta} + w\frac{\partial w}{\partial z}\right) = -\frac{\partial p}{\partial z} + \eta\left[\frac{1}{r}\frac{\partial}{\partial r}\left(r\frac{\partial w}{\partial r}\right) + \frac{1}{r^2}\frac{\partial^2 w}{\partial \theta^2} + \frac{\partial^2 w}{\partial z^2}\right] \tag{2.10}$$

with radial velocity u, circumferential velocity v and longitudinal velocity w. The terms on the left hand side of equations 2.8, 2.9, 2.10 (multiplied by the density) represent inertial forces. All terms on the right hand side inbetween square brackets (multiplied by the viscousity constant) describe viscous forces. Partial time derivatives of u, v, w describe purely longitudinal (or respectively radial and circumferential) accelarations. When adjacent fluid laminae differ in longitudinal velocity (always the case in viscous fluid flow), radial motion of a particle necessarily brings about a change in longitudinal acceleration, indicated for example by $u(\partial w/\partial r)$. If for example (in pipe flow) the pipe tapers (the radius of the pipe decreases downstream), the convergence of the walls imposes a convective acceleration on all laminae, which is for example represented by the term $w(\partial w/\partial z)$ [22].

2.4. Integral Formulation of Governing Equations

The Integral form of the incompressible Navier Stokes equations for Newtonian fluids can be obtained by applying $\int_{C_V}(\ldots)dV$ onto equation 2.2 and equation 2.4. Mass conservation then reads:

$$\int_{C_V}(\nabla\cdot\vec{v})dV = 0 \underbrace{\Longleftrightarrow}_{Gauss\,divergence\,theorem} \int_{C_S}\vec{v}dS = 0 \tag{2.11}$$

The same procedure transforms the momentum equation in differential form (local form) into a integro-differential equation (IDE). Gauss divergence theorem can only be applied on pure divergence terms. Therefore, the convective term $(\vec{v}\cdot\nabla)\vec{v}$ in equation 2.4 must be transformed into $\frac{1}{2}\nabla\cdot(\vec{v}\vec{v})$ (this transformation is possible because: $(\vec{v}\cdot\nabla)\vec{v}+(\vec{v}\cdot\nabla)\vec{v} = \nabla\cdot(\vec{v}\vec{v}) \rightarrow \frac{1}{2}\nabla\cdot(\vec{v}\vec{v}) = (\vec{v}\cdot\nabla)\vec{v}$). After integration over the control volume C_V, the momentum equation looks like:

$$\int_{C_V}\rho\frac{\partial\vec{v}}{\partial t}dV + \int_{C_V}\rho\frac{1}{2}\nabla\cdot(\vec{v}\vec{v}) = -\int_{C_V}\nabla p + \int_{C_V}\eta\Delta\vec{v} \tag{2.12}$$

Gauss divergence theorem converts the integration over C_V of the convective term, the pressure force term and the viscous term into an integration over the control surface C_S:

$$\int_{C_V}\rho\frac{\partial\vec{v}}{\partial t}dV + \int_{C_S}\rho\frac{1}{2}\vec{v}\vec{v}d\vec{S} = -\int_{C_S}\nabla p d\vec{S} + \int_{C_S}\eta\nabla\vec{v}d\vec{S} \tag{2.13}$$

Equation 2.11 and equation 2.13 are those formulations of transport equations used in the finite volume method (FVM) described in section 4.1.

3. Circulation: Outline of Medical Terms and Linkage to Physics

First part of the subsequent chapter provides an overview of anatomical and physiological features of the human´s circulatory system. Especially the physiological characteristics of cardiovascular circulation are mainly determined by physical laws, which in turn are described linguistical, numerical (physical quantities), visual (pictorial schematics, diagrams,...) and mathematical (governing equations). As a foundation for understanding the mechanisms underlying the pathology of dissection formation and a golden thread for the succeeding discussion, the physiology of cardiovascular circulation is described by means of approved medical knowledge with embedded Hemodynamics and structural mechanics.

The second part comprises an exposition of the pathologies handled by this thesis, namely Bicuspid Aortic Valves (BAV), Aortic Valve Stenosis (AVS), Arterial Hypertension (AHT) and Aortic Dissection (AD). Articles of discussion are respective Definition, Incidence, Classification, Predisposing factors, Pathogenesis, Natural History, Manifestations, Diagnosis, Treatment and Prognosis. Main points of interest are the linkages between the pathologies and determining factors which can be examined within the methods (CFD, analytical stress calculation) used in this study.

The units of pressure used in the preceding chapter are $[p] = \text{Pa}$ and $[p] = \text{mmHg}$, conveniently written as $[p] = \text{Pa(mmHg)}$, where the value of pressure in pascal stands before the value of p in mm mercury. Some textbooks use $[p] = \text{dyn/cm}^2$, what makes a translation between the units imperative. $1329\,\text{dyn/cm}^2$ equal $1\,\text{mmHg}$ equal $133.32\,\text{Pa}$ at $21\,^\circ\text{C}$ or $70\,^\circ\text{F}$ (Fahrenheit). Blood flow is variantly expressed as volume moved per unit time ($[Q] = \text{cm}^3/\text{s}$ or $[Q] = \text{l/min}$ or $[Q] = \text{m}^3/\text{s}$) or described by it´s velocity ([v] = cm/s or [v] = m/s). Q (sometimes also written as the lowercase q) is used as a global quantity, whereas v frequently is used as a local quantity of blood flow. If not mentioned explicitly, length (l, L) and diameter (d, D) are always declared in meters (m), time (t, τ) in seconds (s), mass m in kilogram (kg), force F in Newton (N) and area (A, S) in squaremeters (m^2).

3.1. Anatomy, Physiology, Hemodynamics and Structural Mechanics of the Circulatory System

The cardiovascular system (see figure 3.1) as a closed dynamical system maintains a continuous movement of blood within the different organs of the human body. With blood as the main carrier medium of breathing gases, nutrients, cellular metabolites, water, electrolytes, acids and bases, heat, hormones, humoral and cellular components of the human´s immune

system, it serves as a transport system which properly distributes this vital substances within the body to buoy up the organism´s constant inner milieu (homoeostasis). The heart as the system´s pump loads blood into serially and paralelly switched vessels.

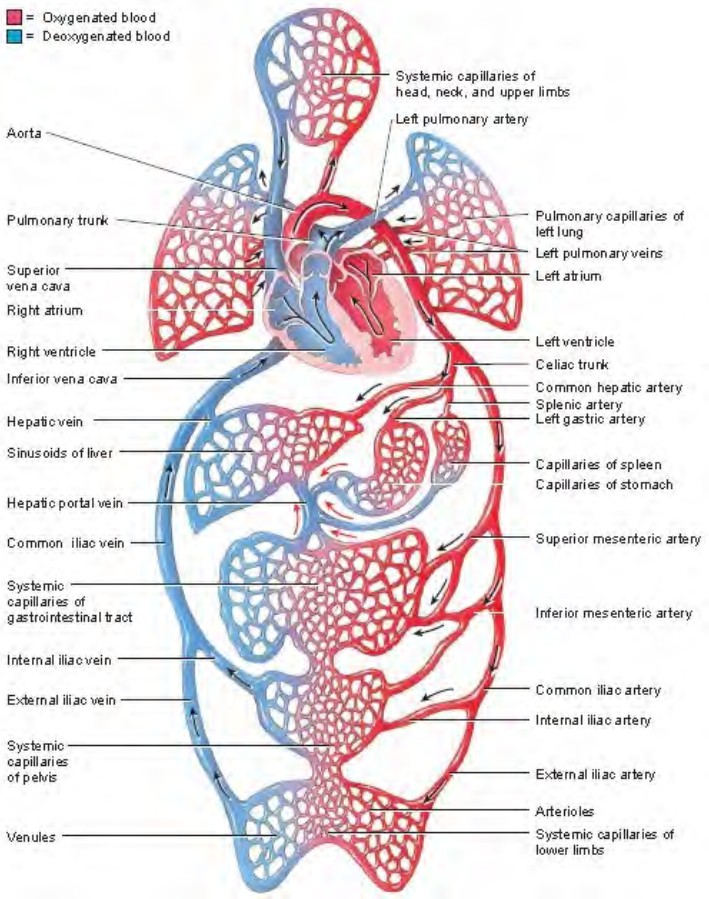

Figure 3.1.: Circulatory routes of the cardiovascular system. Long black arrows indicate the systemic circulation, short black arrows the pulmonary circulation [50].

Systemic Circulation (high pressure system): Oxygenated blood is distributed onto parallel switched vessels of organs by the left heart and subsequently the deoxigenated blood coming from the organs is injected into the right side of the heart.

Pulmonary Circulation (low pressure system): From the right heart, deoxigenated blood is transported to the lung and its system of vessels, where it get´s oxigenated and carried further to it´s origin - the left heart.

Vessels which carry blood away from the heart to the organs are denoted as arteries and more peripheral from the heart as small arteries, arterioles and capillaries. From the substitution of vital substances between blood and cells in the capillaries, downstream postcapillary vessels, namely venules, venoles, small veins and big veins officiate as transporter away from the organs back to the heart.

If not mentioned specifically, values in this chapter refer to the physiological (normal, healthy) state.

3.1.1. Transport Medium: Blood

Blood as a functional body tissue consists of cellular species (erythrocytes = red blood cells, leukocytes = white blood cells and thrombocytes) and plasma (contains proteins and electrolytes). Normal blood volume of 4-6 liters subsides during water removal and sweating (hypovolemia) and is elevated in highly trained endurance athlets (hypervolemia). Erythrocytes build up the main mass of cellular constituents of blood. They are responsible for O_2 transport, are involved in CO_2 transport and regulation of the blood´s pH-value. These functions are linked with the intra-erythrocytic red colorant hemoglobin. Morphological, red blood cells are round, biconcave and acaryote (pipless, no seed) discs (platelets), approximately 7.5 μm in diameter, 2 μm edge thickness and 1 μm central thickness. Elevation of hematocrit (volumetric fraction of erythrocytes in entire blood volume) in women (0.42) and men (0.47) can be caused by hyperproduction of hemoglobin (a chromoprotein, colorant of red blood cells). Polycythemia (elevated production of erythrocytes) and polyglobuly (elevated production of erythropoietin (EPO)) cause higher blood viscosity. A lowering of blood viscosity can be caused by anemia (underproduction of hemoglobin) [45]. Leucocytes are nucleated cells, functionally differenced as granulocytes, lymphocytes and monocytes, which all contribute to specific defense reactions in living organisms (e.g. defending bacteries, viruses) and acute inflammatory reactions. Thrombocytes play an important role in arrest of bleeding (hemostasis) of small blood vessels. In physiological conditions, they show nearly no reaction with the vessel´s endothelial layer, since the healthy glycocalyx of endothelial cells impedes adhesion to maintain a near-wall bounded seam of blood plasma. In case of small endothelial ruptures, thrombocytes adhere at the vessels endothelial wall, build up a reversible plateletaggregation and staunch the bleeding by forming a irreversible thrombocytic graft (primary hemostasis). In the ensuing secondary hemostasis, the endothelial coagulation system forms a fibrous net to ensure the stability of the formerly injured location.

Viscous Properties

A Newtonian fluid is characterized by constant viscosity (e.g.: water with η_w = 0.001 Pa·s at 20 °C, blood plasma with η_{bp} = 0.0011 - 0.0016 Pa·s) however large the strain rate dv/dr acting between the fluid layers may be. The governing equation of fully developed laminar flow in a straight cylindrical tube together with the relation of shear stress and strain rate of a Newtonian fluid results in an expression of shear stress determined by radius (r), length (L) of the tube and pressure difference (ΔP) between an upstream and a downstream location of the tube [22]:

$$\frac{dv}{dr} = -\frac{r(\Delta P)}{2L\eta} \tag{3.1}$$

$$\tau = \frac{F}{A} = \eta\frac{dv}{dr} \Rightarrow \tau = -\frac{r\Delta P}{2L} \tag{3.2}$$

The highest shear stresses are found at the vessel´s wall ($r = R$):

$$\tau_w = -\frac{R\Delta P}{2L} \tag{3.3}$$

which can also be expressed in terms of volume flow rate and average velocity of laminar flow [22]:

$$\frac{dv}{dr}|_{r=R} = \frac{4\bar{v}}{R} = \frac{4Q}{\pi R^3} \tag{3.4}$$

Blood is non- Newtonian (shear thinning), which means, that η decreases with increasing strain rates between the layers. η of blood gets approximately constant at high strain rates within tube diameters greater than 1 mm. At strain rates endemic in the ascending aorta (approx. 50 1/s), viscosity of blood at T = 37 °C is practically constant at a value of η_b = 0.003 - 0.004 Pa·s [22].

3.1.2. The Pump: Heart

By means of rhythmical relaxation phases(diastoles) and contraction phases (systoles) of it´s chambers (ventricles) and atria, the heart pumps blood coming from the veins into the arterial system. The heart overcomes the prevalent flow resistance in the cardiovascular pipework system by generation of sufficient ventricular and atrial pressures, to maintain a life supporting movement of blood.

Anatomy

The heart (depicted in figure 3.2) lies in the anterior inferior Region of the mediastinum, bounded on both sides by the exterior pleura branches of the lungs. Inferior it is bounded by

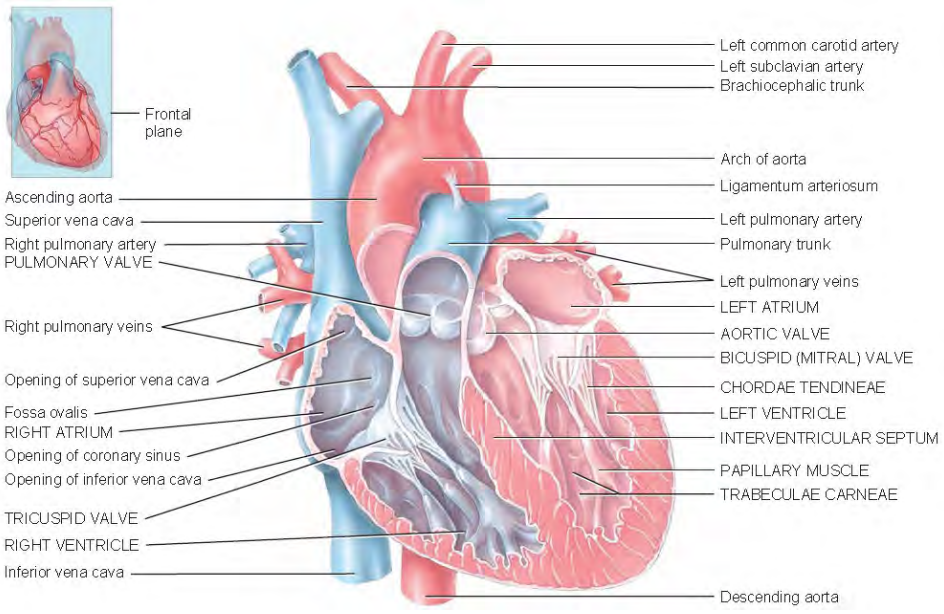

Figure 3.2.: The inner structure of the heart. Anterior view of frontal section [50].

the diaphragm, the anterior portion of the heart impinges onto the sternum and the rips. On the back (posterior) lies the esophagus (see figure 3.3). Geometrically, it looks a bit like a

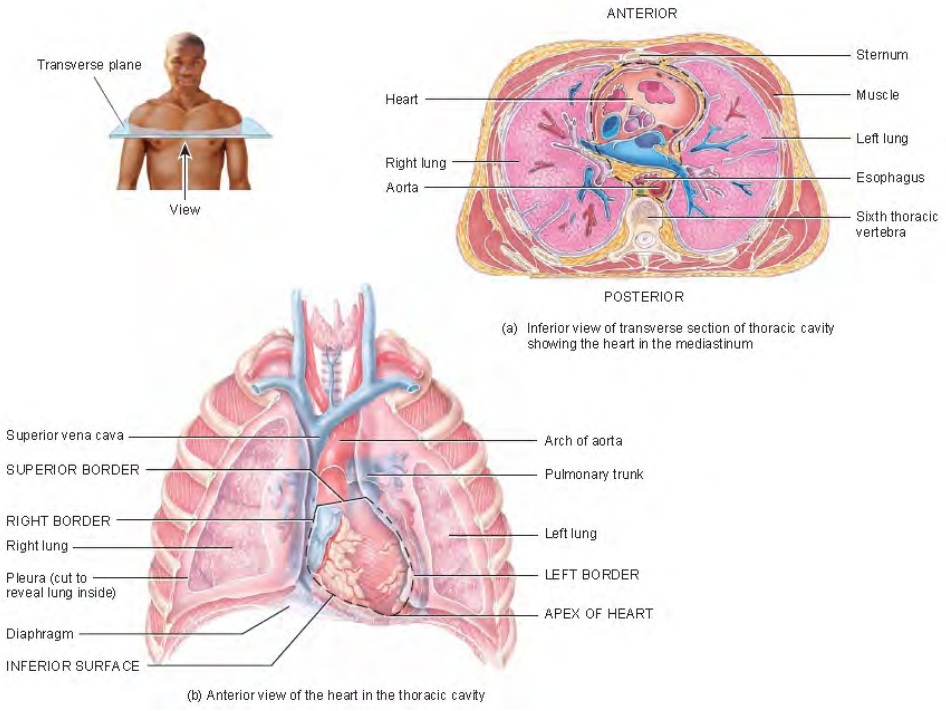

Figure 3.3.: Location of the heart within the human body [50].

more indifferent cone. The upper part is referred as the basis of the heart, whereas the lower part is defined as the cardiac apex or apex of the heart. The axis between the crossectional midpoint of the basis and the apex depicts slantwise to the bottom of the body. The wall as a trilaminate structure shows a variation in thickness within it´s four chambers due to the different functionality of atria and ventricles. The endocardium as a layer of endothelial cells placed over a lose layer of connective tissue plus stored elastic fibers and smooth muscle fibres overcasts the entire interior. The muscular myocardium lies in the middle and determines the contractile ability of the heart wall, whereas the epicardium builds up the outermost layer of the wall. The pericardium (pericardial sac) encases the heart and interconnects it with the surrounding.

Physiology

The functionality of the heart depends mainly on the rhythmic contraction and relaxation of the right atrium (RA), the right ventricle (RV), the left atrium (LA) and the left ventricle (LV). Within this mechanism, the RA is supplied with deoxigenated blood (coming from the organs) from the big caval veins (vena cava superior and vena cava inferior) and leads it to the RV. The RV pumps it into the lung artery (arteria pulmonalis) which transports it to the lung where it get´s oxigenated. The LA receives an oxigenated portion of blood from four pulmonary veins and conducts it further to the LV. Due to contraction of the left ventricle blood is ejected with high pressure into the aorta (biggest artery in humans). From the aorta, shortly after the aortic valve, two coronary arteries originate to supply the

heart muscle with oxigenated blood. Secondly, an integrated valve apparatus (figure 3.4) ensures, that blood flows into the right direction (backflow into the ventricle impinges the heart walls with extra load and would increase the burden carried by the trilaminate layerd wall). Valves are placed at each outflow and inflow orifice (ostium), namely the atrioventricular valves (AV valves) between LA - LV (designed out of two connective tissue membranes), between RA - RV (three connective tissue membranes) to ensure monodirectional inflow of blood into the ventricles and ventricular valves placed at the orifices of LV into the aorta (tricuspid aortic valve) and RV into the lung artery (pulmonary valve) to assure monodirectional outflow into the particular artery. During systole, AV valves close the ostium between

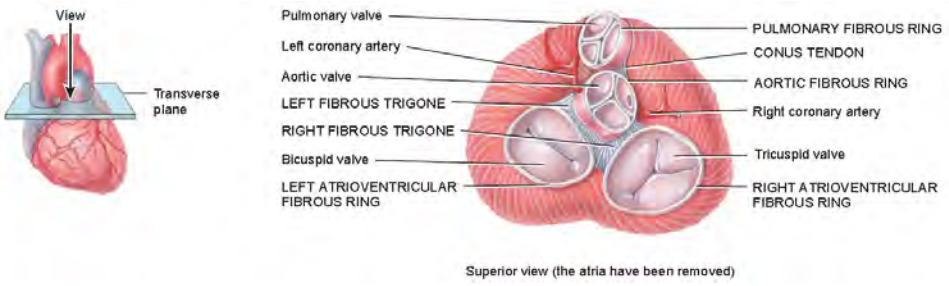

Figure 3.4.: Location and schematic anatomy of heart valves forming an integrated apparatus [50].

ventricle and atrium. During diastole, the two ventricular valves seal the ventricles from the arteries. Opening and closing of the valves is uniquely determined by pressure differences between atria and ventricles. Left heart (propelling the high pressure system) and right heart (propelling the low pressure system) are working (nearly) synchronous and follow the same working principle. A maximum pressure difference of ΔP = 16000 Pa (120 mmHg) - 400 Pa (3 mmHg) = 15600 Pa (117 mmHg) exists between left and right heart.

One overall beat of the left heart (LA and LV) is a cycle of four working steps with characteristic pressure - volume behavior (ECG, the pressure distribution, heart sounds and volume of the left ventricle during the phases of one heart beat are shown in figure 3.5). Systole begins with a short isovolumetric contraction period where AV valves and ventricular valves are closed. Due to the contraction, pressure rises quickly to a value which slightly exceeds diastolic aortic pressure ($p_{dA} \approx$ 10700 Pa (80 mmHg)), causing the aortic valve to open. The following ejection period begins with a continous elevation (Law of Laplace) of ventricular pressure up to a peak value ($p_{sLV} \approx$ 16000 Pa (120 mmHg)) and continues with a drop down of pressure until late systole. Within this period of auxobar contraction, the LV ejects about 70 ml oxigenated blood into the aorta (= stroke volume SV per heart beat). The physiological range of SV lies between 68 and 100 ml [22]. A blood volume of about 40-50ml resides in the LV (ejection fraction EF = Stroke volume SV/enddiastolic charge volume EV). End systole is reached, when pressure in the LV drops down to deceed aortic pressure, effect the aortic valve to close. The successive isovolumetric relaxation period of early diastole, where all valves are closed is characterised by a drop down of intraventricular pressure until a value of $p_{dLV} \approx$ 1200 Pa (9 mmHg) is reached. This value deceeds the prevalent pressure of the LA, causing the AV valves to open. The cycle closes with the subsequent filling period,

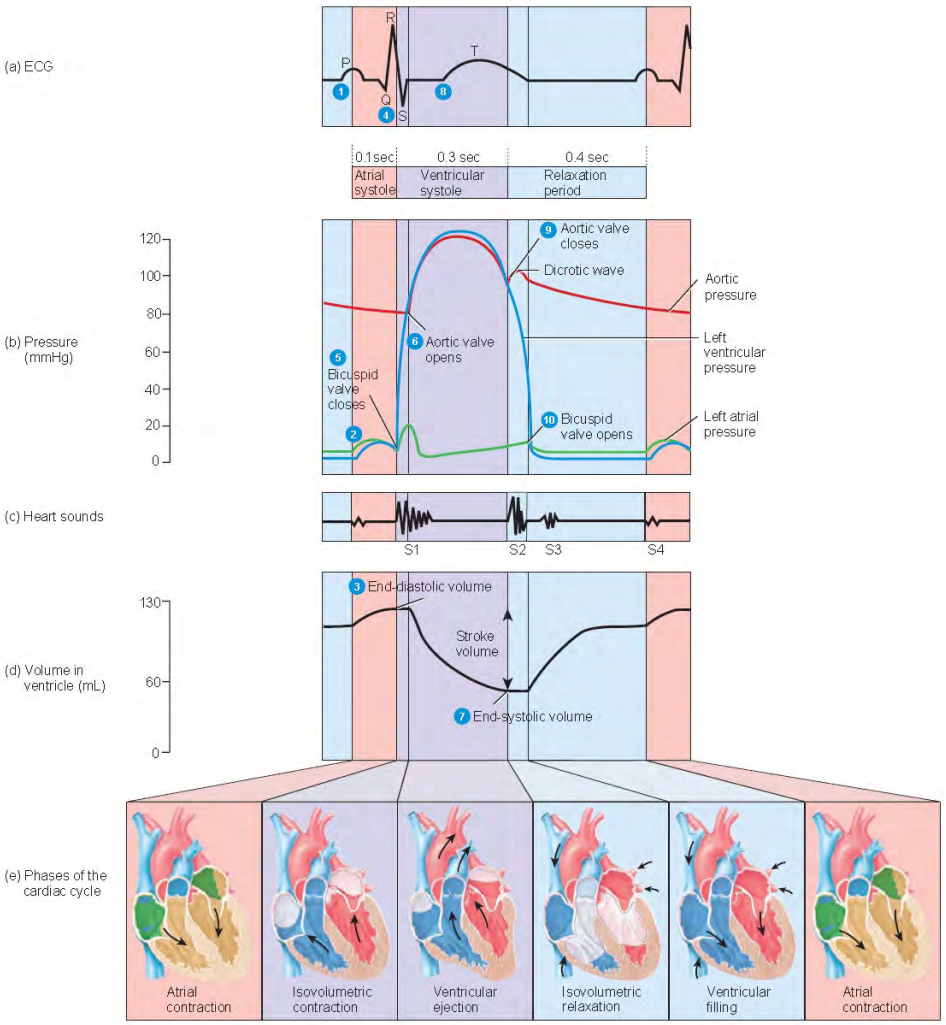

Figure 3.5.: Hemodynamic parameters within one overall beat of the left heart [50].

where oxigenated blood from the pulmonary veins is sucked into the LA. The four steps are embedded within short periods of atrial systole (atrial contraction).

The suitable contraction of atria and ventricles is controlled by an electrical stimulation system, where a autorhythmic electrical stimulus originating from self-stimulating cells - assembled in a zone called the sinoatrial node (Keith-Flack-Node) - propagates downward to the apex sequentially stimulating individual muscular segments. Approximately 60-70 times per minute (= pulse frequency of the heart at rest), an electrical pulse propagates from the sinus node over the atrioventricular node, via the bundle of his (which splits into two tawara branches) finally to the purkinje fibres, which continously disembogue into the fibres of the ventricular muscle.

Regulation of Heart Action

Since the electromechanical coupling is dependent on the concentration gradient of positive charged ions (Ca^{2+}, K^{+}) between the extracellular and intracellular matrix, an elevation of these constituents can cause a moderate heightening of both excitement and velocity of excitement. By far more important in influencing contractility and frequency of the otherwise widely autonomous organ is the innervation of the heart done by postganglionic sympathic and parasympathetic nervous fibers belonging to the automatic nervous system. This innervation can be either efferent or afferent. Efferent innervation modificates the heart´s contractile action for the purpose of accomplishing the requirements of the organism as a whole. This is gainable by influencing heart frequency, the duration of atrioventricular stimulation propagation and force of ventricular and atrial contraction. An activation of sympathic nerves (courier: noradrenaline or adrenaline) leads to an elevation of the parameters mentioned above, whereas an activation of parasympathic nerves (courier: acetylcholine) effects the opposite. Both, sympathic and parasympathic mechanisms, play a major role in regulating the characteristic of cardiac work and power in exercise conditions (sports, hard work). In resting conditions, a SV of 70 ml and a heart rate of 70 beats per minute result in a CO (= average volume of outflow from left ventricle per unit time) of 5 liters per minute. In man between an age of 16-60 years, CO is about 6.5 liters per minute with a standard deviation of 1.44 [22]. In exercise conditions, where all organs need to be supplied with more oxigenated blood, CO can undergo a massive boost. A CO of 25 liters per minute can be the case in extreme conditions. This elevation is mainly achieved by nerval stimulation (sympathic nerves) of ventricular contraction (twofold increase of SV) and a 2.5-fold acceleration of heart frequency. The peak slope in the pressure- time- distribution (dp/dt_{max}) can be consulted as a measure of LV contractility in the isovolumetric contraction phase. Sympathic activity enlarges the physiological slope ($dp/dt_{phys} \approx$ 1500 - 2000 mmHg/s). A 2.5-fold accelaration of frequency changes the ratio between systolic and diastolic duration from 1:2 at rest (isovolumetric contraction: 60 ms, auxobaric ejection: 210 ms, isovolumetric relaxation: 60 ms, ventricular filling: 500 ms) to 2:1 (e.g.: $\approx$ 50 ms, $\approx$ 190 ms, $\approx$ 20 ms, $\approx$ 100 ms). Afferent innervation on the contrary originates from mechanical sensors located in the two atrias and ventricles. They monitor active muscular wall stress and passive wall strain. These nerval pulses are conducted within nerve pathways to regions placed in the medulla oblongata called nucleus tractus solitarii and dorsal vagus nucleus. Thence, frequency, duration of AV stim-

ulation propagation and contraction force are regulated to maintain regional physiological conditions endemic in the heart. A third possibility in adapting the hearts action lies in the interrelation between interventricular pressure and volume with ventricular wall tension. This intracardial mechanism acts independent from nerval and humoral influences. Although it plays a minor role in controlling cardiac output (CO = stroke volume per unit time), it´s contribution in compensating an elevated venous blood supply in end diastole and peripheral vascular resistance is major. A higher enddiastolic filling (pre-load: passively developed enddiastolic wall tension due to ventricular filling) causes wider straining of ventricular muscle fibres (increased volume) in diastole, effecting an increased shortening in systole. This 'Frank-Straub-Starling'-mechanism which elevates SV only depends on muscular characteristics. If total peripheral resistance (TPR) exceeds the physiological value, aortic pressure and pressure in the pulmonary artery (after-load: actively developed wall tension in ventricular systole to exceed diastolic aortic and pulmonary artery pressure) rises synchronously. Thereafter, the heart is not able to overcome arterial pressure. As a result, residual blood volume boosts the physiological value because of the reduced SV. Within the next pumping action, this extra blood volume adds to the constant venous backflow, resulting in a higher diastolic volume. Higher strained myocardium fibers attain a state with higher contraction (law of Laplace) and eject the normal physiological SV with elevated pressure. Acommodation onto lengthy burdens is achieved by structural thickening and lengthening of muscular tissue (hypertrophy), consequently leading into dilation of atria and ventricles accompanied by a gain in SV.

3.1.3. Conduction Elements: Arteries

The aorta takes blood form the LV and leads it to the big branches of systemic circulation. Approximately 25 percent of this portion are directed to the head and upper extremities, 50 percent to the trunk and abdominal viscera and 25 percent are directed to pelvic organs and lower extremeties. After an initial dextral directioned ascendency it proceeds arched into sinistral-posterior direction and afterwards draws downwards (figure 3.6). The first branch located at the aortic arch (brachiocephalic trunk) bifurcates into the right common carotid artery (RCCA) which supplies right head and neck and the right subclavian artery (RSA) supplying the right arm. Between the brachiocephalic trunk (BCT) and the left subclavian artery (supplying the left arm) lies the left common carotid artery for the supply of left head and neck. From it´s origin to termination it remains a tapering structure with a final cross section of about one sixth of that at the origin. The angle of taper measured in a canine aorta ranges from 0.4° to 1.0° [22]. Arteries are composed of a three-layered structure (see figure 3.7), where the innermost layer (intima) consists of an endothelial monolayer, surrounded by fine collagene fibers and a fenestrated elastic membrane. The outermost layer (adventitia) connects the artery (e.g.: aorta) with it´s surroundings and contains longitudinal elastic and collagenous fibers and embedded smooth muscle cells. Inbetween lies a tight layer of circular and helical oriented muscle fibres with embedded connective tissue (media). Big arteries like the aorta are characterized by a relatively thick intima and a tight elastic network in the media to obtain more distensibilty.

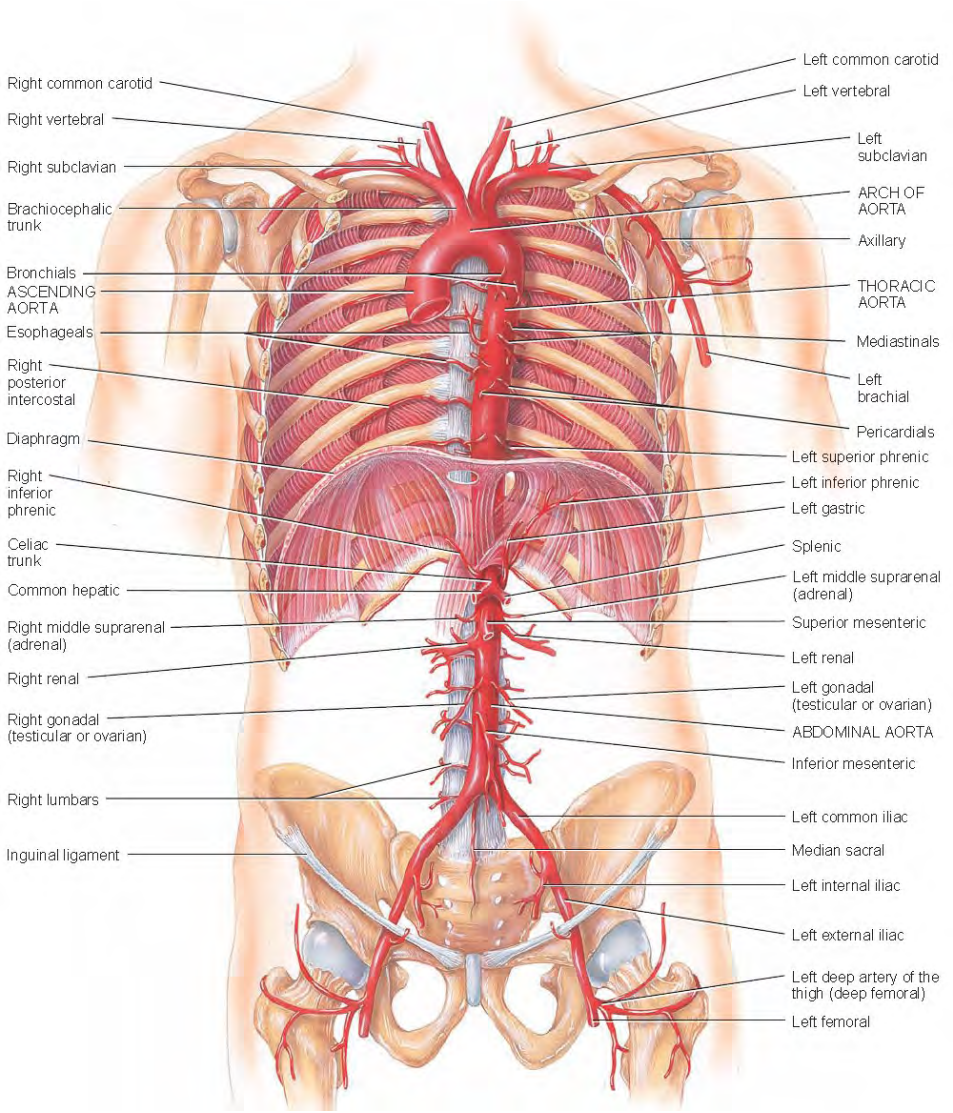

Figure 3.6.: Anatomic structure of the aorta (anterior view) [50].

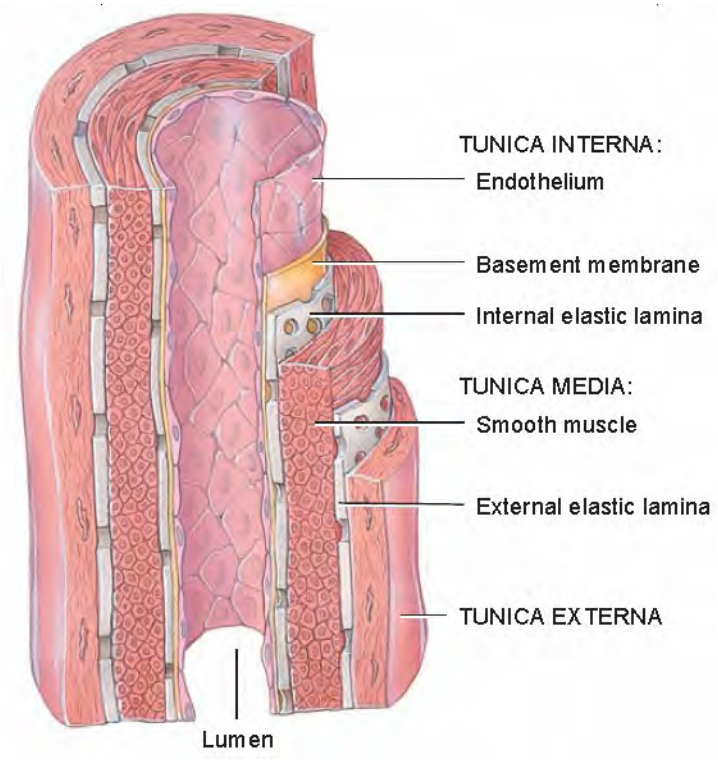

Figure 3.7.: Structure of a typical artery [50].

3.1.4. Arterial Blood Flow

Although all arteries show non-zero deformation (strain) when loaded with transmural pressure, a useful qualitative and quantitative approximation of arterial blood flow can be achieved by studying the principles of flow in rigid pipe systems and bends. Pressure forces are the leading driving forces of arterial blood flow, overcoming flow resistances. A first approximation is therefore pressure driven stationary laminar flow of a homogenous newtonian fluid in a rigid horicontal cylindrical pipe with uniform crossectional area and moistenable walls. Governing equations stating this special flow problem are the linearized steady Navier Stokes equations formulated in a cylindrical coordinate frame (pressure gradient only in z-direction, assuming laminar flow with velocity components only in z-direction). Mass conservation:

$$\frac{\partial w}{\partial z} = 0 \tag{3.5}$$

and momentum conservation:

$$\frac{\partial p}{\partial z} = \eta \frac{1}{r} \frac{\partial}{\partial r} \left(r \frac{\partial w}{\partial r} \right) \tag{3.6}$$

can be solved analytically [21,22,39,40,47], offering a relation between velocity and pressure:

$$v_{(r)} = \frac{(P_1 - P_2)(R^2 - r^2)}{4(x_1 - x_2)\eta} \tag{3.7}$$

where v stands for velocity, P_1 and x_1 are pressure and spatial coordinate at an upstream location of the tube, P_2 and x_2 the values more downstream, respectively. R and r denote the vessel´s radius and the actual radial coordinate of interest as independent parameter. η stands for viscosity. Last equation pictures a parabolic velocity profile. Time averaged velocity $\bar{v}$ is obtained by time- integration over the duration of one heart beat, maximum velocity turns out to be twice as big as $\bar{v}$ and located in the axial centerline stream (v_{axial}):

$$\bar{v} = \frac{R^2(P_1 - P_2)}{8\eta(x_1 - x_2)} \tag{3.8}$$

$$v_{axial} = \frac{R^2(P_1 - P_2)}{4\eta(x_1 - x_2)} \tag{3.9}$$

Necessary assumptions for the applicability of Poiseuilles law are laminar developed flow, a homogenous fluid, rigid tube and moistenable walls. Moistenable walls (no slip condition of vascular walls) are always met in natural flow phenomenons. Under physiological conditions, laminar flow can be found in nearly all locations in systemic cardiac circulation, with exceptions in aortic portions close to the heart, where flow is nonlaminar (transitional or turbulent) in small time instances of acceleration and decceleration of flow (ejection period) [22]. Sometimes 'laminar' is a missleading term, since true parabolic laminar flow as described within equation 3.7 is only met in some experiments with long and straight circular tubes carried out carefully. Therefore it is better to use the term laminar in a more general way for all velocity fields, where the streamlines don´t cross each other and the flow field keeps predictable. Such a nonparabolic situation of laminar flow is met in a situation, where fluid enters a horicontal cylindrical tube from a reservoir. Shortly after the entrance, the velocity profile is essentially flat, all laminae of the fluid move with the same velocity in axial direction. The step-by-step- developement of the profile from the entrance region to the fully developed parabolic profile is linked to the no slip condition of the wall and the viscosity of the fluid. Because of the flat profile at the entrance and the condition of zero velocity at the wall, velocity gradients are especially high in the near wall region. Due to viscosity between adjacent fluid layers, this velocity gradients produce shear stresses (pointing in reverse flow direction) which gradually deccelerate all laminae towards the midline of the tube. After a certain distance called 'entrance length', the transport of shear stress (friction) from the wall towards the centerline and pressure forces balance each other (equilibrium of forces), to finally obtain a stationary parabolic flow profile. Inside the entrance length, the 'boundary layer' - the outer portion of fluid in which a radially directed gradient of velocity exists - increases continously with downstream motion to finally fill the entire crossection of the tube in fully developed flow. Outside the boundary layer (in the middle of the tube), viscous effects are negligible, whereas viscous effects prevail inside and especially in the region near the tube wall. Laminar entrance length l_e^l and laminar Boundary layer thickness (δ^l) can be calculated by following formulas:

$$l_e^l = D0.06Re \tag{3.10}$$

$$\delta^l \propto \sqrt{\frac{\eta x}{\rho v}} \tag{3.11}$$

with Diameter (D), density (ρ), fluid velocity (v) and distance from entrance (x). The Reynolds number must be calculated with averaged entrance velocity (over entire crossection of the tube). A deviation to the parabolic laminar flow profile also results from the nonhomogenous character of blood, beeing a suspension of plasma and cells (non- Newtonian fluid). In smaller arteries, red blood cells are pushed towards the central axis of the vessel where they move faster as the wall bounded plasma [45].

Truly nonlaminar flow is characterized by radially and axially flow components (3D - flow), forming irregular (chaotic) eddies and vortices. Stationary flow in a smooth horizontal cylindrical pipe with constant diameter is said to be laminar inbetween $0 < Re < Re_t$ with $Re_t \approx 2100$ [40]. All streamlines (visualized with injected dye into the pipe) uniquely move into horizontal direction (1D- flow). Beyond Re_t ($Re_t < Re < Re_c$) the streamlines begin to fluctuate in time and space. This transitional region is characterized by moderate irregular behavior up to $Re_c \approx 4000$ [40]. If Re exceeds the critical value, streamlines almost immediately get blurred and randomly spread across the whole cross section of the pipe. The velocity components of the flow field consequently move into all directions (3D- flow). Re_t and Re_c still are dependent on vibrations of the pipe, roughness of the wall, obstacles at the entrance region and geometrical design of the pipe system. Fully developed turbulent flow after entering the tube from a reservoir can be examined after the turbulent entrance length:

$$l_e^t = D4.4Re^{\frac{1}{6}} \tag{3.12}$$

Turbulent and transitional flow are responsible for higher flow resistances burden the heart and arteries with extra loads (shear stress and transmural pressure) [45]. Shear stress between fluid layers in fully developed laminar flow is purely a microscopic effect comming from the random thermal motion of fluid molecules and attractive forces between the molecules. If a molecule from a slow moving layer near the wall darts into a faster layer, it consequently get´s accelerated at cost of the kinetic energy of molecules in the faster layer. This transport of momentum (energy) is responsible for viscosity in laminar flow. In turbulent flow, where random fluctuations and mean velocity are superimposed to determine instantanous velocity, shear stress is the sum of this laminar (microscopic) mechanism plus a macroscopic viscous term resulting from momentum transfer caused by large scale and small scale chaotic fluctuations, eddies and vortices.

Since the Reynolds number is the triggering factor of turbulence in stationary flow in a straight rigid cylindrical tube, an elevation of blood velocity in exercise conditions or within an aortic valve stenosis and a drop in viscosity caused by severe anemia (too less erythrocytes in the blood) can cause transition from laminar to turbulent blood flow [45].

Unsteady Flow

Pulsations impose inertial forces resulting from acceleration and deceleration of fluid to the steady determinants of flow (pressure and friction). Early models of pulsatile flow in straight tubes where based on Newtons second law of motion and Newtons definition of viscosity. The Womersley models [47] used linearized unsteady Navier Stokes equations and offered solutions for pulsatile flow in rigid and elastic tubes expanded by loading and constraint of

the wall, radial dilatation and viscoelastic effects [22]. Such models offered flow rates Q and velocity profiles with the assumption of sinusoidal pressure gradients, which drive the flow.

In unsteady flow, the finite amount of time required for development of turbulent energy (local flow disturbances in form of vortices, eddies, flow separation from the wall, backflow,...) at different length scales makes the Reynolds number futile for predicting laminar-turbulent transitions. Reynolds number calculated with instantaneous velocity predicts turbulent flow in theory while experiments [22] show laminar flow existing up to a Reynolds number of 2900 and disturbed (transitional) stable flow up to 7900. Since Reynolds numbers calculated this way are nothing more than collective properties of the entire cross section of the tube, it does not account for local and time- dependent velocity changes, gradients, geometry changes and obstacles. Therefore it is useful and necessary to define a 'pulsatile Reynolds number' regarding pulsations (e.g.: in arterial blood flow). This dimensionless number can be extracted out of the linear Womersley model of pulsatile pipe flow (rigid and uniform pipe). The pulsatile Reynolds number Re_{cp} is the product of an empirically determined factor k and the Womersley number α:

$$\alpha = \sqrt{\pi Re\ St} \tag{3.13}$$

where St is the dimensionless Strouhalnumber. Usually, k ranges from 250 - 1000 with lower deviations maybe resulting from outflow disturbances of fluid flow at the interconnection of a reservoir with a tube (e.g.: left ventricle and aorta). Critical values of Re_p in a dogs ascending aorta where transition from laminar to turbulent flow may be examined where found experimentally and turned out to be about Re_{cp}=150 α [22]. Another approach in accounting for pulsatile flow in determining the appearance of laminar- turbulent transition uses the fact, that local chaotic disturbances are damped out by viscous forces of the fluid. This damping is assumed to act only, if the instantaneous Reynolds number (calculated with the actual spatially averaged velocity) recides below it´s critical value Re_c (where a transition from laminar to turbulent flow happens in stationary flow). This ansatz works with a nondimensional relaxation time within a sinusoidal cycle defined as:

$$\tau = \frac{\epsilon v(Re - Re_{min})}{2R^2} \tag{3.14}$$

with ϵ as the time during a sinusoidal cycle when the Reynolds number is less than Re_c, Re_{min} as the minimum value of Re in one cycle. It is assumed, that if τ is small enough, disturbances are more likely to persist downstream [22].

Many arteries, essentially the aorta are naturally designed as curved pipes with several originating branches, where flow is geometrically forced to change direction. Consequently, the resulting centrifugal force applied on the laminae pushes them towards the outer wall of the bend. If the velocity distribution at the entrance is flat (as it is in pipeflow entering from a reservoir), all laminae tend to have approximately the same inertia. In this case, the centrifugal force produces higher pressures at the outer than at the inner wall of the bend. Bernoulli´s theorem now states, that kinetic energy ($\propto\ v^2$) must drop down at the outer wall. Thence the highest volicity is found at the inner wall of the bend. A parabolic distribution at the entrance disembogues into a tilled velocity profile towards the outer wall. This is the

case because the fastest moving axial stream in the middle of the tube will be the one most affected by the centrifugal force. Both situations develop secondary flow patterns, resulting from the movement of fluid towards the outer wall, repressing the fluid layers moving in outer regions of the bend. A unique consequence of curvilinear geometry lies in the production of convective (nonlinear) flow terms. In contrast to a straight pipe, where in developed laminar flow all laminae purely move in axial direction, the centrifugal force prompts laminae with higher velocity into regions with lower velocity. In the former case, nonlinear convective terms in the Navier Stokes equations cancel out, whereas in the latter case nonlinear terms like $u(\partial w/\partial r)$ or $w(\partial w/\partial x)$ ($u \ldots$ radial velocity, $w \ldots$ axial velocity) survive. Branchings in a bend (e.g.: brachiocephalic trunk in the aortic arch) create eddies due to bending of streamlines.

The assumption of a rigid tube combined with the incompressibility of blood account for the infinity of signal transporting speed. Pressure and velocity field changes upstream (e.g.: at the aortic valve) immediately have an effect downstream (e.g.: somewhere after the aortic arch). In other words, wave propagation velocity (phase velocity) is infinite, which has the same meaning as if to say, no waves propagate through the tube.

Effects of Arterial Elasticity

Blood vessels, especially arteries close to the heart (aorta, BCT, LCCA, LSA, RCCA, RSA) are distinguished with elastic properties, causing a widening of lumen when loaded with transmural pressure. The pressure- volume- law is not determined by Hookes law of elasticity (linear p - v - relationship), but shows an increase in wall stiffness with higher pressure load (nonlinear p - v - relationship).

Wave propagation (local disturbances of pressure or velocity propagate in space without mass transport) in the arterial system is a consequence of wall elasticity. If an SV of 70 ml is ejected into the aorta, aortic luminal volume and pressure increase. In a rigid tube, this extra volume and pressure pulse would propagate with infinite speed, while the velocity field of blood flow is determined by the Navier Stokes Equations. A distensible tube safes this extra portion of blood for a little while by extending it´s lumen and conducts this disturbances further downstream as a wave. Assuming linear elasticity of the vessel´s wall, the propagating waves likewise are linear, so that the velocity field derived from the linearised Navier Stokes Equations can be superimposed with solutions of the linear wave equation to obtain the actual velocity field of blood flow in space and time. 50 percent of systolic SV in the aorta are safed and carried further in diastole in this way, transforming the highly pulsatile blood ejection from LV into a more smooth and continous flow in more peripheral vessels near the organs. Pressure and velocity pulses are carried from one arterial segment to another with a wave velocity of about 4 - 6 m/s in young healthy men. Assuming a transport length of about 0.3 m pressure and velocity waves are delayed by a transit time of about 0.06 s (60 ms). Reflections cause a contrary effect in velocity amplitudes. The ratio of pulsatile flow to mean flow decreases from 6.3 in ascending cross sections to 5.6 in abdominal cross sections of the aorta. This decrease in pulsatility of blood transport comes from cancellation of pulses (destructive interference) by reflected waves and attenuating effects of viscosity [22]. Due to increasing stiffness of arterial walls, wave velocity elevates continously while advancing in age. What´s more,

stiffness is also increased in hypertrophy (higher blood pressure), because of the nonlinear pressure- volume (stress- strain)- relationship. Yet another phenomenon coming along with wave propagation is the reflexion of waves affected by monotonously increasing impedance in stiffer peripheral arteries. The reflected pulse wave superimposes with the primary pulse wave, so that the pressure amplitude in more peripheral vessels ($\approx$ 8700 Pa (65 mmHg)) exceeds the value of that in softer arteries farther upstream ($\approx$ 6700 Pa (50 mmHg)). What´s more, the pulse wave becomes steeper more downstream.

Shortly after beginning of systole (opening of aortic valve), volume flow rate in the ascending aorta amounts 500 - 600 ml/s (= 0.0005 m^3/s). Considering a cylindrical cross sectional area of 0.04 m^2 (corresponding to an aortic diameter of 0.0225 m), aortic blood flow velocity averaged over the entire cross section (like in inviscid flow) is 1.20 - 1.50 m/s. A short period of backflow of blood occures after a sharply fall away of velocity in the deccelerating phase of systole. The time averaged mean value of aortic flow velocity over one heart beat (CO = 5 l/min = 0.000085 m^3/s, aortic diameter = 0.0225 m) is 0.2 m/s. The contour of the flow wave is mainly determined by contractile properties of ventricular muscle and aortic input impedance [22]. About 1-2 cm after the aortic valve, the velocity profile is essentially flat, relatively slow at the wall and like a cylindrical slug in the mid stream. During it´s movement across the aortic arch, it get´s skewed as it would do in the preliminary discussed bend. Blood moves slower at the outer wall than at the inner wall. Helical secondary flow patterns consequently effect the axial flow to decrease (velocity vector summation). Secondary flow patterns are described by the additional dimensionless Dean number.

After the aortic arch, flow develops symmetrically until in the thoracic portion blood flows nearly parabolic (fully developed laminar flow). Signs of turbulence and transition appear in experiments of dog, horse and man for a short time during deceleration in the ascending aorta. On the contrast, other measurements obtained perfectly smooth velocity records at Reynolds numbers of 4300 up to 7800. Peak Reynolds numbers of about 9500 in man and 5000 in dog are reported [22]. Heart rate plays an important role in developing turbulence, since α increases proportional with rising frequency. Most of experimental data in canine, rabbit, dog, horse, cow, rat, pig suggest transitional conditions in the ascending aorta ($Re/\alpha \approx 250 - 1000$). Entrance effects from the left ventricular inflow vanish in the thoracic aorta, where the entrance length is about 20 times the aortic diameter [22]. Note that such experiments often are carried out with anestisized animals at rest. Conditions highly change in exercise, where heart rate and Strokevolume is elevated. Peak aortic flow is about 6 times higher than mean aortic flow, while acceleration at early systole is about 8 m/s^2 in dog at rest [22], a value which coincides with physiological values in men at rest [41]. Systolic blood pressure, diastolic BP and mean arterial pressure ($\approx$ 13300 Pa (100 mmHg)) in the ascending aorta are influenced by age, sex, pathologies, mentally, stress, outer stimuli (pain, coldness, heat, noises), nutrition, exercise (high elevation of systolic blood pressure and stabilized diastolic blood pressure leads to better circulation of working musculature). In accordance to the small change in diameter between the origin and the termination of the aorta, the pressure drop of 1 mmHg is rather small.

3.1.5. Regulation of Regional and Global Blood Pressure and Velocity

Besides the regulation of regional blood supply for organs to satisfy their needs in different situations of exercise, global control devices play a major role in regulating and adapting all different cardiovascular functions to brave all alternating circulatory crudities and situations.

The global regulation of circulation is based on modulation of CO, ensurance of a sufficing perfusion pressure for all organs, stabilization of blood volume by means of short, middle and longterm mechanisms. Short mechanisms with a response time of several seconds react on changing circulation requirements. Chronic load with a duration of days nullifies their activity partially or fully. Within this class of sensoric mechanisms (input to cardiovascular center), baroreceptors monitor blood pressure in the arterial system. Inter alia located in the adventitia and media of the aortic arch, their mechanosensitive sodiumchannels open due to straining the vessels wall. These pulses are conducted over a branch of the vagus nerve to the neurons responsible for regulation of circulation located in the brain stemm (Cardiovascular center, figure 3.8). Arterial lowering of pressure is answered by activation of sympathic

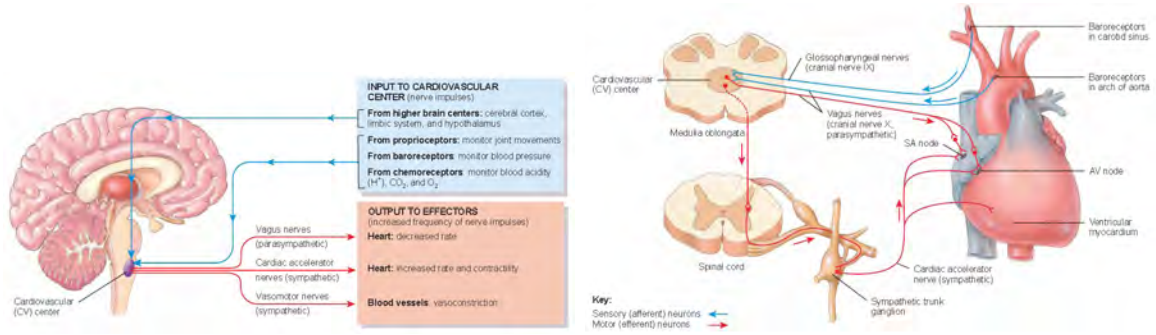

Figure 3.8.: Left picture: Location and function of the cardiovascular center. Right picture: Location of baroreceptors and the system of afferent (sensory) and efferent (motor) neurons [50].

nerves and a repression of parasympathic nerves (output to effectors). In the course of this regulation, heart frequency is elevated, contractility of the myocardium increased and TPR (total peripheral resistance) elevated by vasoconstriction of peripheral vessels. Arterial boosts of pressure lead to contrary reactions. Besides baroreceptors, strain sensors located in atria and intrathoracic veins, chemosensoric reflexes in case of hypoxia, hyperkapnia or acidosis and non- specific ascendancies which impinge on sensors beyond the cardiovascular system (e.g.: pain, coldness, strain of the lungs, contractions of sceletal muscle,...) as well are able to change circulatory parameters within few seconds. Mid- term regulatory systems account for the response of a sudden boost of blood pressure within minutes. Participants in blood pressure regulation are the Renin- Angiotensin- mechanism and adapting intravasal volume by transcapillary shift of fluid. Long- term blood pressure regulation fits the actual blood volume of the human body onto a particular cardiovascular situation. This is mainly achieved by changing depuration of renal liquor.

3.2. Pathologies

3.2.1. Bicuspid Aortic Valves (BAV)

In bicuspid aortic valve patients, the physiological aortic valve with three normal functioning cusps (leaflets) is replaced by a malformed valve structure consisting (most generally) of only two normal or partially normal functioning cusps. BAV is the most common congenital cardiac malformation, occurring in 1 to 2 percent of the population [1] and a frequency of 54 percent in all patients aged >15 years with valvular aortic stenosis [5]. After development, BAV is associated with aortic dilation, aneurysms, and dissection [1]. BAV include differ-

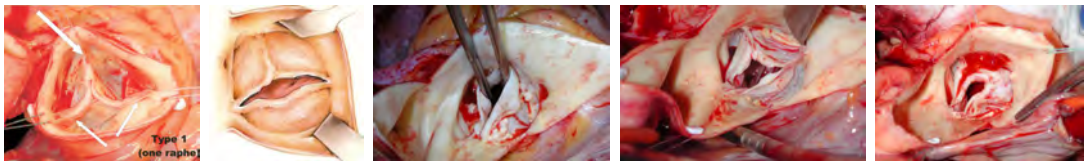

Figure 3.9.: From left to right: Type 1 BAV intraoperative, Type 1 BAV schematic, Type 0 BAV intraoperative, Type 1 BAV intraoperative in open position and Type 2 BAV intraoperative (a description of depicted BAV types is provided in section 3.2.1 [7,51].

ent morphologic phenotypes (figure 3.9 shows different variations of BAV) presenting with different hemodynamic conditions [7,52,53,54].

Definition

BAV is a congenital disease comprising a spectrum of deformed aortic valves presenting on gross examination with two functional cusps forming a valve mechanism with less than three zones of parallel appositions between cusps [7].

Classification

According to [7], BAV are classified by three characteristics: number of raphes (0,1,2), spatial position of cusps and raphes (related to the position relative to the left (L) and right (R) coronary sinuses) and functional status of the valve (predominant insufficiency (I), predominant stenosis (S), balanced insufficiency and stenosis (B) and no insufficiency and stenosis (No)). Three major types of BAV are identified (figure 3.10): type 0 (no raphe), type 1 (one raphe) and type 2 (two raphes). Within the study of 304 surgical specimen, type 1 was identified 269 times. The raphe most frequently was positioned between the left and right coronary sinuses in 216 (type 1, L/R) with a hemodynamic predominant stenosis (S) in 119 (type 1, L/R, S) cases [7]. Type 0 occured 20 times (13 times in lateral spatial position, 7 times in anterior-posterior position) [7].

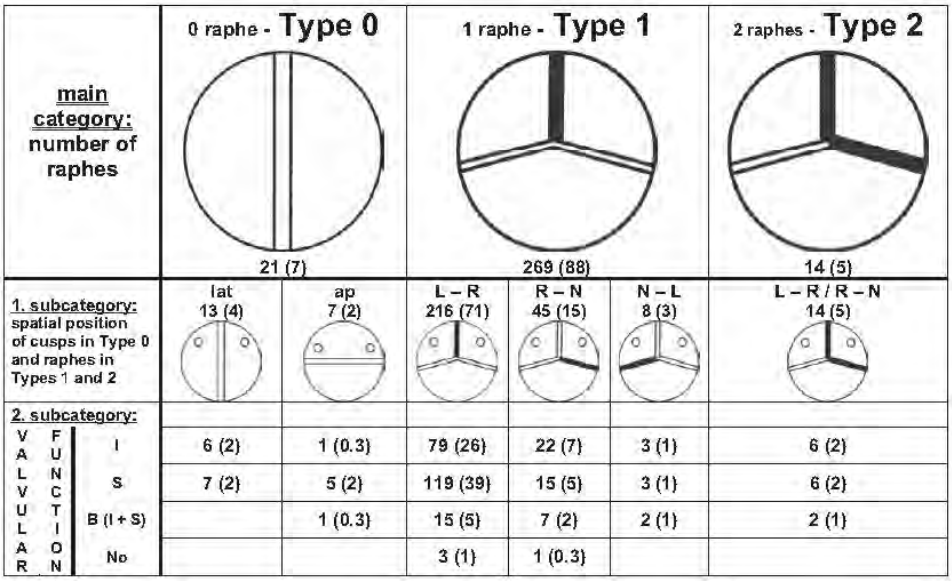

Figure 3.10.: Scheme of classifying bicuspid aortic valves [7].

Risks and Linkage to Aortic Dissection

[1,5] reports clinical consequences like valvular stenosis, regurgitation, infective endocarditis, and aortic complications such as dilation and dissection associated with BAV. In a cohort study examining cardiac outcomes in 642 consecutive ambulatory adults with BAV, AD occured in 11 patients during the follow-up period [3].

According to [2], approximately 50 percent of adults with severe aortic stenosis have a BAV, further more, severely stenosed BAV are very rigid, but are not narrowed. BAV occurs in 20-85 percent of cases of coarctation of the aorta, which is the cause of death by dissection of the aorta in between 19-23 percent in the presurgical era, but in 50 percent when there was a coexisting BAV [2].

The reason for the high incidence of AD in patients with BAV is unclear [2]. Among the uncertain attempted explanations, aortic root dilation states the most commonly identified vascular manifestation of aortic aneurysm and dissection formation [8]. It occurs more frequent in patients with BAV than in tricuspid aortic valves [2,8,15]. [7] additionally states, that dilatation of the ascending aorta is associated with a certain portion of BAVs, especially in young patients, exposing them to an increased risk of dissection formation. The discussion concerning causality of aortic wall changes like aortic dilatation related to AD in patients with BAV is controversely. Some authors [10,11,12] suppose, that aortic wall degenerations (aortic fragility) result from mutual defects in developement of both valve and aortic wall (genetically based), whereas others [9,13] represent the opinion, that the increased frequency of AD in patients with BAV is associated with disturbed hemodynamic properties in BAV, influencing structure and function of the aorta [6,15]. [14] suggests, that intrinsic pathology appears to be responsible for aortic enlargement beyond that predicted by hemodynamic factors.

Several studies show reduced aortic elasticity and reduced aortic root distensibility [4]. Among the hemodynamic normal stresses (pressure) and tangential stresses (wall shear stress WSS), WSS is known as a pathophysiological stimulus leading to gene expression and extracellular matrix remodeling [8]. From a fluid dynamical view, dilatation of the aorta in normally functioning BAV alters the spatial velocity gradients and thus the viscous forces at the artery wall [8].

3.2.2. Aortic Dissection (AD)

Definition and Morphologic Features

A dissection of the aorta is present when the aortic media has split and there is extraluminal blood in the aortic wall [16]. The splitting can vary from less than a millimeter in thickness to total occlusion of the true lumen [16]. Several initiating events are discussed in literature (see figure 3.11):

- A tear in the intima of the vessel leads to blood influx into the media, causing the media layer to tear appart [16,17].
- Perforation of the intima as, for example, caused by intramural hemorrhage and hematoma formation and mechanical traumatization of the intima due to the cannulation for catheter-based diagnostic and/or therapeutic interventions have been identified as initiating aortic dissections [17].
- Blunt traumatic aortic rupture following motor vehicle accidents [17].

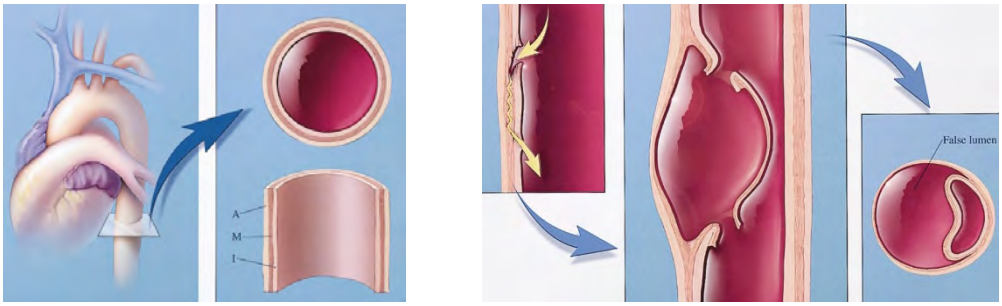

Figure 3.11.: Left: three-layered structure of the aorta. Right: schematic initial event of aortic dissection, beginning with an intimal tear and splitting of media [19].

The dissection can either propagate to the distal aorta or may also extend proximally, additionally, blood in the false lumen can reenter the true lumen or cause the outer wall (adventitia) to rupture [16,20]. Once blood enters the media via the intimal and medial tear, the time required thereafter to dissect the media of the entire length of the aorta appears to be only a few seconds [16].

Locations and Classification

In nearly 70 percent of the patients, the intimal tear is located in the ascending aorta, usaually about 2cm distal to the sino-tubular junction. The entrance tear is usually transverse and involves about one-half of the circumference of the aorta. The location of the dissecting false lumen is in the outer half of the media, therefore, the remaining outer portion of the aortic wall is much thinner, explaining its high frequency of rupture [16]. The entrance tear usually involves the right lateral aortic wall in the ascending aorta [16]. Next to the ascending aorta, the isthmus of the aorta, which is the site of attachment of the obliterated ductus (ligamentum arteriosum), is the most frequent site of entry tears. The relative fixation of the aorta at this site has been considered as the most likely explanation for the higher frequency of dissections there [16]. DeBakey used anatomic location of the dissection process to classify them [16]:

Type 1: The type I dissection involves the ascending aorta, as well as the distal portions of the aorta. Although in most patients the intimal tear arises as a transverse opening in the anterior wall of the proximal portion of the ascending aorta, it may also begin in the aortic arch or even in the descending thoracic aorta, with retrograde dissection to the aortic root and distal dissection throughout the remainder of the aorta.

Type 2: In type II, the dissecting process is limited to the ascending aorta and is usually characterized by a transverse tear in the intima anteriorly just above the aortic valve with the dissection terminating just proximal to the origin of the innominate artery.

Type 3: In type III, the dissection usually begins just distal to the origin of the left subclavian artery and extends distally for a varying distance.

Another important parameter for classification of dissections is the duration of the dissection at the time of its first presentation. Dissections are categorized as acute if its presentation occurs within 2 weeks of its onset and as chronic if more than 2 weeks have elapsed [16].

Incidence

In the United States, an incidence of about 2000 diagnosed cases per year are estimated [16]. The incidence of spontaneous aortic dissection is 530 cases per million people per year, and it strongly depends on the presence of risk factors [17].

Predisposing Factors and Risk Factors

Hypertension is the most important predisposing factor for aortic dissection [16,17]. It exists in 70 - 90 percent of these patients [16]. Hypertension can enhance atherosclerotic plaques and thus enhance cardiovascular disease and/or it can weaken the media and promote dissection [16], since atherosclerosis is a well established predisposing factor of dissection [17]. Experimental results show, that it takes an 8-fold physiological pressure to reach the ultimate tensile strength (rupture strength) of the aorta [16, 17]. Pressure in hypertensive patients is about 27000 Pa (200 mmHg) and exceeds the physiological pressure at least twofold. This relation shows clearly, that other factors contribute to dissection formation, which still remain unacknowledged. A step towards understanding the mechanisms causing

dissection formation can therefore only be made by respecting different kinds of mechanisms and scenarios. Other factors predisposing to aortic dissection are congenital disorders of the connective tissue, especially Marfan syndrome [16,17] and, to a lesser extent, Ehlers- Danlos syndrome [16,17] and aortic dilatation [17]. Also, congenitally bicuspid and unicommissural aortic valves [16] and aortic coarctation [16,17] are associated with an increased risk of aortic dissection. Interestingly, [18] report in their study of acute Stanford type A dissections (include DeBakey type 1 and 2 dissections), that genes coding for components responsible for the integrity and strength of the aortic wall (extracellular matrix components such as collagen IV a2 and a5, collagen VI a3, collagen XIV a1, collagen XVIII a1 and elastin) were down-regulated whereas components of inflammatory response were up-regulated. They suggest, that altered patterns of gene expression indicate a pre-existing structural failure, which is probably a consequence of insufficient remodeling of the aortic wall resulting in further aortic dissection. Dissection predominates in males, with a male:female ratio of 3:1, but there is an association with pregnancy. Half of all dissections in women under the age of 40 occur during pregnancy, usually in the third trimester [16].

Pathogenesis

A summary of the pathogenesis (how it may be) is given in the following list of statements [16]:

1. Medial degeneration in the wall of the thoracic aorta sets the stage by decreasing the cohesiveness of the medial layers of the aortic wall.

2. Repeated motion of the aorta related to the beating of the heart results in flexion stresses, most marked in the ascending aorta and proximal portion of the descending thoracic aorta, 60100 times a minute, 37 million times a year.

3. Hydrodynamic forces in the bloodstream, related to the pulse wave propagated by each myocardial contraction, as well as the level of systolic blood pressure, act upon the wall of the aortamost markedly the proximal ascending aorta.

4. A combination of these factors eventually results in an intimal tear, which leads to a hematoma dissecting into the media of the aortic wall. Hydrodynamic forces, primarily related to the steepness of the pulse wave dp/dtmax, as well as the blood pressure, continue to propagate the dissection until rupture occurs.

Studies in the aortic media between normal aging aortas, dilated aortas and dissected aortas carried out to find differences in features like cystic medial necrosis, elastin fragmentation, fibrosis and medionecrosis showed no qualitative but quantitative differences [16]. The authors suggest that the process of injury and repair represents part of the aging process in the aortic media and leads to wall weakening and comitant dilation [16], whereas hemodynamic forces could then influence these events further, leading to complete dissection [16]. Other studies suggest, that cystic medial necrosis associated with connective tissue disorders only plays a minor role in dissection formation and that the primary initiating event is the intimal tear with a following degeneration of the media and a loss of elastic tissue [19]. According to

this events, the mechanical strength of the aortic wall decreases. The mechanical approaches of [17] suggest, that these intimal defects can cause concentrations of mechanical stress of the pressurized aorta and may be the trigger for the propagation of the medial dissection and contribute to this these. Stress concentrations in tubes loaded with internal pressure with elliptical or circular holes can be calculated by the help of [16]. Mechanical forces contributing to aortic dissection include flexion forces of the vessel at fixed sites, the radial impact of the pressure pulse, and the shear stress of the blood [19]. A correlation between location of the dissection and hemodynamic forces can clearly seen from the fact, that classic Stanford type A and B aortic dissections produce an intimal tear at the areas of greatest hydraulic stress: the right lateral wall of the ascending aorta or the descending aorta in proximity to the ligamentum arteriosum [19]. Other authors suggest, that aortic root motion plays a role in dissection formation [16]. As a consequence of arterial hypertension, decreased vasa vasorum flow may increase the stiffness of the outer ischemic media of the aorta to produce interlaminar shear stresses contributing to the development of aortic dissection [19].

4. Methods: Computational Fluid Dynamics (CFD)

Physical phenomenas like viscous fluid flow include characteristics (mass, momentum, energy, turbulent kinetic energy, turbulence intensity, turbulence dissipation,...) which can be determined by partial differential equations (PDE´s). Computational Fluid Dynamics (CFD) provides tools for qualitative and quantitative flow prediction. Globally, it contains the physical and mathematical modeling process (Problem formulation), numerical methods to solve the mathematical equations (including software tools combining solvers, pre- and postprocessing). While an experiment (PIV, LDA, flow measurements, catheter- measurements,...) is a description of flow for one quantity at a time and a limited number of points, for limited scales and ranges of operating conditions, a simulation makes predictions of a flow situation for all desired quantities with high resolution (depends on the grid spacing and discretization technique), for every thinkable scale and any operating condition. Experimental errors can result from the measurement technique, unpredictable changes in operating conditions and changes of flow by sensors and probes. Errors in simulations come in by inadequate modeling, the discretization process (accuracy is always limited by the computational source), the iterative technique and the implementation. Also input data contains many sources of errors, since many factors in the modelling process depend on guessing and prediction. What´s more, the mathematical and geometrical model may be inadequate. Starting with some definitions and foundations of numerical mathematics, first part of this chapter gives an outline of the computational methods used to create the predictive aortic flow model. It should help to understand the workflow from stating the problem over postprocessing to the final verification and validation of the model and the numerical technique. Secluding, (Section...) outlines the strategy of an approximate structural analysis of the aortic wall synthesized by substituting the loads gained from the CFD study into simplified and remodeled governing equations of durability approval. The numerical stress and strain values concluded from the fluid-structure-interaction in comparison with experimental and clinical perceptions should finally give more insight in the mechanism underlying AD formation correlated (or not) with BAV disease.

4.1. Foundations of Numerical Mathematics for CFD

4.1.1. Partial Differential Equations (PDE)

A PDE is a mathematical equation, determining the behavior of a scalar or vectorial physical quantity (e.g.: fluid velocity, pressure, temperature) most general in time and space. Since

the physical quantity can be dependent of several independent variables and physical constants like viscosity, density, time and the three spatial coordinates in three dimensional space, a PDE may involve the unknown physical quantity, physical constants and partial derivatives of the unknown quantity with respect to the independent variables. Most general, a PDE for a certain quantity $v = v_{(x_1,x_2,\ldots,x_m)}$ dependent on m spatial and temporal variables is of the implicit form:

$$G(x_1, x_2, \cdots, x_m, v, \frac{\partial v}{\partial x_1}, \cdots, \frac{\partial v}{\partial x_m}, \frac{\partial^2 v}{\partial x_1 \partial x_1}, \frac{\partial^2 v}{\partial x_1 \partial x_2}, \cdots, \frac{\partial^2 v}{\partial x_m \partial x_n}, \cdots) = 0 \qquad (4.1)$$

with $n, m = 1, 2, \ldots N$, if N independent variables are determining the problem. G denotes a linear function in v. The quantity v can be either a scalar or a vector. Nonlinear PDE´s like the Navier Stokes Equations additionally involve quadratic or higher- order in the unknown quantity v (e.g.: v^2), making G a nonlinear function. Another possibility, describing the behavior of a physical quantity is the formulation of physical conservation laws in integral form (see section 2.4). These 'Integro- Differential Equations' (IDE) combine surface integrals and volume integrals over the dependent physical quantities and partial derivatives of the quantities. Each of the possibilities - PDE and IDE - needs different discretization methods to obtain a solution for the unknown variables.

4.1.2. Boundary Conditions and Initial Conditions

A boundary value problem (BVP) consists of a system of PDE´s, where special conditions at the borders of the geometrical and/or temporal domain must be fulfilled. These conditions are specified at the maximum and minimum values of the independent variables. Boundary conditions can either be specified as values (Dirichlet Boundary conditions) or the normal derivative of the value (Neumann Boundary conditions). On the contrary, an initial value problem (IVP) is a combination of PDE´s and conditions defined at the lower boundary of the geometric or temporal domain. Initial conditions are therefore defined as values or derivatives of the values at a constant value of the independent variable.

4.1.3. Discretization of PDE and Geometric Domain

For nonlinear PDE´s, where yet no analytical solution has been found, numerical methods are the only successive possibility to predict the physical characteristics determined by these equations. Numerical techniques used for gradients and derivatives in PDE´s transform the infinitely small (infinitesimal) change of a physical quantity v (dv) due to a infinitely change of a independent variable (time dt, spacial coordinate dx) into finite changes in v (Δv) and t or x (Δt, Δx). Continous volume integrals and surface integrals in IDE´s are transferred into discrete sums over finite pieces of faces or volumes. Among several discretization techniques, Finite Difference Methods (FDM), Finite Element Methods (FEM) and Finite Volume Methods (FVM) are frequently applied on physical flow problems. The latter is used in the commercial CFD software Ansys Fluent 12, where all simulations within this study where carried out. Both, FDM and FVM discretize the geometric domain (meshing)

and in further consequence discretize the mathematical equations on this splitted domain. For imagination, the continous geometric domain on which a PDE or a IDE is formulated can either be understood as a sum over infinite small sub- volumes or as a subdivided domain of spatial points with infinite space from one point to another. In FVM, the continous geometric domain is subdivided into interconnected control (sub-)volumes (C_V) of finite size, whereas in FDM, the geometric domain get´s subdivided into discrete points with finite grid spacing. Consequently, the governing equations are formulated separately for each C_V in FVM or each discrete point in FDM. Obviously, FVM is used to discretize IDE´s and FDM discretizes PDE´s. The ongoing discussion will only be concerned with discretization of IDE´s by FVM.

Meshing

The division of the solution domain can be done by structured grids, block-structured grids or unstructured grids. Among FVM, all grid types can be applied. Structured grid line families cross each other only once. Therefore, any position of a grid point is uniquely defined by a set of indices i, j, k in 3D- space. Block-structured grids are characterized structured families, that are subdivided to make the discretization of the solution domain finer. Unstructured grids are especially recommended for complex geometries. They are best adapted to the FVM and FEM approaches. Usually, these grids can consist of tetraheder, hexaeder or polyeder. Advantages are the possibility of local mesh refinement, flexibility and the possibility of automatic generation. Disadvantages are the irregularity of the data structure, which leads to the fact, that the matrix of the algebraic equation system get´s a irregular and non- diagonal shape.

Approximation of Integrals in IDE

For sufficiently small C_V´s, the exact IDE can be replaced by it´s discrete counterpart without losing too much of physical information. Picture 4.1 shows a schematic control volume with the notation used throughout the text. If the velocity field and the fluid properties are known,

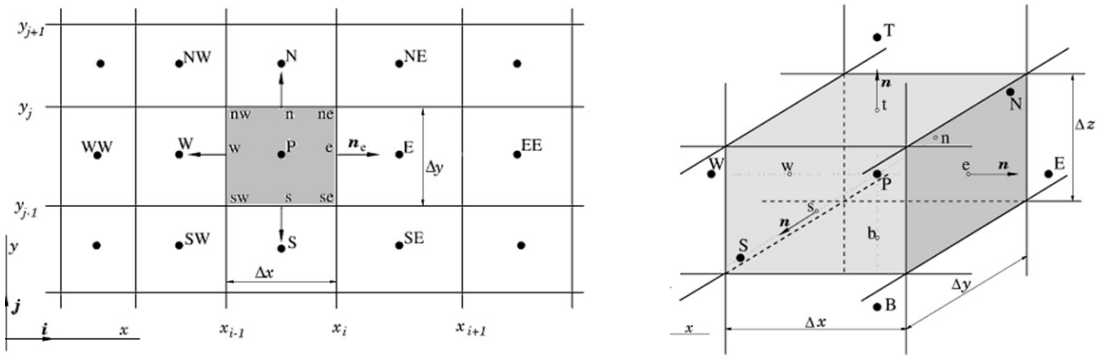

Figure 4.1.: Left: 2D control volume for a cartesian grid. Right: 3D control volume [36].

the net flux through the C_V boundary is the sum of integrals over the four (in 2D) or six (in

3D) C_V faces:

$$\int_{C_S} f dS = \sum_k \int_{C_{Sk}} f dS \tag{4.2}$$

where f is the component of the convective or diffusive flux vector at the surface of the C_V in the direction normal to C_V face [36]. The principles of conservation of mass and momentum are only fulfilled, if the C_V´s don´t overlap. The approximation of the surface integral for each location $k = e$ (east), w (west) etc. at each surface can be obtained by building the product of the integrand at the cell-face center with the cell-face area (midpoint rule):

$$F_e = \int_{S_e} f dS \approx f_e S_e \tag{4.3}$$

which is of second- order accuracy. Alternatively, the trapezoidal rule (second order accuracy), the Simpson´s rule (third order accuracy) can be used. Since only the value of f at the C_V´s center is known, an interpolation must be done to achieve the function value at the surface of the C_V. This can be achieved most simply by approximating ϕ_e by its value at the node upstream of 'e' (upwind interpolation, see [36] for details). Since this possibility brings numerical diffusion into the discretization process, other higher order techniques should be preffered. Higher order schemes like the linear interpolation (CDS), the quadratic upwind interpolation (QUICK), fourth-order CDS, skew upwind scheme and linear upwind scheme (LUDS) are described in [36,37]. Geometric examples approximating an arbitrary function are depicted in figure 4.2. To preserve the accuracies of the approximation, the interpolation

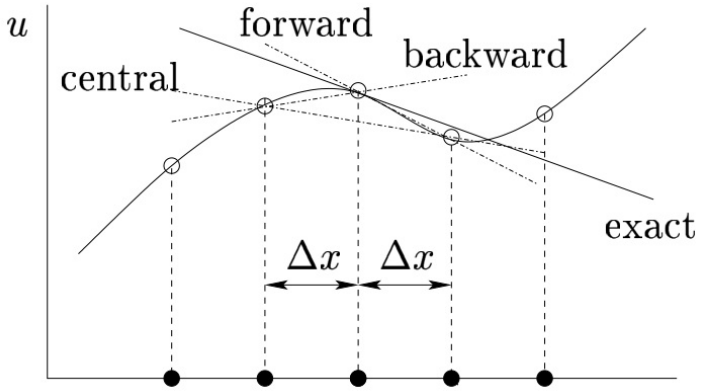

Figure 4.2.: Interpolation techniques to obtain the value of a function at the surface of a C_V [31].

technique must at least offer an accuracy equivalent to that of the approximation. The simplest way to approximate volume integrals in IDE´s is to replace them by the product of the mean value of the integrand and the C_V volume and approximate the former as the value at the C_V center:

$$Q_P = \int_{C_V} q dV \approx q_P \Delta V \tag{4.4}$$

where q_P stands for the value of q at the C_V center [36]. This second order accuracy scheme needs no further interpolation, since all variables are given at the C_V center P.

Approximation of Derivatives and Gradients in IDE

Unsteady problems involve time derivatives which also have to be discretized. Forces in future have no effect on the flow in the past, therefore unsteady problems are always formulated as IVP´s and solved step-by-step forward in time. In general, the Navier Stokes Equation, beeing a first order ordinary differential equation in time (initial value problem):

$$\frac{d\phi(t)}{dt} = f(t, \phi(t));\ \phi(t_0) = \phi^0 \tag{4.5}$$

can be discretized by integrating from t_n to t_{n+1}=$t_n + \Delta t$:

$$\int_{t_n}^{t_{n+1}} \frac{d\phi}{dt} dt = \phi(t_{n+1}) - \phi(t_n) = \int_{t_n}^{t_{n+1}} f(t, \phi(t)) dt \tag{4.6}$$

The implicit Euler method (FE method) uses the value of f at the upper integration boundary:

$$\phi(t_{n+1}) = \phi(t_n) + f(t_{n+1}, \phi(t_{n+1}))\Delta t \tag{4.7}$$

whereas the explicit Euler method (BE method) uses the lower boundary and the midpoint rule (LF) takes the value at the midpoint of the integration boundaries (see picture 4.3). All these techniques are of first- order- accuracy.

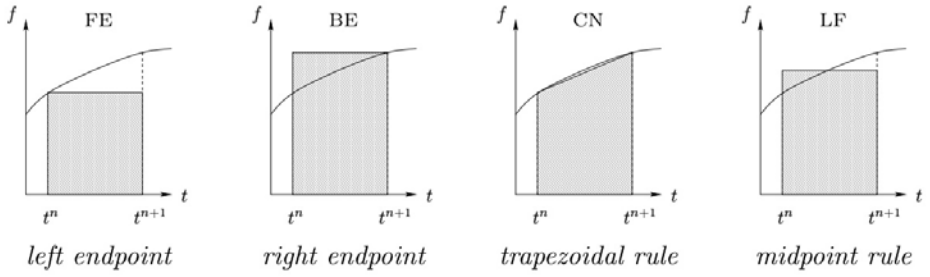

Figure 4.3.: Decisions concerning integration boundaries among time-stepping methods [31].

Spatial gradients and derivatives can be approximated by using the Green-Gauss theorem:

$$(\nabla\phi)_P = \frac{1}{V} \sum_k \bar{\phi}_k \vec{A}_k \tag{4.8}$$

where ϕ_k is the value of ϕ at the cell face centroid (P) and V is the volume of the cell. The summation runs over all the faces ($\vec{A}_k = \mathrm{A}_k \vec{n_k}$) enclosing the cell [48]. The evaluation can be done either cell-based ($\bar{\phi}_k$ is calculated as the arithmetic average of the two values lying in the neighboring cell centers) or node-based (taking the arithmetic average of nodal values at the cells face to obtain $\bar{\phi}_k$).

A summation over all approximated surface and volume integrals in the governing equations carried out for each CV of the geometric domain offers an algebraic equation system which substitutes the original, exact IDE.

4.1.4. Algebraic Equations

The discretization of a linear IDE results in a linear algebraic equation of the form:

$$A_P\phi_P + \sum_l A_l\phi_l = Q_P \tag{4.9}$$

with index P denoting the center of each CV and index l running over the neighbor faces (t, b, e, w, s, n, nn, ne, nw, ww, ee, sw, se and ss). Linear algebraic systems for the unknowns ϕ_l can always be written in matrix notation:

$$\hat{A}\hat{\phi} = \hat{Q} \tag{4.10}$$

The (square and sparse) coefficient matrix $\hat{A}$ contains information about fluid properties, geometrical features and in case of nonlinear equations, the variable values themselves [36]. $\hat{Q}$ consists only of known terms. In structured grids with grid locations described by regular index notation, one-dimensional arrays for storing the calculated values on computers are obtained by converting the indices into scalar storage locations [36]. Unstructured grids need different types of iterative solvers and storage strategies, since the coefficient matrix so far remains sparse, but loses it´s banded structure.

4.1.5. Iteration Methods

Among several solver possibilities for algebraic equation systems (direct methods: Gauss elimination, LU Decomposition, iterative methods: Jacobi method, Gauss-Seidel method, Gauss-Seidel SOR, Stone´s method, ADI method, Conjugate Gradient Methods, Biconjugate Gradients and CGSTAB, Multigrid methods, simultaneous solution, sequential solution, under relaxation, Newton-like techniques,...), iterative solvers are those who are neccessary for solving non-linear algebraic equations. Basically, an iteration method starts with guessing a solution of the algebraic equation and continous with systematically improving the solution by using the algebraic equation [36]. For a general system of linear equations, an iteration scheme (may) look like:

$$\hat{M}\hat{\phi}^{n+1} = \hat{N}\hat{\phi}^n + \hat{B} \tag{4.11}$$

where $\hat{M} - \hat{N} = \hat{A}$ and $\hat{B} = \hat{Q}$ if the converged iteration satisfies (Matrix equation) ($\hat{\phi}^{n+1} = \hat{\phi}^n = \hat{\phi}$). After n iterations, a non-zero residual $\hat{\rho}^n$ differentiates the approximate solution from the exact solution:

$$\hat{A}\hat{\phi}^n = \hat{Q} - \hat{\rho}^n \tag{4.12}$$

Subtracting this equation from the general algebraic Matrix equation yields the definition of the iteration error $\hat{\epsilon^n}$:

$$\hat{\epsilon^n} = \hat{\phi} - \hat{\phi}^n \tag{4.13}$$

The purpose of the iteration procedure is to drive the residual to zero; in the process, ϵ also becomes zero [36]. A basic example of an iterative solver is the successive over-relaxation (SOR)- solver:

$$\phi_P^{n+1} = \omega\frac{Q_P - A_S\phi_S^{n+1} - A_W\phi_W^{n+1} - A_N\phi_N^{n+1} - A_E\phi_E^{n+1}}{A_P} + (1-\omega)\phi_P^n \tag{4.14}$$

which is obtained by setting $\hat{M}$ as the lower triangular portion of the coefficient matrix $\hat{A}$. ω is called the over- relaxation factor, which must be greater than 1 for accelaration of the iteration process. For $\omega = 1$, SOR reduces to the Gauss-Seidel method [36], which is inter alia used in ANSYS Fluent [48]. During the iteration process, several properties inherent to the discretization and iteration method must be monitored and supervised carefully to keep errors introduced by the approximation process as low as possible.

4.1.6. Errors

Errors may occur in the physical and mathematical modeling process, the methods of numerical solving, in post processing and interpreting the results. An error is delimited from an uncertainty (potential deficiency due to lack of knowledge, e.g.: turbulence modeling) by the circumstance that it can be recognized. Acknowledged errors all can be identified, estimated and maybe eliminated within a certain limit by defined mechanisms. Unacknowledged errors which remain undiscovered may be questioning the meaningfulness of the whole model. Local errors are deficiencies at the cell level (e.g.: errors resulting from skewed cells), whereas global errors affect the entire flow domain. Since flow problems are highly dynamical, local errors may move through the whole computational domain, affecting the global solution of the problem.

Acknowledged and Unacknowledged Errors

- *Physical and mathematical modeling errors:* Modeling errors are responsible for the difference between the actual flow and the exact solution of the mathematical model [36]. Most frequently, they are introduced by mistakes, uncertainties, simplifications, estimations and assumptions in the physical modeling process. Within this process, manifold sources of errors may be introduced within the derivation of the governing equations, adapting the geometry, implementation and choice of boundary and initial conditions, usage of parameters and physical constants, turbulence modeling and many more.
- *Discretization errors:* Difference between the exact solution of the conservation equations used in the physical and mathematical model and the exact solution of the algebraic system. Spatial and temporal discretization of IDE´s or PDE´s by construction introduce errors (truncation errors) due to the finite (non-continuous) grid- (and time-step) spacing and the transformation of integrals and derivatives into finite sums and linear combinations of discrete values.
- *Iterative convergence error:* Difference between iterative and exact solutions of the algebraic equation. Even in a stable and consistent solution method, the remaining cut-off-error depending on the stopping criteria for residuals is not infinitely small.
- *Round-off errors:* Deficiencies coming from the finite accuracy of computer arithmetics
- *Software errors:* Computer programs seldom run free of mistakes. Software errors are introduced by imperfect coding and implementing.

- *Errors made by the user:* Using wrong parameters, physical constants, boundary conditions, initial conditions, models for describing turbulence,$\cdots$) during the modeling process

Unacknowledged errors like those introduced by the lack of physical and mathematical knowledge in turbulence modeling can only be evaluated by comparing solutions in which the discretization and convergence errors are negligible, (sic) with accurate experimental data or with data obtained by more accurate models (e.g. data from direct simulation of turbulence, etc.) [36].

4.1.7. Properties of Discretization and Iteration

Consistency

The discretization should become exact as the grid spacing tends to zero [36]. In a consistent approximation method, the truncation error in space and time becomes infinitely small when geometric mesh and time step spacing parallel are made infinitely small.

Stability

A solving process is said to be stable, if it doesn´t increase errors involved in the approximation process. An unstable iterative process would cause an increase in residuals ρ^n (diverging process).

Convergence

A consistent and stable solving process satisfies the condition of convergence. A convergent process offers solutions, which approximate the exact solution of the differential equation the better, the grid spacing tends to zero. As in non-linear differential equations like the governing equations of fluid flow no analytic 'exact' solution exists up to now [43], it is rather difficult to define properties of convergent solution methods within this kind of problems. Convergence (consistency plus stability) of a solution method for non-linear problems is therefore usually checked by carrying out a series of simulations where the discretization of the geometric domain (meshing) is successfully refined to finally obtain a grid-independent solution in case of a consistent and stable method [36].

Conservation

All governing equations of fluid flow (mass, momentum) are conservation laws by definition. Therefore, the numerical method must generate solutions, which do not injure these fundamental physical laws. Vividly, a certain quantity (e.g.: mass) entering a closed geometric domain (e.g.: a rigid tube), must - according to the law of conservation of mass - leave this closed domain without a change in amount.

Boundedness

Quantities which are described by physical principles strictly lie between certain boundaries. Mass density of physical matter for example is uniquely a positive quantity. Solutions of numerical techniques should lie between such boundaries. Some first order discretization schemes guarantee this property, while second order schemes (especially when applied on coarse grids) may produce unbounded solutions [36].

Realizability

Models of turbulence or multiphase flow should be constructed in a way, that offers physical realistic solutions.

Accuracy

The global accuracy of a numerical method is dependent on errors introduced by the development of the solution algorithm, in programming or setting up the BC´s, numerical solutions additionally introduce modeling, discretization and iteration errors. Accuracy should be maximized within the available resources and all remaining errors should be mentioned and estimated. In addition, the effect of each particular error on the final model must be defined and valued. This procedure offers an aid for deciding, if a model describes a particular physical problem accurately enough within certain boundaries. A precise awareness of all errors (acknowledged errors) within a model even can transform a completely inaccurate model into a useful model for future investigations, since it provides knowledge about mistakes and lacks made in the global process.

4.2. Methodology of CFD

To keep the description of methodology simple and lucid, most of the tasks carried out to obtain a predictive model of aortic flow in the tendered thesis are listed as a statement of numbers. This list should either be useful for later studies and simulations of incompressible fluid flow in arteries, inasmuch as it contains considerations and decisions made in the analysis process selected on the fundament of physical intuition, numerical solver theory and preliminary studies. All contained questions should be answered carefully and all multiple possibilities of decisions and considerations, every task should be made to obtain the most accurate, fastest and simplest way out of numerous numerical methods.

4.2.1. Problem Formulation

The Flow Problem, Special Physical Phenomenons

Blood - against its true natural composition - is assumed to be a homogeneous, Newtonian fluid with constant density ($\rho_b \cong 1050 \text{kg/m}^3$ [22,21]) and viscosity ($\eta_b \cong 0.0035$ Pa·s [22,21]). Deviations from Newtonian behavior have been found only in very narrow tubes, less than

0.5 mm in diameter [22]. The effect of possible variations of hematocrit on blood viscosity in certain deseases is neglected, since no evidence of a variation between TAV and BAV patients with AD could be found in literature. Viscous effects near the wall of blood vessels should be determined by blood plasma viscosity rather than viscosity of blood as a whole. Blood cells tend to be scarcer near the walls than in the rest of the stream [22]. This effect was reported in narrow tubes [22,21]. If this effect is also evident in larger vessels should be determined by literature research or experimental investigation, since with a cell free layer, the viscosity at the wall would be that of the plasma and would be smaller than that of the whole blood [21]. From a fluid dynamic point of view, this would probably have an effect on the flow patterns of blood flow. Mechanically, at a given shear rate, wall shear stress would be decreased threefold if calculated with plasma viscosity rather than with blood viscosity. Within the simulations, this uncertain effect is neglected. The pulsatility of heart action is responsible for a wide range of flow regimes in aortic blood flow. Over the whole heart circle and the spatial aortic domain, flow ranges from laminar over transitional (disturbed) to an onset of turbulence. This large bandwith of flow phenomena must be respected in the choice of a mathematical model. This is aggravated by the fact that a stenosed orifice area at the position, where blood enters the aorta (aortic valve), the instantaneous Reynolds number (and parallely the Womersley number) rises clearly above the critical value. Turbulence models used for predicting those irregular phenomena (if not simulated directly) must therefore be valid in laminar, transitional and fully turbulent regimes.

Geometry Definition and Computational Domain

The aortic arch geometry with its three branching arteries was originally taken out of [30], afterwards constructed in the commercial CAD software NX5 (Martin Stoiber). The aortic root (sinus of valsalva and aortic valve) was constructed within the commercial software ANSYS Design Modeler and finally linked to the arch by boolean operations. Dimensions of the aortic root could be gained out of [31,32,33] for the sinuses of valsalva and [31,33] for the aortic valve. The geometry of the inflow region from the left ventricle between velocity inlet and aortic valve was adapted from the systolic flow pattern found in [49]. All valve geometries depicted in figure 4.4 are drawn in fully opened position, which is truely a falsification of the physiologic case, since the valve cusps open and close during a heart cycle as a result of pressure differences between LV and aorta. An error estimation within the model is yet not possible.

Flow simulations involving dynamic valve cusp movement can be found in [31,33], unfortunately they did not compare their results with simulations carried out with rigid valve cusps. Among several initial trials with different inflow regions and aortic root geometries (simulations carried out with those geometries are for the purpose of the limit in pages not presented in the thesis, several initial simulations carried out with simple aortic geometry can be found in the project thesis), four final geometries were used to model the aortic patho-anatomy. A non-stenotic fully open BAV geometry with an orifice diameter of $d_{od} = 20$ mm serves as a reference model for three stenotic BAV models. Most frequently occuring BAV types where chosen as comparable models, namely Type 0 (pure BAV with no raphe) in lateral spatial position, Type 0 in anterior-posterior position and Type 1 L/R with a hemodynamic

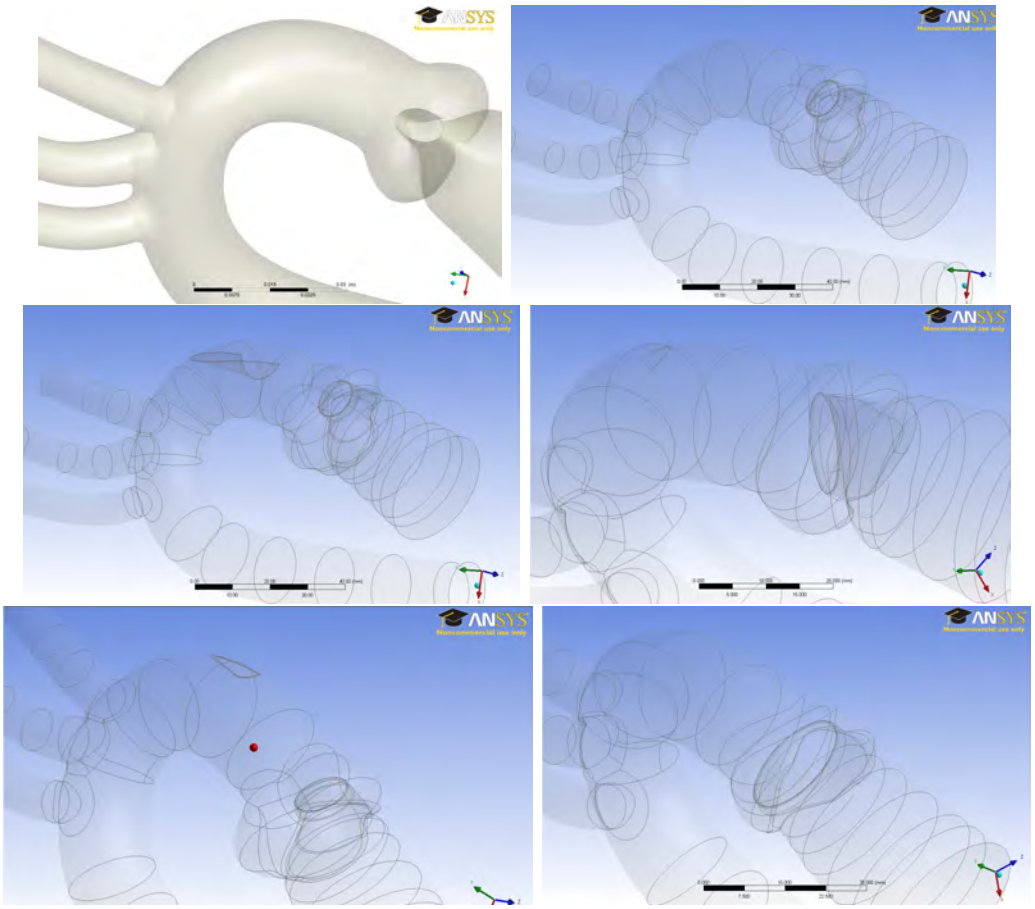

Figure 4.4.: Top left: Type 0 anterior-posterior; top right: Type 1 L/R-ND; middle left: Type 1 L/R-BD; middle right: Type 0 lateral-SD; bottom left: Type 1 L/R-MD; bottom right: non-stenotic fully open BAV

predominant stenosis (figure 4.4). The orifice areas where chosen to match the condition of severe aortic stenosis, where peak systolic blood velocity in the aorta exceeds 4 m/s [34]. Orifice areas in both Type 0 models are designed as elipses with diameters d_{maa} = 20 mm (diameter of major axis) and d_{mia} = 6 mm (diameter of minor axis), whereas in the Type 1 model the diameters are chosen as d_{maa}=12 mm and d_{mia}=10 mm. Conveniantly, Type 0 BAV models are constructed with two sinus concavities, whereas Type 1 received three concavities (as they are prominent in normal tricuspid aortic valves). After simulating those geometries, three different sizes (small, medium, large) of DeBakey Type I aortic dissections where constructed and linked to the outer curvature of the ascending aorta in all three stenotic BAV models. Conveniantly for all proceeding chapters, Type 0 lateral model with no/small/medium/large dissection will be denoted as Type 0 lateral-ND/SD/MD/LD and invariantly for the remaining types of BAV models. Geometrically, the dissections follow the descriptions from [35], experimental tests carried out at the *Center for Medical Physics and Biomedical Engineering, Medical University Vienna* and geometric intuition. The choice of location at the outer portion of the ascending aorta was made according to [65].

Flow Analysis Objectives

Finally, all four models should yield a reliable distribution of wall shear stress and pressure across the ascending aortic wall at rest and in strenuous exercise to be able to perform a comparative analytic stress analysis. These values can be compared with relevant clinical and experimental data. If the reference flow model (non stenotic orifice area) coincides only qualitatively, not quantitatively with physiological data, relative pressure and wall shear stress values obtained between the different models can serve to determine the differences between the physiological and the pathological state. It needs not to be mentioned, that quantitative and qualitative coincidence must be checked by comparing the simulated flow prediction with physiological evident data and experimental flow description. Therefore, the postprocess of the simulation must also yield an appropriate depiction of the predicted flow field.

4.2.2. Mathematical Model

Forces Influencing the Flow

Due to the pumping action of the heart, the pressure force accelerates the blood. On the contrary, blood is decelerated by forces due to friction (viscous forces between adjacent fluid layers). The imbalance between pressure forces and viscous forces is balanced by inertial forces that the blood possesses. Gravitational forces can be neglected, due to the fact, that hydrostatic forces are the same in all models and they are of negligible magnitude in comparison with pressure forces applied by the heart (in a horizontal tube with d = 0.1 m and a height of 0.05 m entirely filled with blood, pressure at the bottom is about 450 Pa (3.5 mmHg)).

Conservation Laws and Models

Besides the equations for mass and momentum conservation, which determine all physical phenomenons, turbulence models must be chosen if turbulence is not simulated directly [36]. Since the fluctuations caused by turbulence can be of small scale and high frequency, they are too computationally expensive to simulate directly. Instead, the instantaneous (exact) governing equations can be time-averaged (Reynolds averaging of flow quantities with the whole range of the scales of turbulence), ensemble-averaged, or otherwise manipulated (e.g.: filtering) to remove the small scales, resulting in a modified set of equations that are computationally less expensive to solve. The modified equations contain additional unknown variables, and turbulence models are needed to determine these variables in terms of known quantities to close the equations [37]. ANSYS Fluent 12 provides the following models: Spalart Allmaras, $k-\epsilon$-models, $k-\omega$-models and Reynolds Stress models belonging to Reynolds-averaged Navier Stokes (RANS) equations, furthermore Detached Eddy simulations and Large Eddy simulations. RANS equations often are used to compute time-dependent flows, whose unsteadiness may be externally imposed (e.g., time-dependent boundary conditions or sources) [37] and are therefore used in the pulsatile simulation of aortic blood flow. Within the RANS strategy, physical variables (e.g. velocity) in the Navier Stokes equations are separated into mean and fluctuating components. Consequently, the Navier Stokes equations are decomposed into terms including mean values and additional terms representing the effects of turbulence (Reynolds stresses), which must be modeled in order to close the momentum equations. Modeling in Spalart-Allmaras, $k-\epsilon$ and $k-\omega$ approach is usually accomplished using Boussinesq hypothesis, relating the Reynolds stresses to mean velocity gradients [37]. The Spalart-Allmaras model is effectively a low-Reynolds-number model, solving a modeled transport equation for the kinematic eddy (turbulent) viscosity [37]. The $k-\epsilon$-model is a semi-empirical model which assumes the flow being fully turbulent. It´s based on model transport equations for the turbulence kintetic energy (k) obtained from the exact equation and its dissipation rate (ϵ) obtained using physical reasoning [37]. The standard $k-\omega$-model is an empirical model based on model transport equations for the turbulence kinetic energy (k) and the specific dissipation rate (ω), which can also be thought of as the ratio of ϵ to k. In Fluent 12, it incorporates modifications for low-Reynoldsnumber effects, which makes it applicable to wall bounded flows and free shear flows [37]. The four equation shear-stress transport (SST)-$k-\omega$-model effectively blends the robust and accurate formulation of the $k-\omega$-model in the near-wall region with the free-stream independence of the $k-\epsilon$-model in the far field, which is achieved by multiplying each model by a blending function. Both models are added together. The blending function is designed to be one in the near-wall region, which activates the standard $k-\omega$-model and zero away from the surface, which activates the transformed $k-\epsilon$-model [37]. The Reynolds stress model (RSM) closes the Reynolds-averaged Navier Stokes equations by solving transport equations for the Reynolds stresses, together with an equation for the turbulence dissipation rate. Seven additional transport equations must be solved in 3D, making it computational expensive. Nevertheless, it accounts for the effects of streamline curvature, swirl, rotation, and rapid changes in strain rate in a more rigorous manner than one-equation and two-equation models, it has greater potential to give accurate predictions for complex flows (cyclone flows, highly swirling flows in

combustors, rotating flow passages and stress induced secondary flows in ducts) [37]. Among the numerous turbulence models, the Transition SST-$k-\omega$-model appears to be the best choice (see figure 4.5 for the particular possibilities in ANSYS Fluent model setup), since it is valid in a wide range of Reynoldsnumbers. What´s more, it offers a good compromise

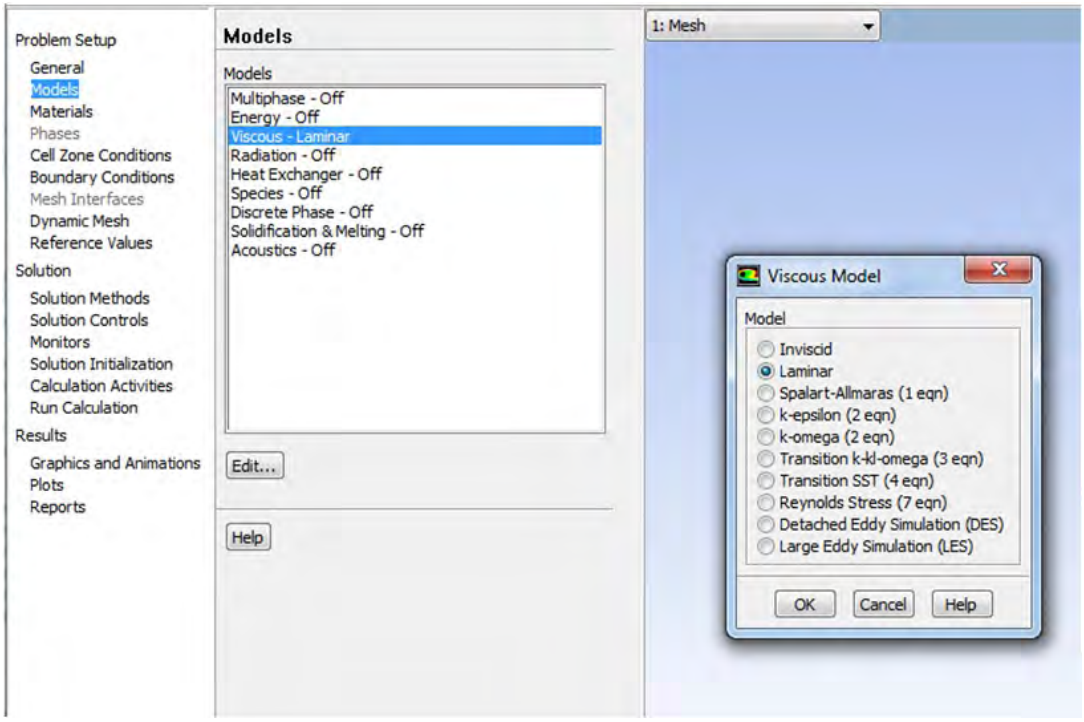

Figure 4.5.: Possibilities for choosing a turbulence model in ANSYS fluent model setup

between accuracy and computational effort, which could be confirmed within the simulations. In practical CFD, each turbulent model should be applied on a flow model with comparable boundary conditions. A comparison yielded possible errors between each model.

Constitutive Relations, Boundary and Initial Conditions

Due to neglecting the elastic behavior of the aortic wall in the simulation, the only constitutive relation involved in the flow problem is the description of blood assumed to be an incompressible Newtonian fluid. The special form of the viscous term in the Navier Stokes equations can be found alternatively in [21,29,40] and in section 2.2. Constitutive equations for Non-Newtonian behavior of blood (e.g.: Cassons equation) can be found in [21]. According to the geometric domain, 6 boundary conditions (BC) are required to define the physical values on all borders: Inlet BC at the left ventricle, outlets BC at the three branching arteries and the abdominal aorta and the wall BC. Pressure as the accelerating force is physiologically exerted onto the blood from the left ventricle (inlet). From a fluid dynamical standpoint, it is indifferent, whether the inlet is defined as pressure inlet and the outlets are defined as velocity outlets or vice verca, since only pressure gradients are responsible for accelerating the fluid. For reasons of easier implementation of boundary conditions found

in literature (depicted in figure 4.6), the inlet located at LV was specified as velocity inlet, the outlet (abdominal aorta) as (static) zero pressure outlet. All boundary conditions

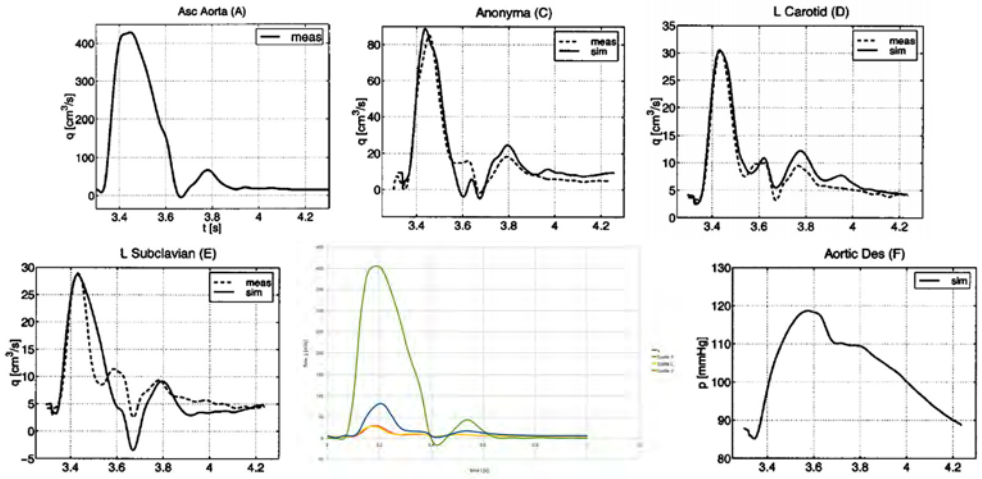

Figure 4.6.: Boundary conditions used in all aortic flow simulations at rest. Top left: inlet flow profile for left ventricle; top middle: outlet flow profile for brachiocephalic trunk; top right: outlet flow profile for left common carotid artery; bottom left: outlet profile for left subclavian artery; bottom middle: inlet and outlet profiles after digitization and transformation into velocities; bottom right: pressure outlet profile for descending aorta

except the constant static pressure outlet are defined as completely flat transient velocity profiles gained from [41] by digitizing the time-flow curves with a $x-y$-extractor free share software and transforming blood flow values into blood velocity values ($[v]$ m/s) by using diameters at the locations of inlets and outlets. Figure 4.7 shows the format of a particular editor file, which must be read into the Fluent profile setup (the number 7 in parenthesis stands for the number of time and velocity values in the file) and the surface of boundary setup boxes. As a consequence of zero pressure at the outlet, a measured pressure profile

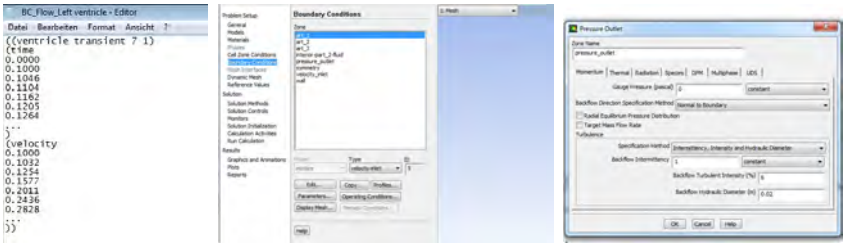

Figure 4.7.: Left: Format of the left ventricle inlet velocity file; middle: boundary setup in Fluent; right: particular settings in boundary box of pressure outlet boundary

[41] must be added to each simulated transient pressure distribution (bottom right graph in figure 4.6). Boundary conditions for simulating exercise conditions could not be found in

literature, therefore, the elevation of CO was modeled by using the proportions described in section 3.1 for the transient velocity profiles used as exercise boundary conditions). Fluent 12 does not offer velocity outlets, hence the blood flow outlets at the three branching arteries where defined as velocity inlets with negative velocity. According to the considerations made in appendix B, the wall must be characterized by a no-slip boundary condition. Among the turbulence specification method for each inlet or outlet, backflow intermittency is set ot 1, backflow turbulent intensity (BTI) was calculated at the LV inlet (5.4 $\%$), ($\approx 6\%$) at the abdominal aorta outlet and ($\approx$ 6.6$\%$) at the three branching arteries. Backflow hydraulic diameters (BHD) are specified as cross-sectional diameters of the vessel at the locations of inlets and outlets (hydraulic diameters of eliptic cross-sections must be defined alternatively): BHD_{LV} = 0.032 m, BHD_{BCT} = 0.009 m, BHD_{LCCA} = 0.008 m, BHD_{LSA} = 0.0085 m.

Simplifications and Assumptions

Simplifications about the flow regime cannot be carried out, since the flow characteristics must be assumed to range from laminar to fully turbulent.

Gravity can be neglected for reasons described above, introducing a maximum physical modeling error of about 2.9 percent at the relevant peak systolic pressure value (16000 Pa (120 mmHg)).

Several simplifications where made concerning the aortic geometry and the physiological behavior of the aortic wall. The aortic geometry [30,31,32,33], designed in ANSYS Fluent 12 Design Modeler, is free of buckets and billows which are usually present in anatomical aortic geometries. The aortic diameter is rather small, but lies in the range of normal dimensions. The brachiocephalic trunk is too small with respect to the subclavian artery and the common carotid artery. Errors can only be estimated by comparing the simulation with reverence simulations which are based on anatomically correct aortic arch models.

Each aortic model was designed to be symmetric regarding to the longitudinal axis. That makes it possible to slice the geometry. This procedure introduces a neglection of the anatomical flexion [51] of the aortic longitudinal axis. The largest differences in the flow field concern secondary flow patterns [51] and the pressure distribution caused by the jet, which most probably affects other regions at the circumference of the wall (a comparison with non-symmetric geometries can be found in chapter 5). Apart from that, the more or less comparative nature of the study makes those differences vitiate. What´s more, the differences in pressures and wall shear stresses between the symmetric and non-symmetric geometry are considered to be negligible small. This can be deduced from the fact, that the numerical (concerning the values of pressure and wall shear stress) differences between Type 1 L/R, Type 0 anterior-posterior and Type 0 lateral simulations are futile.

Another simplification was made in neglecting the elasticity of the aortic wall. All flow simulations where carried out with rigid wall behavior. With pulsatile flow, the elasticity of the vessel wall becomes a critical determinant of pressure-flow relationships [22]. Pressure- and velocity waves in a rigid wall model are neglected per definition, since changes of physical quantities at the inlet are transported within infinite velocity to the outlet. Wave reflections, existing in distensible tubes, which are responsible for elevation of pressure curves towards more peripheral regions of the aorta can not be observed within the rigid model. Errors can

be deduced by comparison with in vivo pressure and velocity measurements along the length of the aortic arch.

4.2.3. Solving the Mathematical Equations

The set of mathematical equations must be transformed into a discretized algebraic system of equations to finally be able to solve it with an iterative solver mechanism. Usually, the governing equations of physical problems contain independent spatially (three dimensional space) and temporal variables. Iterative techniques offer a tool for solving nonlinear algebraic equations obtained from the discretization process. To develop an accurate solution, convergence of the method should be carefully examined by monitoring residuals, relative solution changes and the fulfilling of conservation laws.

Meshing

Fluent 12 offers a semiautomatic mesh tool illustrated in 4.8. Among standard choices about

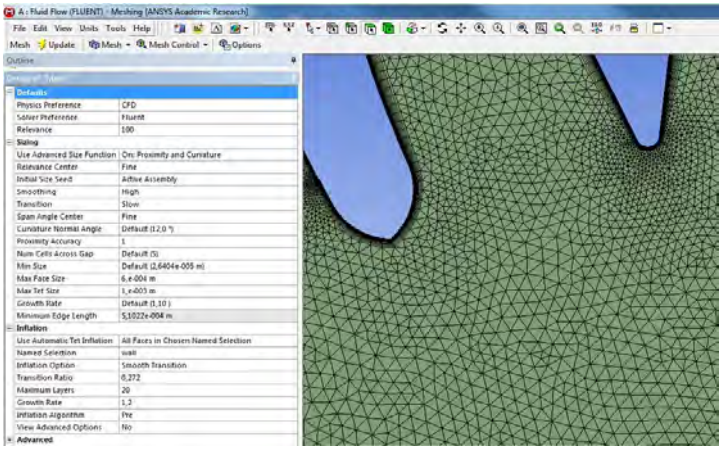

Figure 4.8.: Mesh setup in ANSYS Fluent workflow

grid type (hexahedra, tetrahedra, prisms/wedges) and appropriate mesh sizing, wall bounded prism layers should be considered to accurately resolve large velocity gradients or the shear stress near the wall (in laminar flow and even more in turbulent flow). As for the problem of appropriate mesh sizing, successful mesh refinement (carry out simulations reiterated simulations by starting with a coarse mesh and refine the mesh step by step to finally obtain an almost grid independent solution) leads to a mesh fullfilling the conditions of accuracy with least computational effort. Regions, where turbulence and flow separation at the wall can be expected should be meshed as fine as possible to accurately resolve these special physical phenomenons. Wall bounded prism layers especially ensure accurate physical outcomes in combination with the transition SST-$k-\omega$ model for turbulent flow modeling. According to [37], the first wall bounded prism cell centroid should lie between the wall and the dimensionless viscous sublayer thickness $y^+ = 1$ - 5. Because it is a value dependent on the specific flow situation, y^+ can be examined only after the solution process in postprocessing.

If y^+ exceeds the limit in some locations near the wall, additional local mesh refinement is required during the remeshing process. The free stream can either be meshed by hexahedra elements (simple geometries: straight smooth tubes, smooth bends) or by tetrahedra elements for more complex geometries. Within the Setup, the tetrahedra/prism (only available for tetrahedra/prism) meshed domain can be converted into polyhedra elements. This reduces the overall cell amount three- to five-fold without worsening the convergence behavior [37]. The geometric mesh should fulfill several quality criterias, which can be monitored after the meshing process (mesh setup):

- *Smoothness:* Describes, how fast cell voluminas change from a cell to a neighboring cell. Fast changes lead to bigger truncation errors [37], therefore, changes should be kept small by chosing high smoothing in the mesh setup.
- *Skewness* (only important for tetrahedra meshes): Denotes the difference between geometry of the actual cell and a equilateral reference cell of the same volume. A high skewness is responsible for a decrease in accuracy and stability of the numerical technique [37]. Good convergence of the numerical scheme are achieved by keeping cell skewness under 0.95 (in Fluent).
- *Cell squish* (relevant for polyhedra meshes): Corresponds to the definition of skewness in tetrahedra meshes. Good cells show squish values near zero.
- *Aspect ratio* $AR = A/B$: Is a measure for the tightness of the cell. Cells near a wall should not exceed an AR of 10/1, cells further from the wall should be designed with AR smaller than 5/1.

All above defined mesh requirements are complied for the aortic geometries by a tetrahedra mesh with 7 wall bounded prism layers consisting of a cell amount ranging from 1.1 to 1.4 million cells (depending on the geometry of the aortic root). A representative mesh setup generating the actual mesh used in the simulations is depicted in figure 4.9.

General Solver Setup

In incompressible flow problems, pressure based solvers (PBS) with absolute velocity formulation should be favored versus density based solvers (DBS), since PBS originally where developed for incompressible low velocity flows, whereas on the contrary DBS per construction are sufficient for compressible high velocity flows (gases) [37]. In PBS the velocity field is calculated by means of momentum equations. Additionally, pressure is derived within a pressure equation or a pressure-correction equation obtained by manipulation of continuity- and momentum equation. Fluent solves these IDE´s by FVM techniques. Pulsatile flow requires to set the 'Time'- option to 'Transient' (figure 4.10). Gravity can be neglected, units require no further setting apart from default values (SI units).

Pressure and Velocity Coupling

Pressure-velocity coupling (pressure correction) is needed, because a haphazard substitution of pressure into the discretized equations injures the equation of mass conservation. Fluent

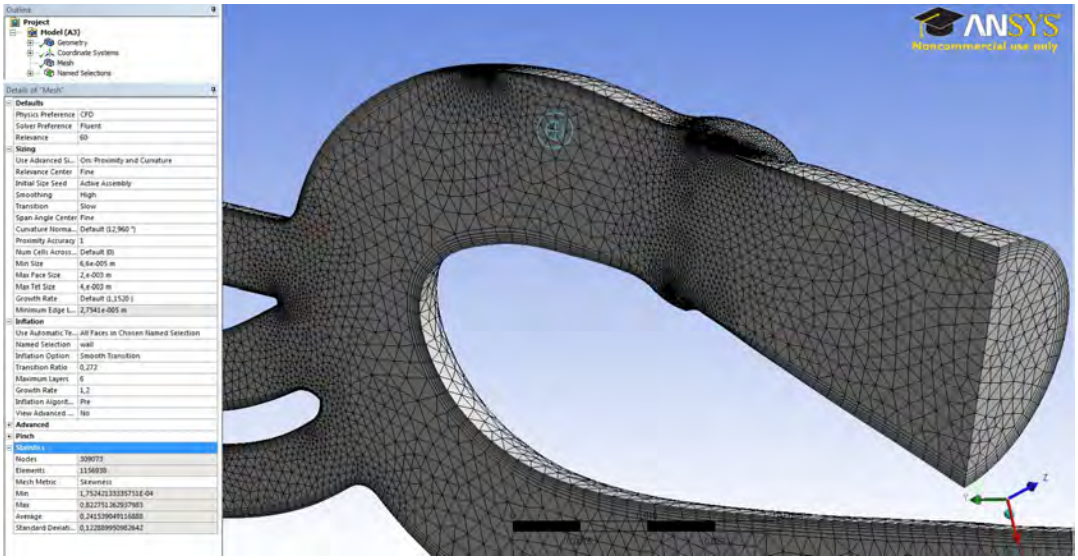

Figure 4.9.: Representative mesh setup and corresponding mesh

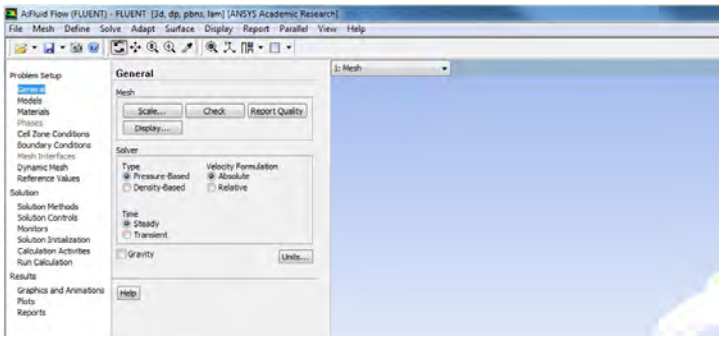

Figure 4.10.: General setup in ANSYS Fluent workflow

offers SIMPLE (sufficient for all type of flows, small time steps required), SIMPLEC (only for trivial flows without additional models) and PISO (advantageous for transient flows, time steps can be chosen bigger than in SIMPLE). SIMPLE was used instead of PISO, inasmuch as the latter showed poorer convergence history. SIMPLE turned out to be a stable coupling mechanism within sufficient small time steps. All possible choices can be seen in figure 4.11.

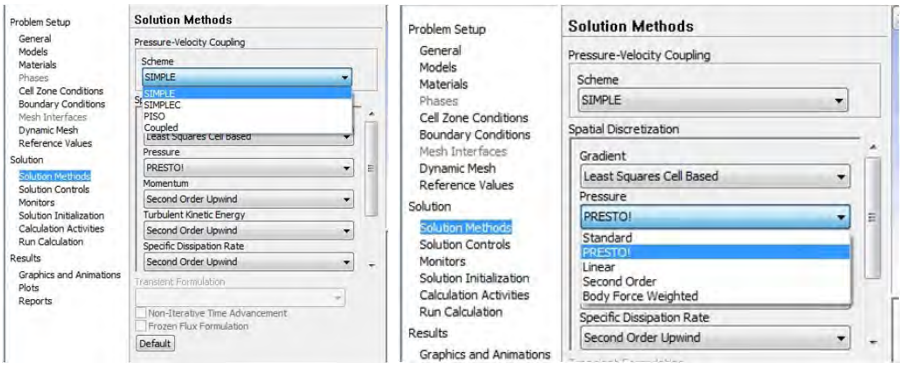

Figure 4.11.: Solution setup in ANSYS Fluent workflow

Discretization of Spatial Terms and Derivatives

All choices about spatial discretization (interpolation) of gradients, pressure, momentum, turbulent kinetic energy (TKE), specific dissipation rate,... are depicted in figure ??. Second order accuracy is required in all terms, since the second order accuracy of the numeric derivation of volume and surface integrals is only retained when the interpolation technique is at least of the same accuracy than that of the integral derivation. QUICK schemes are only valid in hexahedra meshed domains. Central difference schemes can only be used in LES turbulence models. The attended accuracy for turbulence models can therefore only be complied by using second order upwind schemes. Least squares cell based gradient derivation is preferred to Green Gauss Cell/Node based for reasons of higher accuracy when using polyhedra meshes. Alternatively, node based techniques should be used within tetrahedra meshed domains. PRESTO! (Pressure Staggering Option) is the best choice for pressure interpolation in strong curved geometries and highly swirling, rotating flows.

Temporal Discretization

The transient formulation was set to second order implicit for reasons of higher accuracy. As noted above, SIMPLE requires sufficient small time steps to converge fast enough. A successful trial-and-error method yielded a time step size of $\Delta t_{re} = 0.0005$ seconds (for the transient inlet LV inlet condition at resting conditions) and $\Delta t_{ex} = 0.0002$ seconds (at exercise conditions) together with a maximum number of iterations per time step ($n = 30$).

Convergence Monitors

Besides the supervision of residuals, convergence monitors should be used to examine the convergence history of every single iteration cycle. Consequently, surface monitors and volume monitors (as depicted in 4.12) where created to police relative solution changes from one iteration step to the next. A criterion for the magnitude of sufficiently small inferior

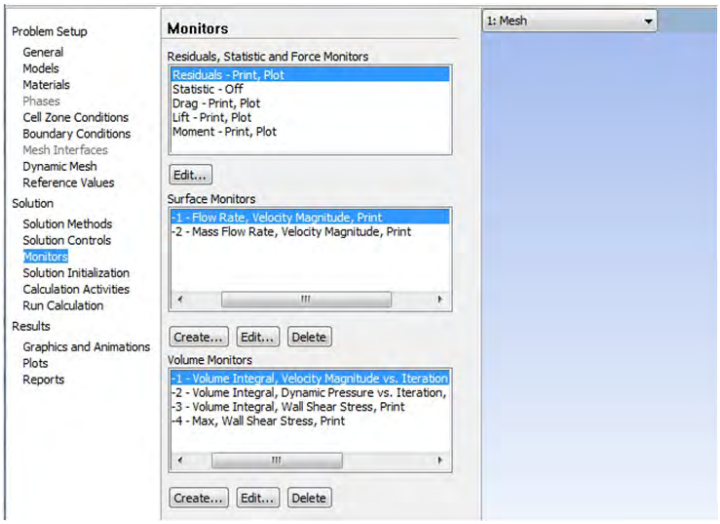

Figure 4.12.: Convergence monitors used in all aortic flow simulations

solution changes can only be determined by examining a set of simulation solutions, each cut off at different amounts of iteration steps. The quality of conservation of mass within a simulation can be used as a tool reviewing convergence. Among all simulations, the difference between mass flow ($[m]$=kg/s) at the inlet and mass flow at the four outlets could be reduced to 10^{-6} - 10^{-8} kg/s.

4.2.4. Postprocessing

Postprocessing serves as a tool for visualization of local and integral physical quantities of interest. Besides total pressure, static pressure and dynamic pressure, wall shear stress and the velocity field (two dimensional contour plots at the aortic wall and in cross sections perpendicular to the wall), turbulent kinetic energy, turbulent intensity, y^+ and intermittency can serve as quantities for further investigations, verification and validation. The velocity field can be depicted by means of contour plots and arrows. All particular choices of visualization, a partial effort of verification and validation of the model can be found in chapter 5.

5. Results and Discussion

The results of the CFD study are all gained from the postprocessing tool within the ANSYS Fluent workflow. To keep the paper as short as possible, only essential results with a possible dominant effect on Aortic Dissection are presented.

At the very beginning of this chapter, the velocity field of several aortic flow models (resting conditions) is depicted in various views. A comparison with flow experiments, reference simulations and clinical studies will partially indemnify for the missing experimental PIV validation. Subsequently, the pressure distribution will be validated in the same manner. A comparison of simulated hemodynamic values with the pathologic case should show the tight relation between predisposing factors and pathogenesis of AD with hydromechanical stress and strain. A succeeding comparison of stresses and strains according to the stress analysis described in section E.2 with in vivo and ex vivo experimental data should underline these correlations. A 'gedanken experiment' based on long life fatique strength testing and theory, commonly used for material testing in mechanical engineering should defy over the lack of appropriate experimental long life strength data of aortic tissue. Finally, a comparison of wall shear stress (WSS) distribution across the ascending aortic wall between physiologic and pathologic models manifold elevations is depicted.

5.1. The Velocity Field at Rest

Velocity is depicted by means of:

- The velocity field in the symmetry plane (section 5.1.1) of the ascending aorta and aortic arch (velocity arrows and velocity contour plot);
- Velocity contour plots and velocity arrows (section 5.1.2) in 6 different crossections perpendicular to the ascending aortic wall.
- Secondary flow patterns (tangential projection of velocity in the plane perpencicular to the vessels wall) at two different locations of the ascending aorta (section 5.1.3);

It should be noted, that the range of velocity values (and pressure values) presented near each aortic velocity profile is only valid for the particular model. Consequently, the velocity (or pressure) described by a certain color (e.g.: red, representing maximum velocity of 2 m/s) in one particular model describes another (higher or lower) maximum velocity (pressure) value in another model. Therefore, it is of most importance to compare numerical values instead of colors in CFD (otherwise CFD would get a rather different meaning...). All above itemized velocity pictures (and invariantly all distributions of pressure and wall shear stress) for each

pulsatile simulated model (non-stenotic fully open BAV, Type 0 lateral-ND/SD/MD/BD, Type 0 anterior-posterior-ND/SD/MD/BD and Type 1 L/R-ND/SD/MD/BD, defined in section 4.2.1) are presented in early systole ($t = 0.1$ s, time instance of maximum acceleration of blood), peak systole ($t = 0.18$ s, maximum velocity) and late systole ($t = 0.26$ s, maximum decceleration). In all presented results to follow (excluding SD, MD models and simulations in exercise conditions, since only particular cases are presented), each comparative series of pictures contains four plots beginning with the non-stenotic fully open BAV model (as a model of reference) at the top left side (tl), proceeding with Type 0 lateral model located at the top right side (tr), Type 0 anterior-posterior at bottom left (bl) and Type 1 L/R at bottom right (br) side.

5.1.1. Velocity Field in the Symmetry Plane

The velocity distribution of the healthy reference model depicted in figures 5.1 to ?? (top left pictures) shows qualitative and quantitative similarity with the flow description emphasized in section 3.1.4.

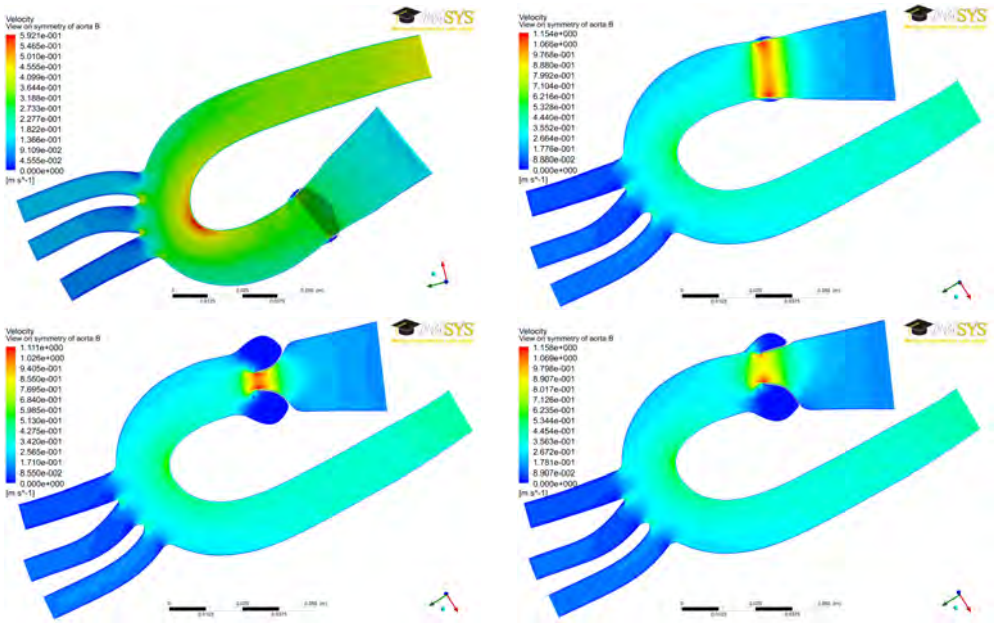

Figure 5.1.: Velocity contour plot at $t = 0.1$ s for non-stenotic fully open BAV (tl), Type 0 lateral-ND (tr), Type 0 anterior-posterior-ND (bl) and Type 1 L/R-ND (br)

Maximum velocity for the healthy (h) configuration ($v_h^{max} = 1.9$ m/s), as expected from the preliminary discussion can be found at the inner portion of the aortic arch at peak systole ($t = 0.18$ s).

The simulated blood flow velocity at peak systole (ps) averaged over the entire aortic cross section (v_h^{ps}) yields about 1.2 m/s for the ascending aorta. Flow separation at the ascending aortic wall is absent in the healthy configuration.

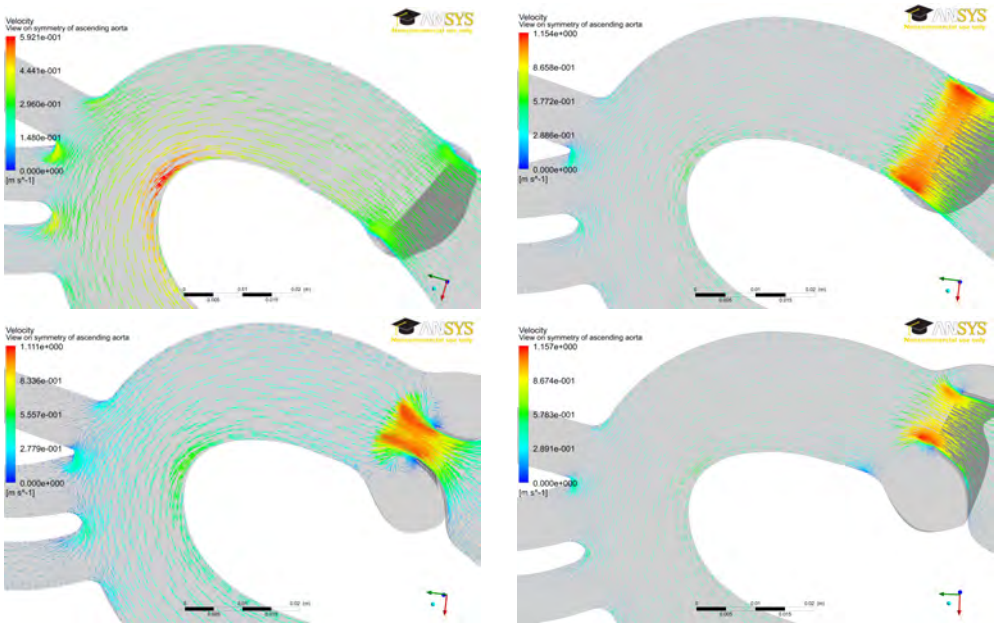

Figure 5.2.: Velocity arrows at $t = 0.1$ s for non-stenotic fully open BAV (tl), Type 0 lateral-ND (tr), Type 0 anterior-posterior-ND (bl) and Type 1 L/R-ND (br)

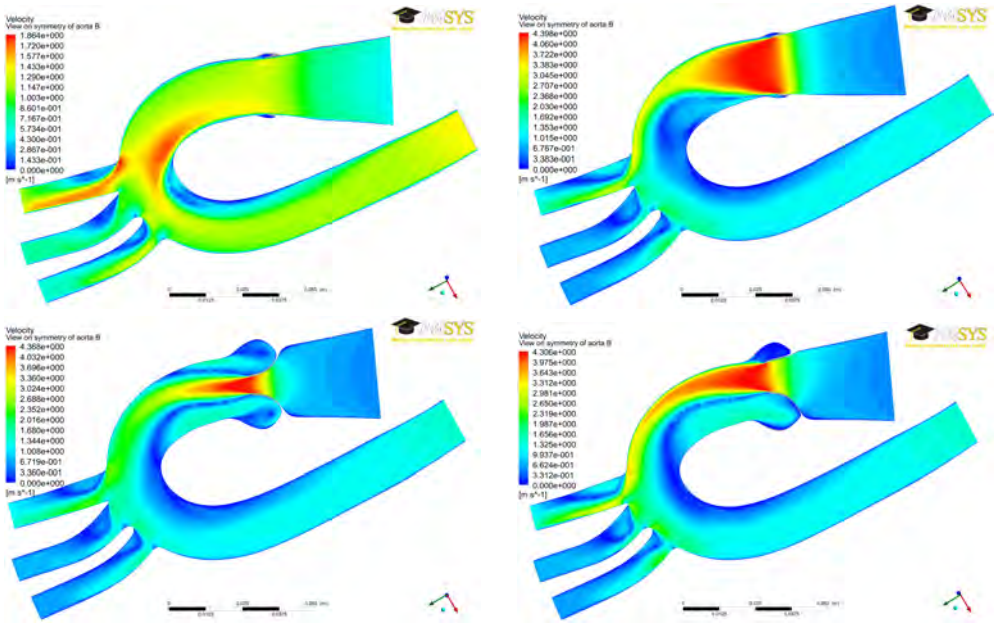

Figure 5.3.: Velocity contour plot at $t = 0.18$ s for non-stenotic fully open BAV (tl), Type 0 lateral-ND (tr), Type 0 anterior-posterior-ND (bl) and Type 1 L/R-ND (br)

A comparison with axial velocity profiles found in [52] shows qualitative agreement with flow patterns depicted in figures 5.9 (tl) to 5.12 (tl) for systolic acceleration, systolic peak

and systolic deceleration, especially at the three cranial cross sections. In the three cross sections near the aortic valve, backflow (as observed in the deceleration phase of the flow model in [52]) cannot be observed in the actual flow model.

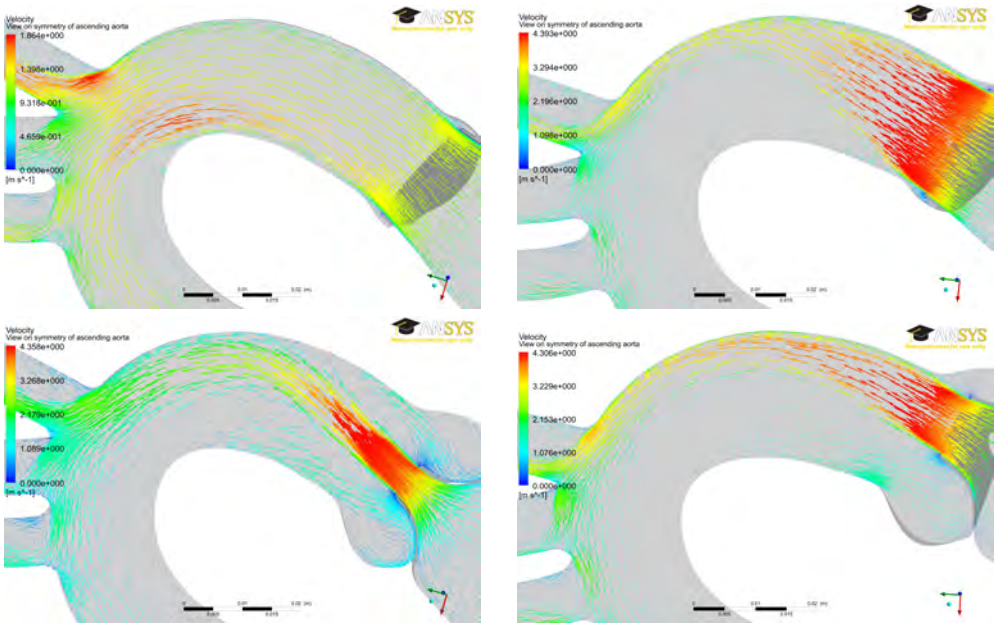

Figure 5.4.: Velocity arrows at $t = 0.18$ s for non-stenotic fully open BAV (tl), Type 0 lateral-ND (tr), Type 0 anterior-posterior-ND (bl) and Type 1 L/R-ND (br)

A global comparison of the healthy configuration with [54,57,30,58] also yields a qualitative matching of velocity profiles gained in the presented simulations. A quantitative comparison between the studies is difficult, since each simulation was carried out with different boundary conditions.

Notheless, the qualitative matching with representative aortic flow simulations and experiments in combination with a good quantitative accordance with well accepted textbook data [22,45,50] gradually transforms the theoretical flow model to a reliable prediction of physiological aortic flow.

This accordance underlines the fact, that the actual choice of boundary conditions, solver strategies and mesh size lead to a well converged simulation appropriately predicting the observed aortic velocity field.

5.1.2. Velocity Contour Plots and Arrows in Crossections

The flow distribution in all pathologic cases shown in figures 5.1 to 5.6 and figures 5.7 to 5.12 (Type 0 lateral-ND, Type 0 anterior-posterior-ND and Type 1 L/R-ND, see also section 5.1.2 for velocity profiles in different cross sections of the aortic geometry) are characterized by a localized high velocity jet impinging at the outer ascending aortic wall where most frequently aortic dissections are located (see section 3.2.2.

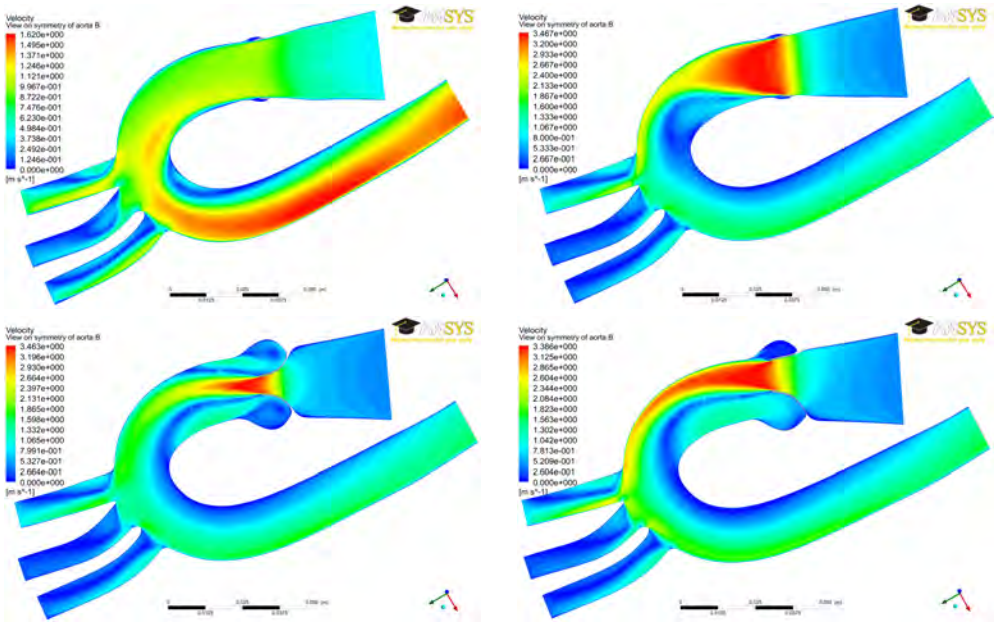

Figure 5.5.: Velocity contour plot at $t = 0.26$ s for non-stenotic fully open BAV (tl), Type 0 lateral-ND (tr), Type 0 anterior-posterior-ND (bl) and Type 1 L/R-ND (br)

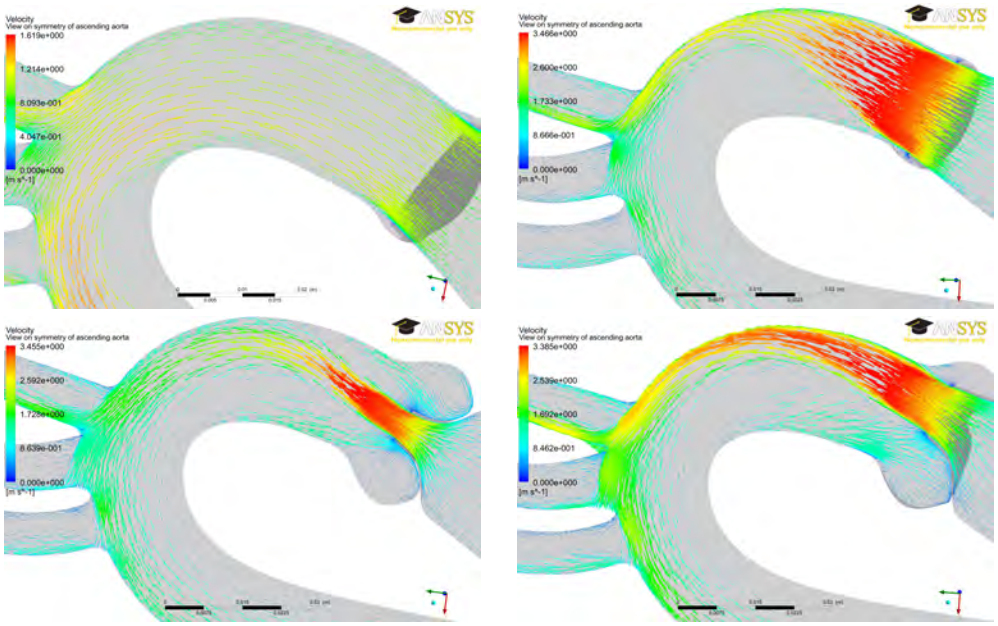

Figure 5.6.: Velocity arrows at $t = 0.26$ s for non-stenotic fully open BAV (tl), Type 0 lateral-ND (tr), Type 0 anterior-posterior-ND (bl) and Type 1 L/R-ND (br)

Maximum jet velocity at peak systole in the pathologic case (p) is $v^p_{max} = 4.4$ m/s in Type 0 BAV and $v^p_{max} = 4.3$ m/s in Type 1 BAV, consequently increasing dynamic pressure on the

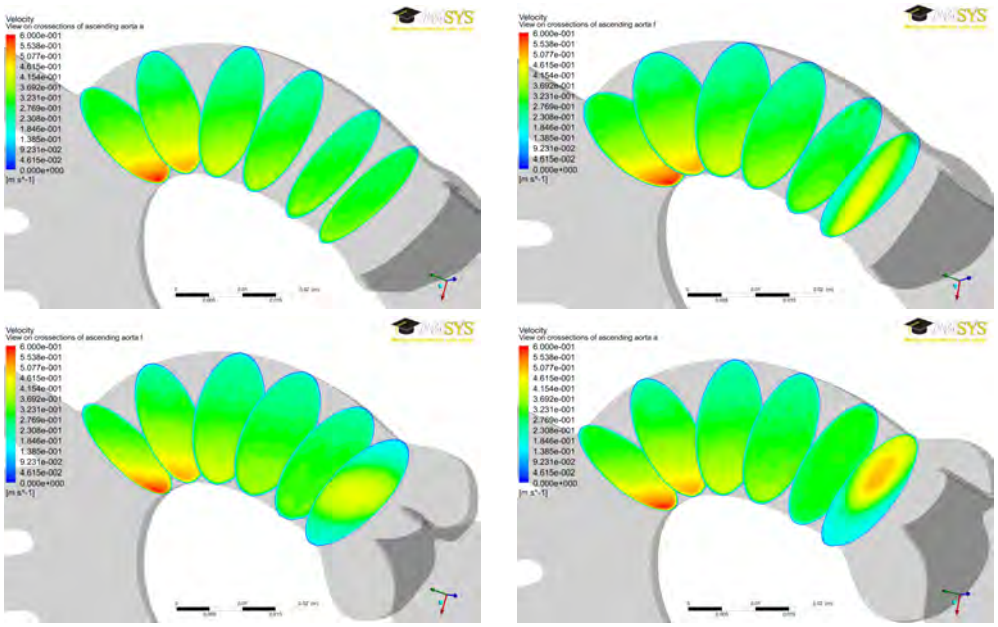

Figure 5.7.: Velocity contour plot at $t = 0.1$ s for non-stenotic fully open BAV (tl), Type 0 lateral-ND (tr), Type 0 anterior-posterior-ND (bl) and Type 1 L/R-ND (br)

aortic wall.

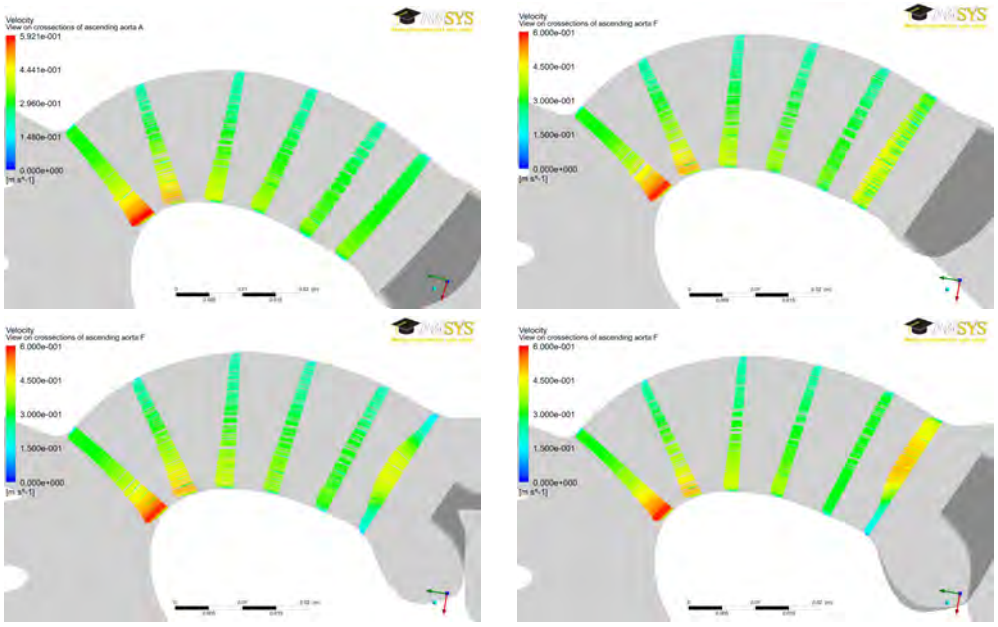

Figure 5.8.: Velocity arrows at $t = 0.1$ s for non-stenotic fully open BAV (tl), Type 0 lateral-ND (tr), Type 0 anterior-posterior-ND (bl) and Type 1 L/R-ND (br)

Lateral from the high velocity jet, flow is forming a three dimensional vertex (see also the

following results concerning secondary flow patterns), which causes retrograde flow back to the aortic valve (a phenomenon which adds to the physiologic vertex behind the valve cusps).

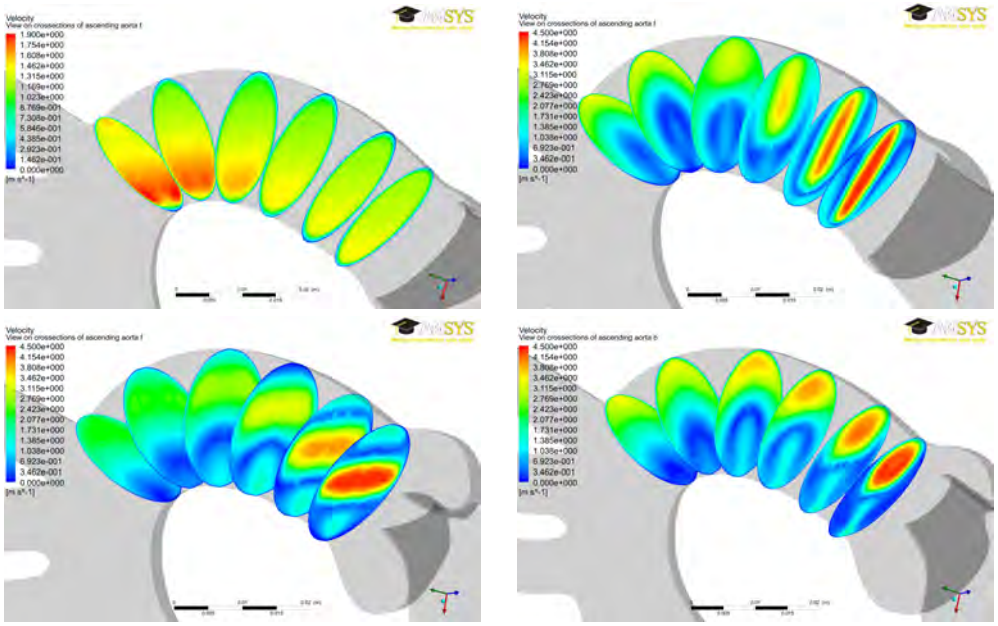

Figure 5.9.: Velocity contour plot at $t = 0.18$ s for non-stenotic fully open BAV (tl), Type 0 lateral-ND (tr), Type 0 anterior-posterior-ND (bl) and Type 1 L/R-ND (br)

Flow separation (flow stagnation point) occurs at the inner aortic wall shortly after beginning of the aortic arch in all stenotic models, causing especially low wall shear stresses in these regions. Obviously, velocity is higher at the outer wall with respect to the inner wall of the aortic curvature (which is vice verca as in the physiologic case).

The ascending aortic flow distribution of Type 0 anterior-posterior BAV can (qualitatively) be compared with the simulations found in [53]. Flow patterns in acceleration and deceleration phase $t = 0.1$ s and $t = 0.26$ s both show the same features (jet, flow separation at the inner wall and vertex at the inner curvature) as described in the paper.

Comparable simulations for the Type 1 BAV model could not be found during the literature survey, but since severe aortic valve stenosis is (for example) described by maximum blood flow velocities (at the location of the aortic valve) greater than 4 m/s (see section 4.2), there is good evidence, that the velocity jet impinging the wall in the actual Type 1 model at peak systole describes the nature of flow quite well.

Additionally, the velocity jet produced by the stenosed bicuspid aortic valve can also be observed in the simulations carried out in [33], although the difference in peak velocity between healthy (tricuspid valve) and pathologic (bicuspid valve) model is less dominant (obviously because of the less dominant difference in valve orifice area).

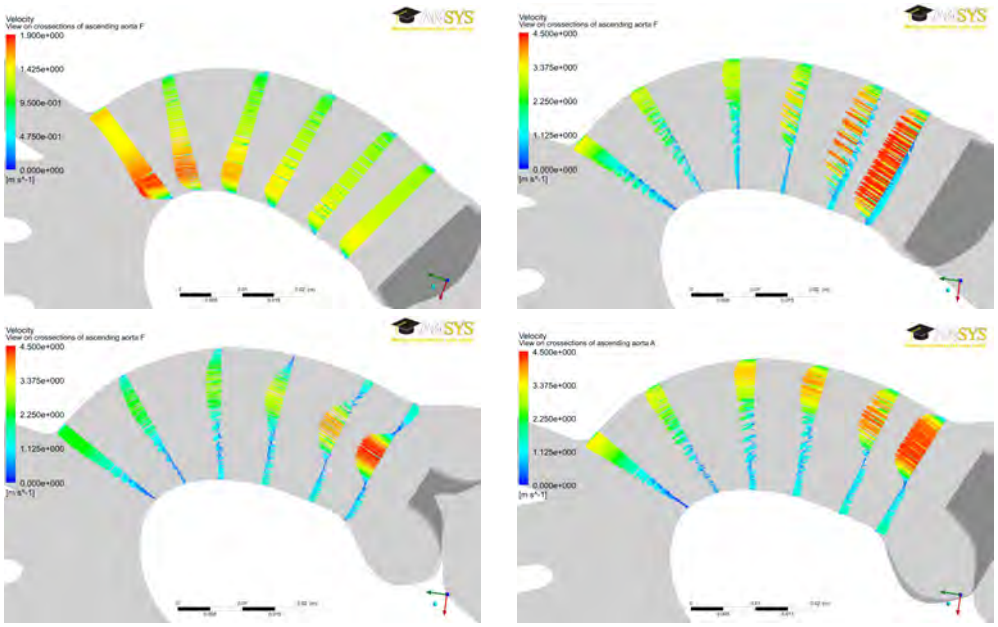

Figure 5.10.: Velocity arrows at $t = 0.18$ s for non-stenotic fully open BAV (tl), Type 0 lateral-ND (tr), Type 0 anterior-posterior-ND (bl) and Type 1 L/R-ND (br)

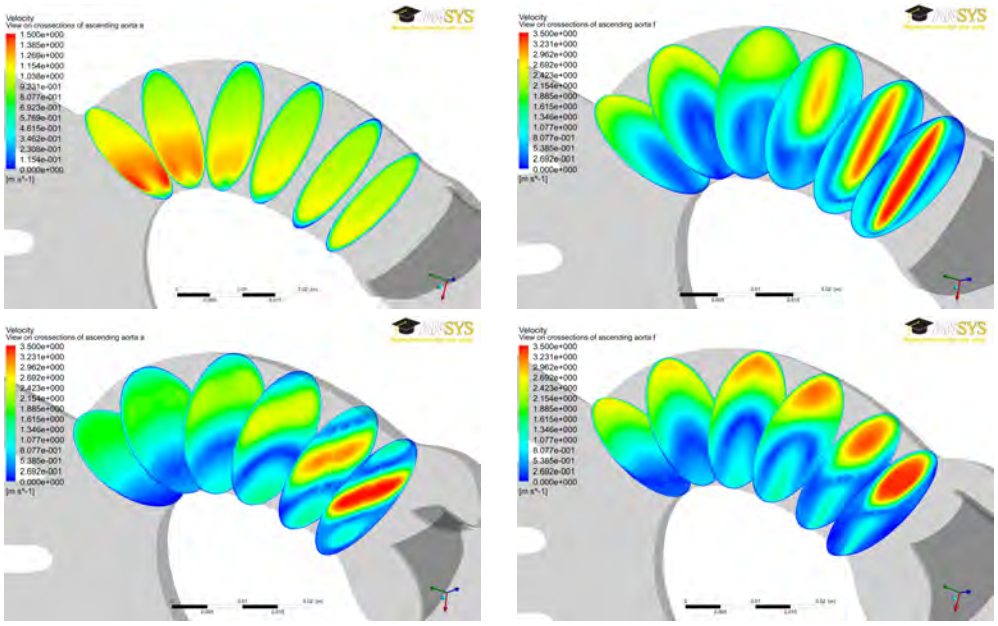

Figure 5.11.: Velocity contour plot at $t = 0.26$ s for non-stenotic fully open BAV (tl), Type 0 lateral-ND (tr), Type 0 anterior-posterior-ND (bl) and Type 1 L/R-ND (br)

5.1.3. Secondary Flow Patterns

Secondary flow patterns describe the tangential projection of the velocity field in a cross section perpendicular to the aortic wall. Due to the fact, that the aortic geometry within

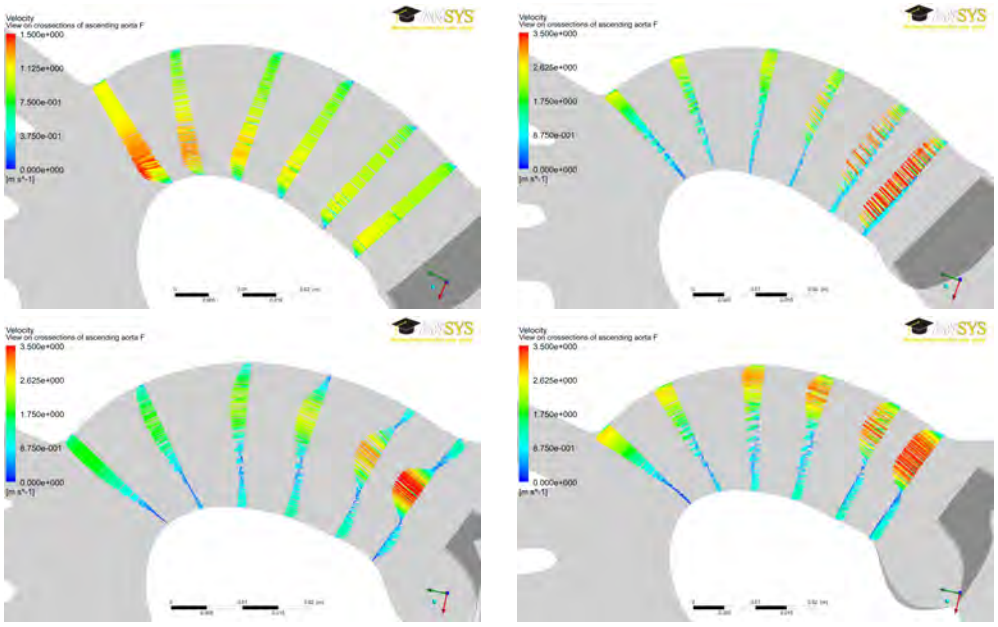

Figure 5.12.: Velocity arrows at $t = 0.26$ s for non-stenotic fully open BAV (tl), Type 0 lateral-ND (tr), Type 0 anterior-posterior-ND (bl) and Type 1 L/R-ND (br)

all presented models is purely symmetric, secondary flow patterns consequently are also symmetric.

As it was expected from the discussion in section 3.1.4, the tangential projection of velocity depicted in figure 5.13, 5.14 and 5.15 shows symmetric vortexes which rotate counterclockwise.

Interestingly, maximum secondary flow at peak systole is nearly twofold higher in Type 0 lateral and Type 1 L/R models than in Type 0 anterior-posterior BAV model.

If the aortic geometry would be slightly asymmetric against the longitudinal axis (as it is in the human body), secondary flow patterns (in healthy aortic geometries) would probably look like helices as they can be shown by the help of MR-techniques [58] or in simulations with more realistic (asymmetric) aortic geometries [51].

Abnormal asymmetric helical flow can also be seen in MR evaluations [59] of ascending aortic systolic flow patterns in bicuspid aortic valves.

5.2. Pressure Distribution at Rest

Total pressure p_t (= dynamic pressure p_d + static pressure p_s) as the physical quantity acting directly (perpendicular) onto the aortic wall is one of the mature determining hemodynamic factors of arterial structural integrity. Results are presented in the same manner as in the preceding section. A proceeding structural analysis among the maximum values of total pressure acting on the ascending aortic wall may provide a useful tool for understanding the mechanism of AD development.

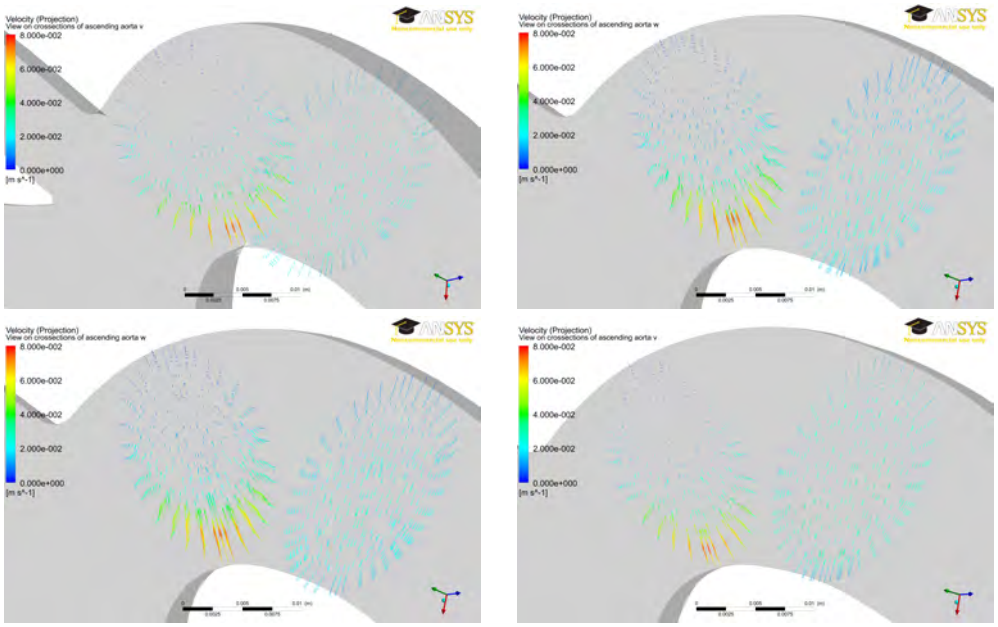

Figure 5.13.: Secondary flow at $t = 0.1$ s for non-stenotic fully open BAV (tl), Type 0 lateral-ND (tr), Type 0 anterior-posterior-ND (bl) and Type 1 L/R-ND (br)

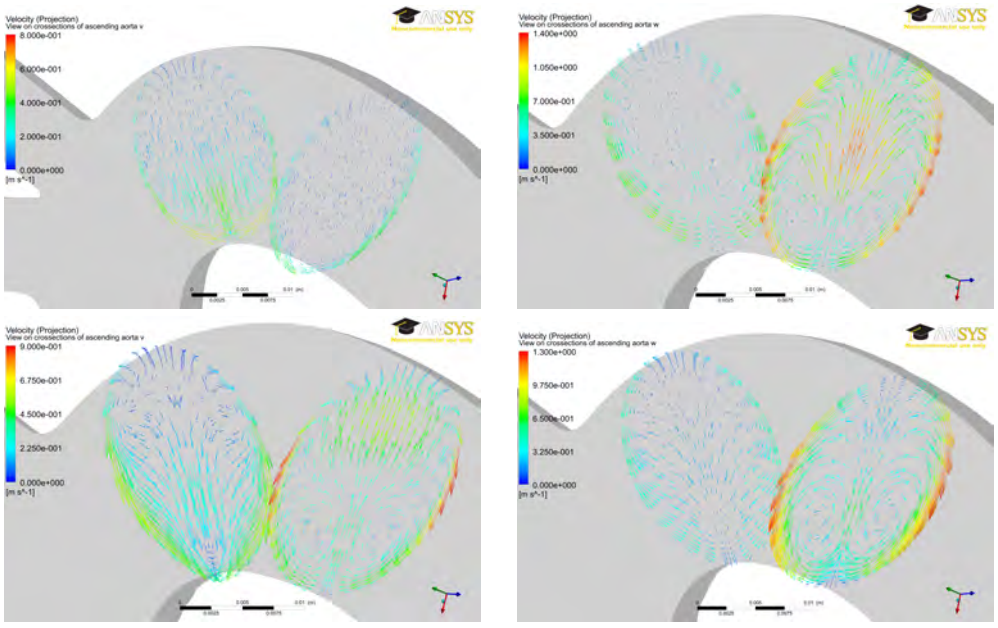

Figure 5.14.: Secondary flow at $t = 0.18$ s for non-stenotic fully open BAV (tl), Type 0 lateral-ND (tr), Type 0 anterior-posterior-ND (bl) and Type 1 L/R-ND (br)

5.2.1. Total Pressure Contour Plots at the Ascending Aortic Wall

The outlet boundary (abdominal aorta) was set to constant zero static pressure. Therefore, all values of total pressure at $t = 0.1$ s (early systole, acceleration phase), $t = 0.18$ s

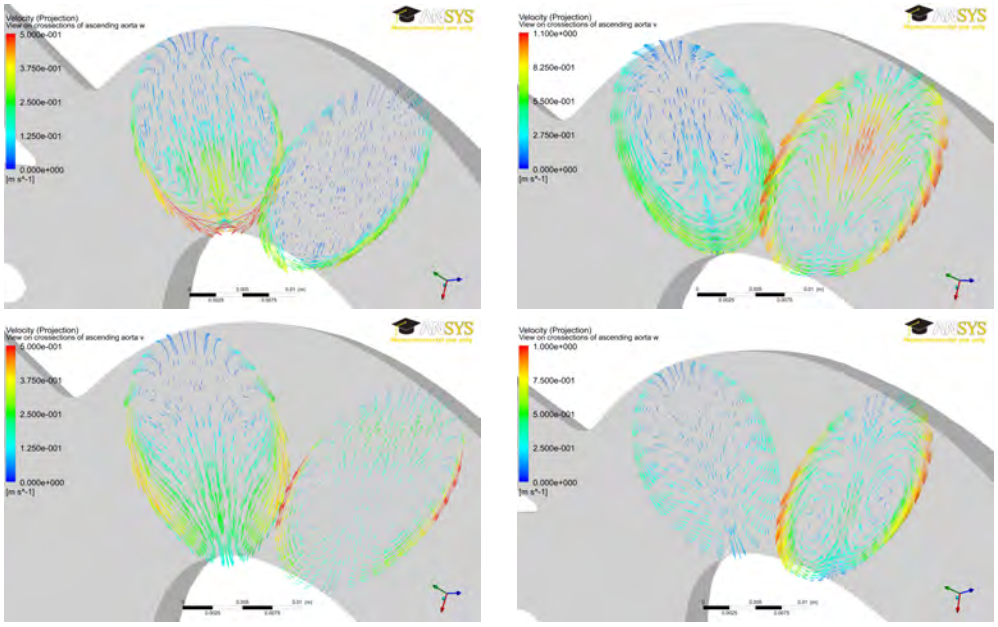

Figure 5.15.: Secondary flow at $t = 0.26$ s for non-stenotic fully open BAV (tl), Type 0 lateral-ND (tr), Type 0 anterior-posterior-ND (bl) and Type 1 L/R-ND (br)

(peak systole) and $t = 0.26$ s (late systole, deceleration phase) must be superimposed by the particular values from the pressure distribution of picture 4.6 in section 4.2.2. Total physiologic and pathologic pressure values are then gained by subtracting simulated total pressure values at the location of descending aorta from above derived values. This procedure holds true, because total pressure is defined as the sum of static pressure and dynamic pressure.

Simulated [41] descending aortic pressure at $t = 0.1$ s (coinciding with $t = 3.44$ s in figure 4.6) is about 103 mmHg, 117 mmHg at $t = 0.18$ s (respectively $t = 3.52$ s in figure 4.6) and 117 mmHg at $t = 0.26$ s (respectively $t = 3.6$ s in figure 4.6).

Superimposing these values with the pressure values gained in the actual simulations and subtracting the simulated descending pressure value (p_{des}) yields physiologic total pressure values at the outer portion of the ascending aortic wall (non-stenotic fully open BAV model) of about $p_{asc}(t = 0.1s) = 140$ mmHg, $p_{asc}(t = 0.18s) = 121$ mmHg and $p_{asc}(t = 0.26s) = 120$ mmHg. Pressure values at $t = 0.1$ s should be less than predicted within this model. The great pressure gradient between ascending and descending aorta (see figure 5.16 (tl)) results from acceleration forces which are superior in this phase of early systole. Physically, this phenomenon is explicable by the aid of inviscid Navier Stokes Equation (see section C.0.5 in appendix). In vitro experiments in living dogs [22] underline the physiologic effect of acceleration forces on blood pressure gradients. Nevertheless, the actual model overestimates this effect (most probably because of the neglection of aortic wall elasticity and static boundary condition at the outlet). Total pressure at $t = 0.18$ s (peak systole) and $t = 0.26$ s (late systole) on the other hand predicts reality quite well (even without regarding

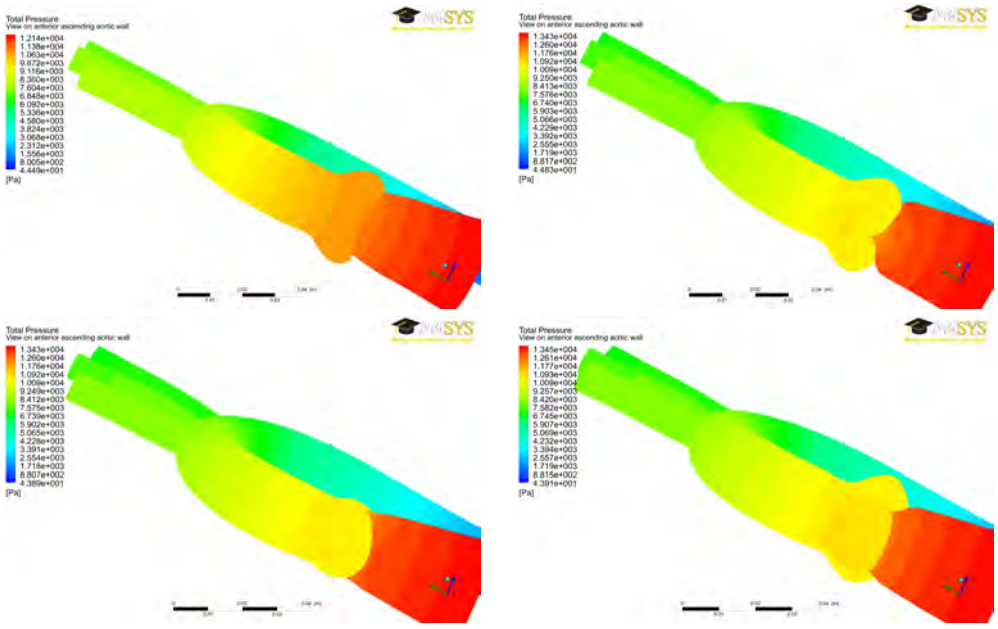

Figure 5.16.: Wall pressure at $t = 0.1$ s for non-stenotic fully open BAV (tl), Type 0 lateral-ND (tr), Type 0 anterior-posterior-ND (bl) and Type 1 L/R-ND (br)

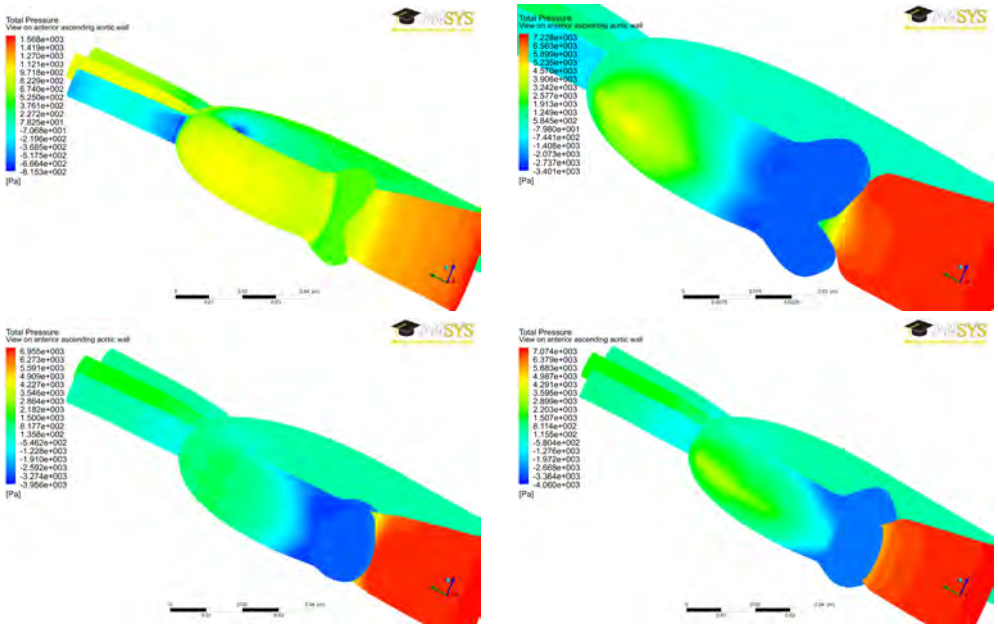

Figure 5.17.: Wall pressure at $t = 0.18$ s for non-stenotic fully open BAV (tl), Type 0 lateral-ND (tr), Type 0 anterior-posterior-ND (bl) and Type 1 L/R-ND (br)

elasticity and wave reflections), since the pressure difference between averaged total blood

pressure over the first cross section after the aortic valve (depicted in figure 5.20 (tl)) and predicted peak systolic descending aortic pressure of about 3 mmHg nearly coincides with those values found in literature [41] and in standard text books.

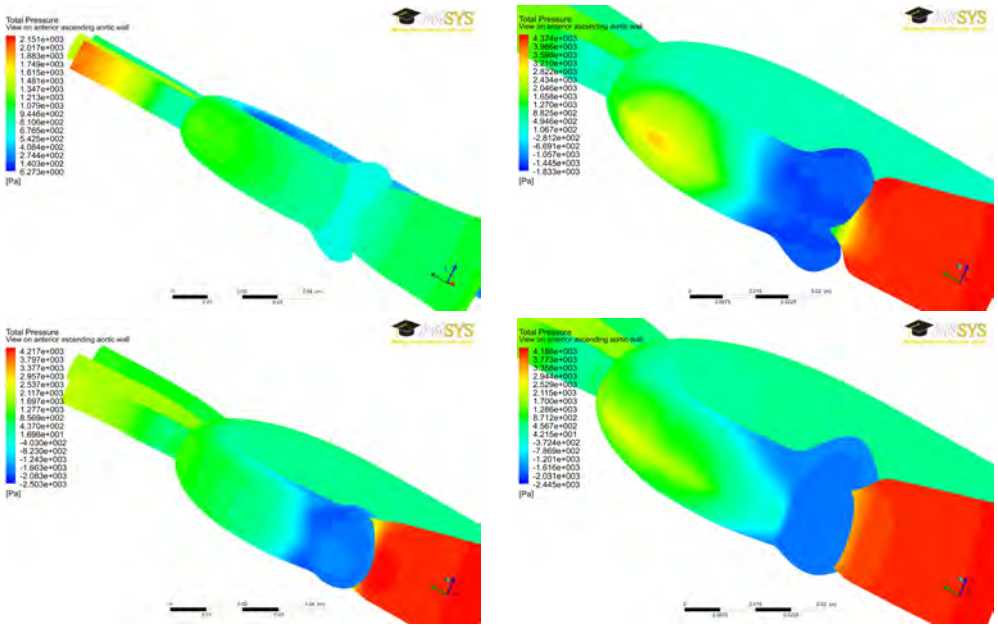

Figure 5.18.: Wall pressure at $t = 0.26$ s for non-stenotic fully open BAV (tl), Type 0 lateral-ND (tr), Type 0 anterior-posterior-ND (bl) and Type 1 L/R-ND (br)

At the same location, total pressure values for Type 0 lateral-ND are $p_{asc}(t = 0.1s) = 140mmHg$, $p_{asc}(t = 0.18s) = 154mmHg$ and $p_{asc}(t = 0.26s) = 139mmHg$. For Type 0 anterior-posterior-ND, total pressure values are lower: $p_{asc}(t = 0.1s) = 140mmHg$, $p_{asc}(t = 0.18s) = 132mmHg$ and $p_{asc}(t = 0.26s) = 124mmHg$. Values for Type 1 L/R-ND approximately coincide with those of the Type 0 lateral model: $p_{asc}(t = 0.1s) = 140mmHg$, $p_{asc}(t = 0.18s) = 150mmHg$ and $p_{asc}(t = 0.26s) = 135mmHg$.

5.2.2. Total Pressure Contour Plots in Crossections

Early systolic values are overestimated as described above. Peak systolic pressure values at the outer ascending aortic wall in stenotic BAV models are mainly determined by the high velocity jet. There, dynamic pressure (Total pressure equals static pressure plus dynamic pressure) is the major responsible factor of wall stress. The most affected region in Type 0 lateral and Type 1 L/R models uniquely is the usual location of DeBakey Type 1 Dissections (see section 3.2.2). In the Type 0 anterior-posterior model, where the jet is directed more centrally (see figure 5.10 (bl)), wall pressures are significantly lower.

Beside the values at the aortic wall, peak systolic pressure values in the left ventricle ($\approx$ 170 mmHg, figure 5.17 (tr,bl,br)) jibe with those values found in standard pathologic texts concerning left ventricular pressure in severly stenosed aortic valves [45].

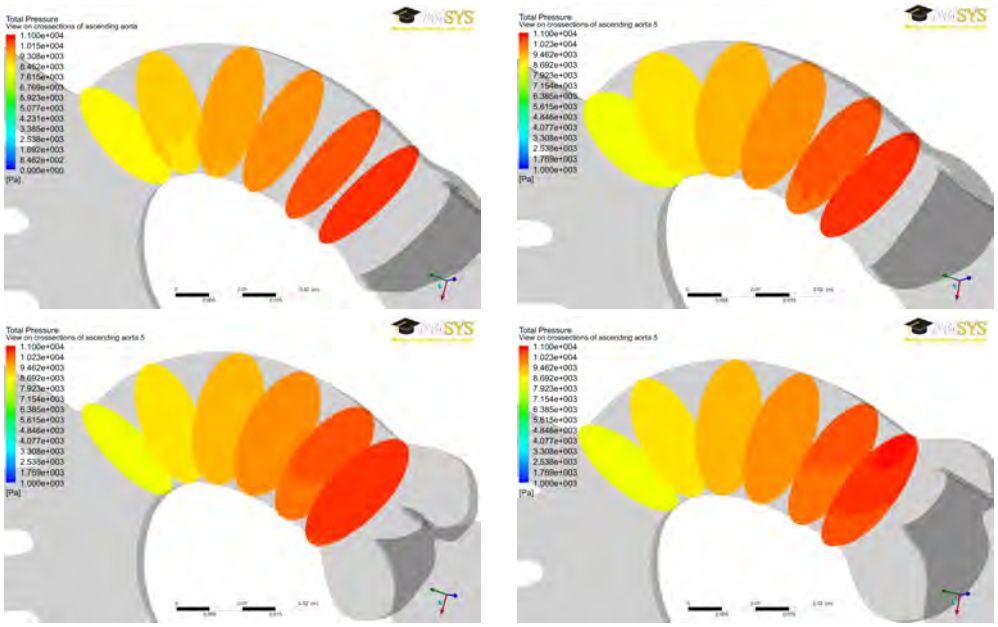

Figure 5.19.: Pressure in crossections at $t = 0.1$ s for non-stenotic fully open BAV (tl), Type 0 lateral-ND (tr), Type 0 anterior-posterior-ND (bl) and Type 1 L/R-ND (br)

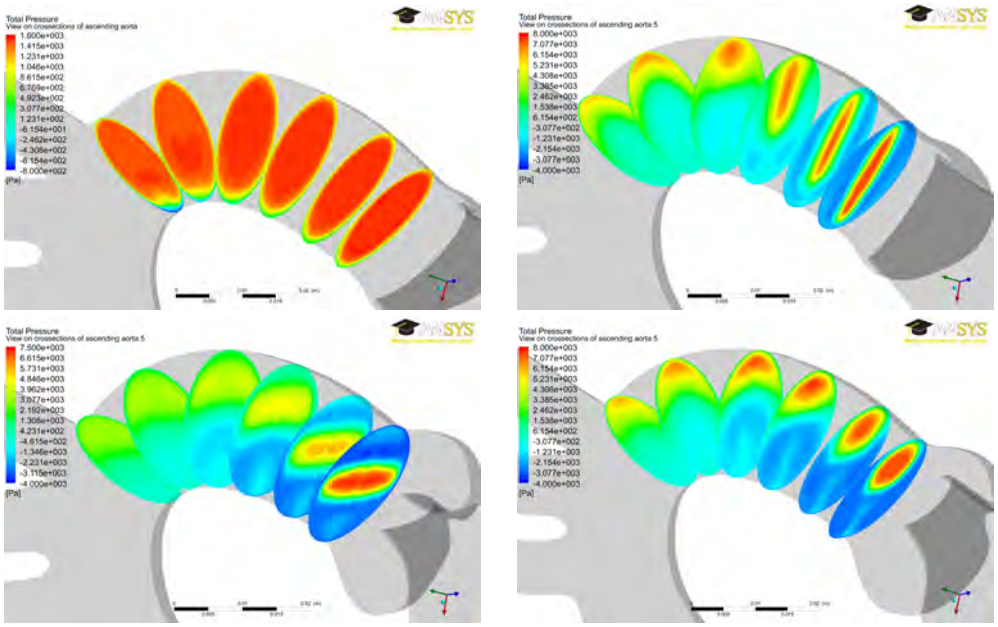

Figure 5.20.: Pressure in crossections at $t = 0.18$ s for non-stenotic fully open BAV (tl), Type 0 lateral-ND (tr), Type 0 anterior-posterior-ND (bl) and Type 1 L/R-ND (br)

Since hypertrophy is discussed (section 3.2.2) as the major determining factor in Aortic

Dissection formation, there is a high evidence that among the discussed models, Type 0 lateral and Type 1 L/R indeed are responsible for this particular pathology. This becomes certain by comparing the definition of mild (systolic blood pressure between 140 and 159 mmHg) and semi- severe (systolic blood pressure between 160 and 179 mmHg) hypertrophy [45] and the values gained from the simulations, which range from 150 mmHg to 160 mmHg (peak systole) in resting conditions. In other words, the velocity jet resulting from severe aortic valve stenosis in Type 0 lateral and Type 1 L/R BAV elevates ascending aortic wall pressure to values which coincide with the definition of arterial hypertrophy.

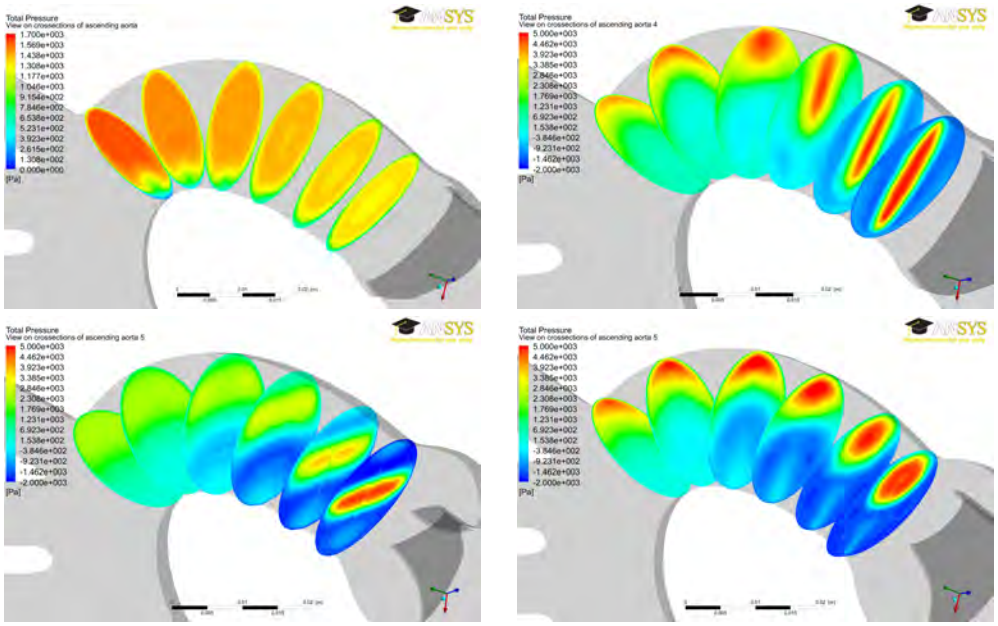

Figure 5.21.: Pressure in crossections at $t = 0.26$ s for non-stenotic fully open BAV (tl), Type 0 lateral-ND (tr), Type 0 anterior-posterior-ND (bl) and Type 1 L/R-ND (br)

Another important and interesting feature of aortic valve stenosis is the fact, that blood pressure is not elevated in all regions of the artery. Even more, the contrary is the case. At the same time instant (peak systole), measured blood pressure in the aorta ($\approx$ 75 mmHg) is much lower than left ventricular pressure ($\approx$ 180 mmHg) in severe aortic valve stenosis [45]. This phenomenon can also be seen by examining simulated total pressure values in several ascending aortic cross sections (figure 5.20). Lateral from the high velocity jet, total pressure values are less than those values found at the descending aorta (therefore the minus sign of blue colored pressure values). Consequently, absolute total pressures lateral from the velocity jet range from 90 mmHg to 100 mmHg which build up a contrast to those (significantly higher) pressure values at the outer portion of the ascending aortic wall. A comparison of the wall pressure distribution between non-stenotic fully open BAV (reference model), Type 0 lateral and Type 1 L/R models along the outer curvature of the aortic geometry yields the impression that in the reference case, pressure decreases smoothely downstream, whereas in the pathologic case, pressure falls abruptly after the location where the jet impinges the wall.

As a consequence, pressure is relatively low (with respect to the jet pressure) at the lateral portions of the aortic arch (figure 5.17 (tr,br)), where the aortic baroreceptor is located (see section 3.1.5). Therefore, the baroreceptor does not recognize the boost of total blood pressure at the outer portion of ascending aortic wall. The parasympathic down- regulation of heart rate, heart contraction and dilatation of peripheral vessels which would be the case in boosts of arterial blood pressure will in this case probably be less prominent or even won´t take place at all. Thence, dynamic pressure caused by the velocity jet won´t be down-regulated and will keep impinging at the aortic wall.

Numerical stress and strain values due to loading of the arterial wall may be effective parameters to show weather the elevated transmural pressure plays a significant role in dissection formation or not. Applying the fundamentals of section E.1 and the strategy of section E.2 onto the above gained pressure values yield stress values σ_r, σ_θ, σ_z and σ_{res}, strains e_r, e_θ,e_z, instantaneous inner radius (r_i) and aortic wall thickness (h) for the outer portion of the ascending aortic wall at peak systole.

According to their hypothetic character, stress and strain values for the aortic wall where placed in appendix E.

5.3. Hemodynamic Values in Exercise Conditions

In physiological exercise (EX) conditions, cardiac output (CO) is strongly elevated due to an increase of stroke volume (SV) and heart rate (HR) with respect to CO at rest. Parallel to an elevation of CO, total pressure, wall shear stress and velocity in the aorta are increased. To assess the relative boost in these hemodynamic quantities, simulations with adapted inlet and outlet boundary conditions (see section 4.2.2) where carried out in the non-stenotic fully open BAV model (reference model) and Type 0 lateral-ND model (pathological stenotic BAV case). The following results are presented within a four-plot-box beginning with the non-stenotic fully open BAV model at rest (tl), furthermore Type 0 lateral-ND (tr), non-stenotic fully open BAV-EX (bl) and Type 0 lateral-ND-EX (br).

Since maximum total pressure and maximum wall shear stress are both found at peak systole, only values at $t = 0.18$ s are presented for the sake of stress analysis. As it was performed in preliminary section 5.2, a systolic pressure value is added to the simulated pressure distribution, since the outlet boundary condition at the abdominal aorta was again chosen as zero static pressure outlet. A physiologic systolic pressure value of 30000 Pa (220 mmHg) at a physical power of 225 W was found in a standard textbook of physiology [45].

Qualitatively, the velocity distribution does not change in comparison with conditions at rest. Maximum velocity is elevated approximately twofold in both cases (non-stenotic fully open and Type 0 lateral BAV model).

Total pressure in both cases is elevated threefold, which results in a total systolic ascending aortic wall pressure of $p_{asc} = 30000Pa + 4251Pa = 34251Pa$ $(220mmHg + 32mmHg = 252mmHg)$ for the physiologic reference case in exercise and respectively $p_{asc} = 30000Pa + 22160Pa = 52160Pa$ $(220mmHg + 166mmHg = 386mmHg)$ for the pathologic case in exercise.

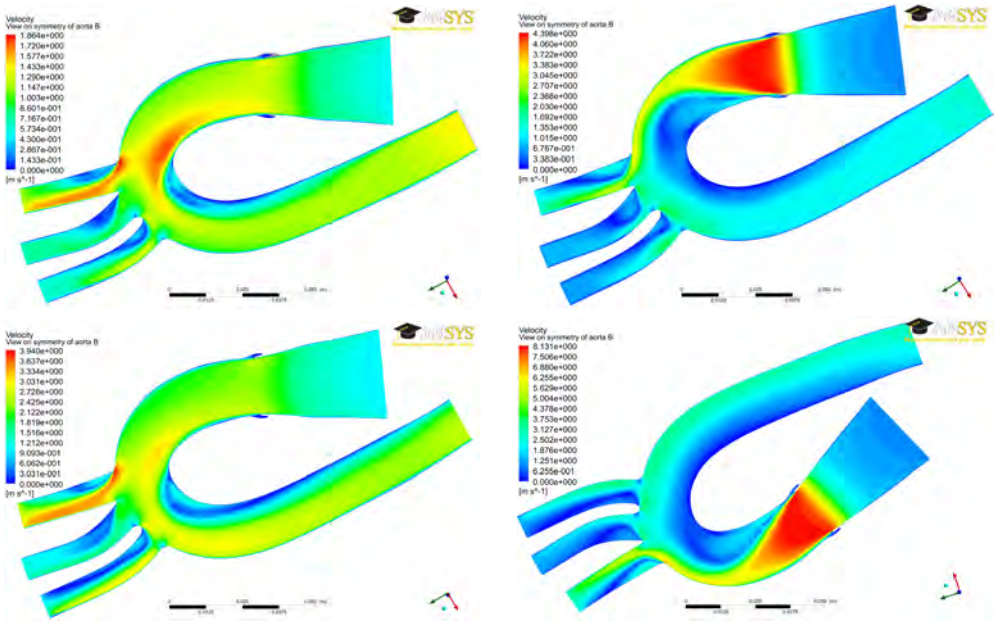

Figure 5.22.: Velocity contour plots (symmetry) at $t = 0.18$ s for non-stenotic fully open BAV (tl), Type 0 lateral-ND (tr), non-stenotic fully open BAV-EX (bl) and Type 0 lateral-ND-EX (br)

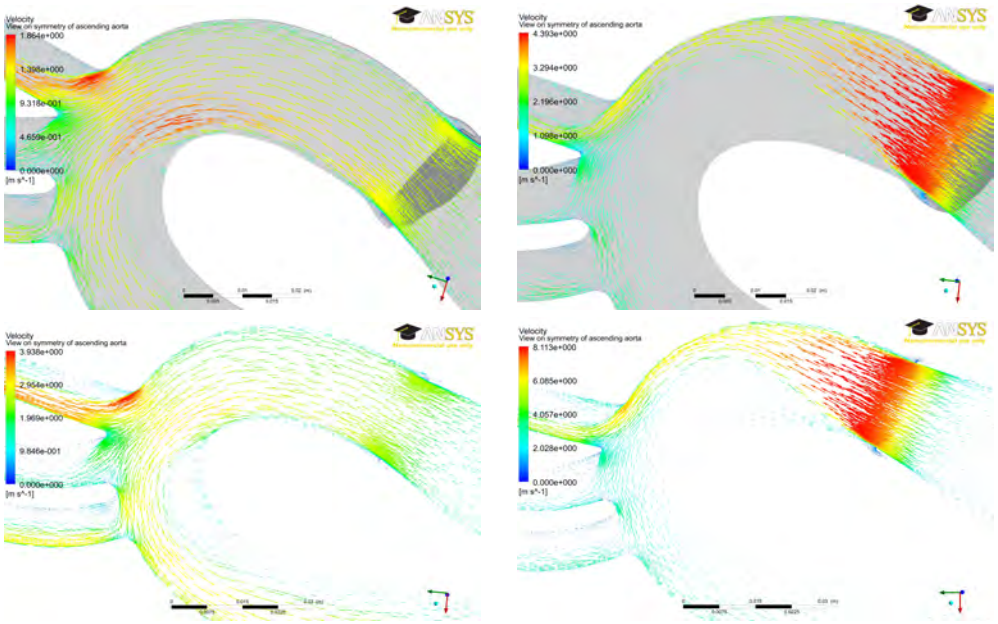

Figure 5.23.: Velocity arrows (symmetry) at $t = 0.18$ s for non-stenotic fully open BAV (tl), Type 0 lateral-ND (tr), non-stenotic fully open BAV-EX (bl) and Type 0 lateral-ND-EX (br)

According to their hypothetic character, stress and strain values for the aortic wall where

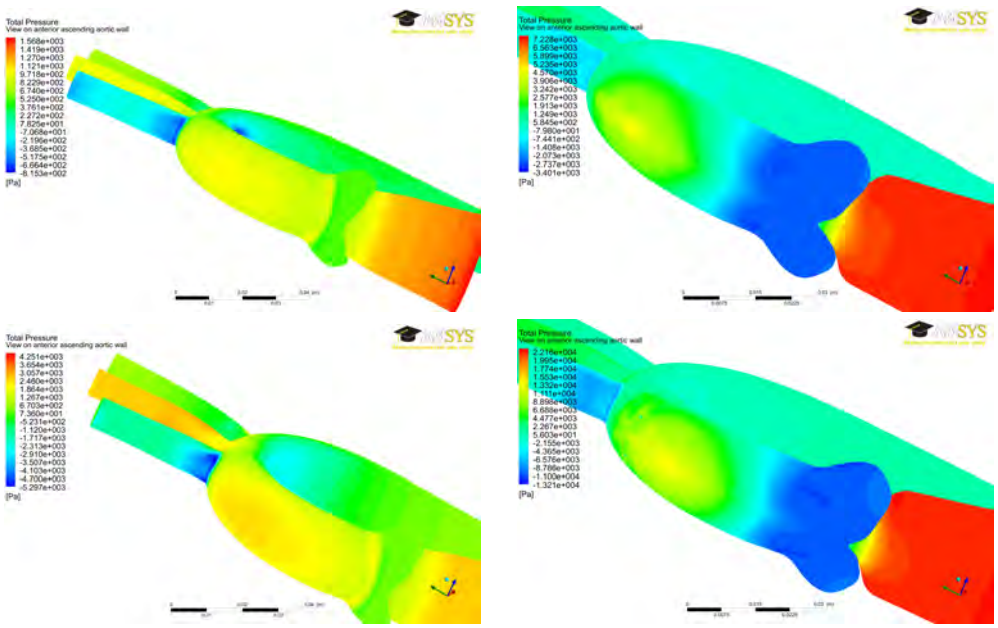

Figure 5.24.: Total pressure (wall) at $t = 0.18$ s for non-stenotic fully open BAV (tl), Type 0 lateral-ND (tr), non-stenotic fully open BAV-EX (bl) and Type 0 lateral-ND-EX (br)

placed in appendix E.

5.4. Ram Pressure Values between dissecting Media Layer

To learn more about the mechanism of aortic dissection growth (after the initial tear of the intima), total pressure values between the separated media layers of the Type 0 lateral model and the Type 1 L/R model are presented for aortic geometries without, with small, medium and big dissections at peak systole ($t = 0.18$ s). The aortic model with small dissection should represent an approximation of the aortic wall status after the above described tear in the tunica intima layer, which propagates further and further downstream due to blow up caused by static ram pressure. Forces, which tend to tear the separated media layers appart are calculated by means of total pressure values multiplied by the approximate surface area of the dissected layer. Forces per unit length can then be compared with experimentally gained ex vivo values.

Total ram pressure p_{ram} is about 5000 Pa in Type 0 lateral-SD model, 6000 Pa in Type 0 lateral-MD and 10000 Pa in Type 0 lateral-BD model (figure 5.25). Slightly lower values can be found in Type 1 L/R-SD, MD and BD model (see figure 5.26). Surface areas for the dissected media layers are $A_{AD} = 0.00024$ m^2 for big dissection model, 0.000048 m^2 for medium dissection and 0.000009 m^2 for small dissection. Since force on the dissected layer F_{AD} can be calculated by $F_{AD} = p_{ram} A_{AD}$. Consequently, F_{AD} for Type 0 lateral-SD

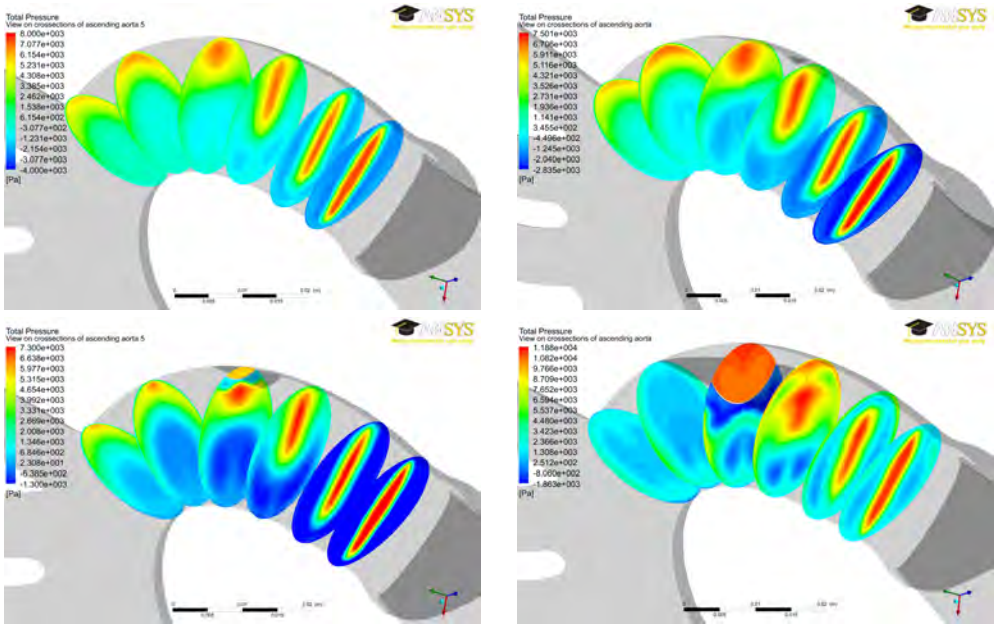

Figure 5.25.: Total pressure in crossections at $t = 0.18$ s for Type 0 lateral-ND (tl), Type 0 lateral-SD (tr), Type 0 lateral-MD (bl) and Type 0 lateral-BD (br)

is 0.045 N, 0.288 N for medium dissection and 2.4 for big dissection. Forces/width obtained from tearing tests protocols (force/width versus dissection path) of medial layers in human abdominal aortic tissue [25] yield values of approximately 23 mN/mm in circumferential direction and 35 mN/mm in longitudinal direction. As F_{AD} is acting onto the entire circumference (0.009 m for SD, 0.022 m for MD and 0.052 m for BD) of the dissected medial layer, values of force/width which try to tear the dissected medial layer further appart are approximately 5 N/m = 5 mN/mm for SD, 13.1 N/m = 13.1 mN/mm for MD and 46.15 N/m = 46.15 mN/mm for BD model. Assuming a bonding force between medial layers as it was found in [25], aortic dissection won´t start to propagate downstream in the Type 0 lateral and Type 1 L/R model at rest.

If the dynamic jet pressure resulting from the stenotic orifice area in exercise conditions is converted into ram pressure ($\approx$ 14000 Pa, see figure 5.24) at the inside of the small dissection, force on the dissected layer $F_{AD} = 0.126$ N ($p_{ram} = 14000$ Pa, $A_{AD} = 0.000009$ m^2) results in force/width = 14 mN/mm (entire circumference of small dissection: 0.009 m), which obviously does not exceed the values gained from the test protocol in [25]. When a ram pressure of $p_{ram} = 14000$ Pa acts onto the medium dissection ($A_{AD} = 0.000048$ m^2, circumference: 0.022 m), force/width (30.55 mN/mm) approaches the value of required dissection force per width. Force/width in the big dissection model is 64.61 mN/mm (twice as high as the required dissecting force). In this advanced case, the dissection will most probably propagate downstream within some heart beats (seconds).

It should be noted, that all above obtained values can naturally vary in a wide range, since every particular aortic dissection may have it´s own geometric characteristic and each blood flow situation may be altered by means of heart valve orifice area, blood jet orientation, wall

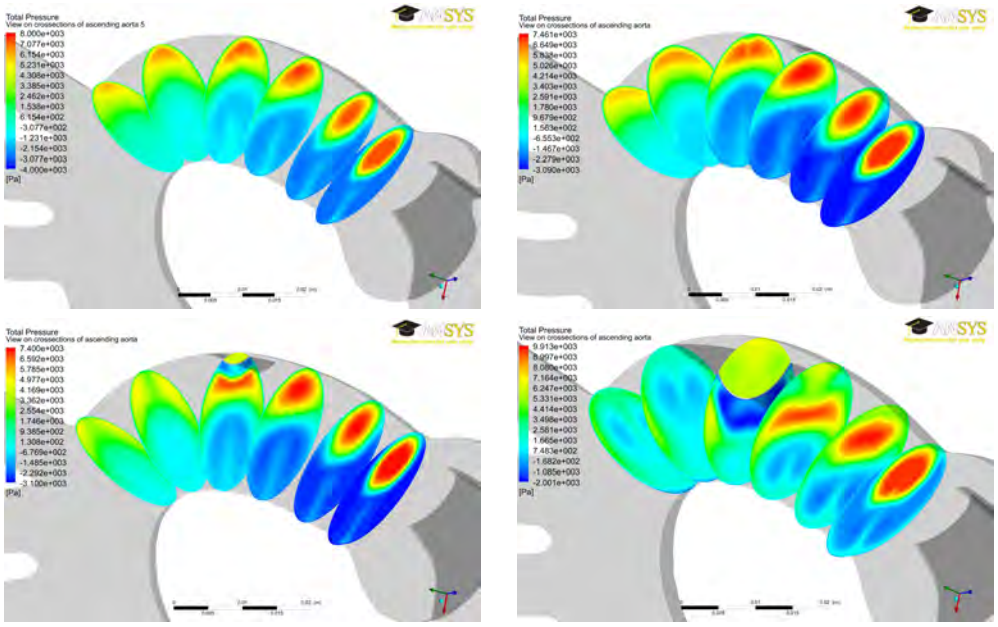

Figure 5.26.: Total pressure in crossections at $t = 0.18$ s for Type 1 L/R-ND (tl), Type 1 L/R-SD (tr), Type 1 L/R-MD (bl) and Type 1 L/R-BD (br)

elasticity, valve leaflet elasticity, strength of the heart, curvature of the aorta, size of the aorta and as many causes again. What´s more, the integrity (the bonding force) of the medial layer, i.e. it´s ability to withstand the dissecting forces caused by static ram pressure, may vary greatly from patient to patient (some aortic tissue will be able to burden higher forces as obtained in [25], others dissect more easily). From a structural mechanical standpoint, the stepwise weakening of the aortic wall (described in the previous section) caused by repeated elevated transmural pressure over a lifetime will most probably additionally decrease the ability of the medial layer to withstand dissecting forces, since the media is the major supporting element of elastic arteries.

All results obtained in this section (in combination with force/width results from [25]) support the idea, that shortly after a small initial intimal tear (provided that the aorta does not blow up immediately) a fast propagation of DeBakey Type 1 dissection downstream is not very likely. Although, the probability of immediate propagation is about three times higher in exercise conditions than in resting conditions. Most probably, it will take some time (hours, days, weeks?) until repeated exposition of the small tear in the aortic wall to ram pressure (rest, exercise) weakens the joint between the layers enough to dissect the layers a little further. This devilish spiral inevitably leads to higher force/width - ratios until it approaches the critical value (23 mN/mm in circumferential direction and 35 mN/mm in longitudinal direction), at which dissection propagation advances within seconds. If otherwise the aortic tissue (especially the media) is weakened severe enough (required force/width values for medial dissection would be highly decreased), the propability of fast propagation of the dissection downstream would clearly be increased.

5.5. Wall Shear Stress Distribution

Some experimental and numerical investigations on blood flow in bicuspid aortic valve disease displayed altered Wall shear stress (WSS) distributions on the ascending aortic wall. As mentioned in section E.2, wall shear stress (WSS) is approximately 4 times lower than Stresses caused by transmural blood pressure. Nonetheless, WSS is discussed to play a major role in regulation of transcriptional events in vascular remodeling (gene expression and extracellular matrix remodeling) [8].

5.5.1. WSS in Aortic models at Rest

Since the discussion concerning the effect on aortic dissection, aortic dilatation and aneurysm formation is still controversial and coined with antagonisms, only uncommented absolute values of WSS are presented. These may provide future investigations within this field of research with some useful data.

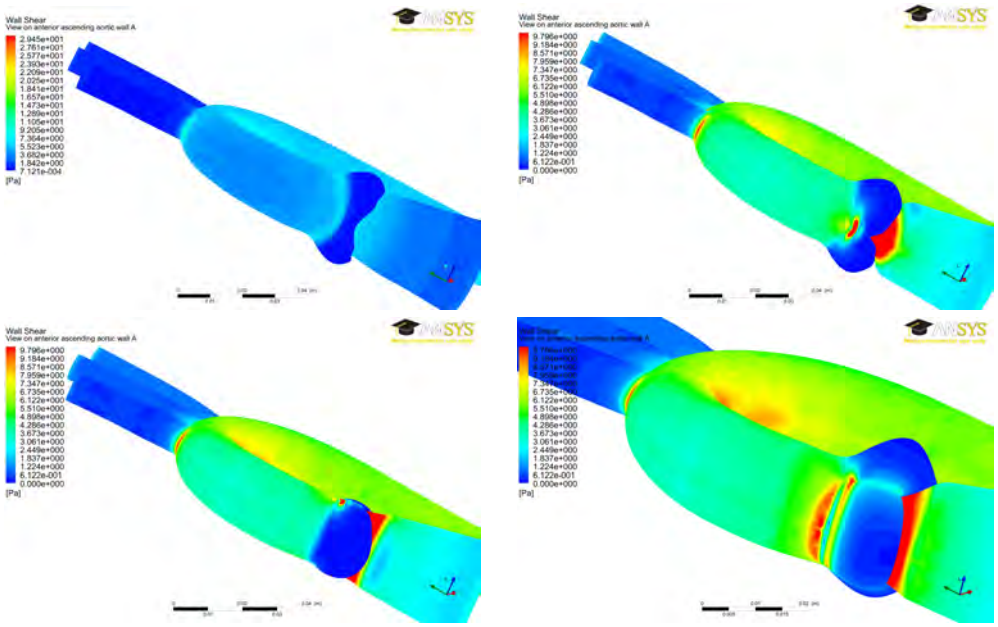

Figure 5.27.: Wall shear stress at $t = 0.1$ s for non-stenotic fully open BAV (tl), Type 0 lateral-ND (tr), Type 0 anterior-posterior-ND (bl) and Type 1 L/R-ND (br)

In comparison with the reference model (see figures 5.27) at $t = 0.18$ s (peak systole), Type 0 lateral-ND (tr) shows 18- fold increased wall shear stress ($WSS_{T0l} = 110$ Pa) at the outer portion of ascending aortic wall. WSS in Type 0 anterior-posterior-ND (bl) and Type 1 L/R-ND (br) is 10 times ($WSS_{T0ap} = 110$ Pa), respectively 17 times ($WSS_{T1} = 110$ Pa) increased.

Approximately the same ratios can be observed at $t = 0.1$ s (acceleration phase) and $t = 0.26$ s (deceleration phase).

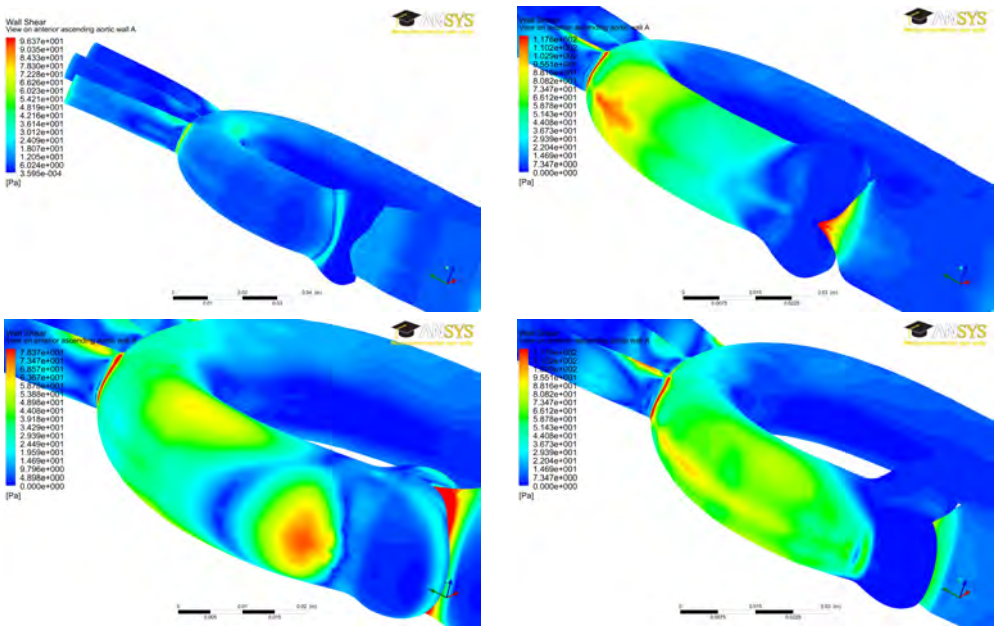

Figure 5.28.: Wall shear stress at $t = 0.18$ s for non-stenotic fully open BAV (tl), Type 0 lateral-ND (tr), Type 0 anterior-posterior-ND (bl) and Type 1 L/R-ND (br)

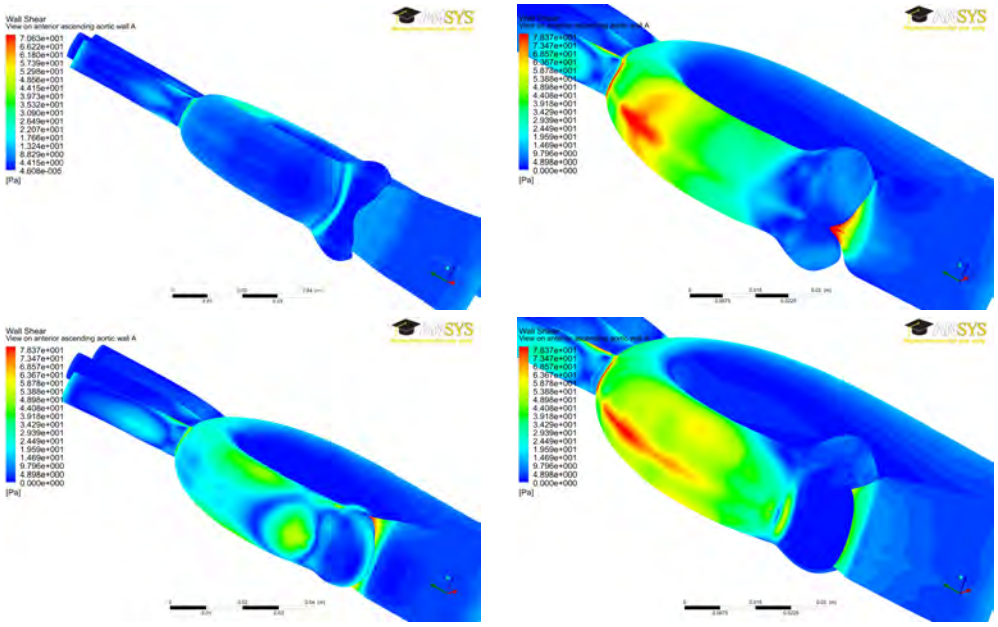

Figure 5.29.: Wall shear stress at $t = 0.26$ s for non-stenotic fully open BAV (tl), Type 0 lateral-ND (tr), Type 0 anterior-posterior-ND (bl) and Type 1 L/R-ND (br)

5.5.2. WSS in Aortic models in Exercise Conditions

In Exercise conditions, WSS on the outer portion of ascending aortic wall is found to be increased approximately 4 times ($WSS_{ns}^{ex} = 110$ Pa) in non-stenotic fully open BAV model

and 63 times ($WSS_{T1}^{ex} = 110$ Pa) with respect to the reference model at rest (see figure 5.30).

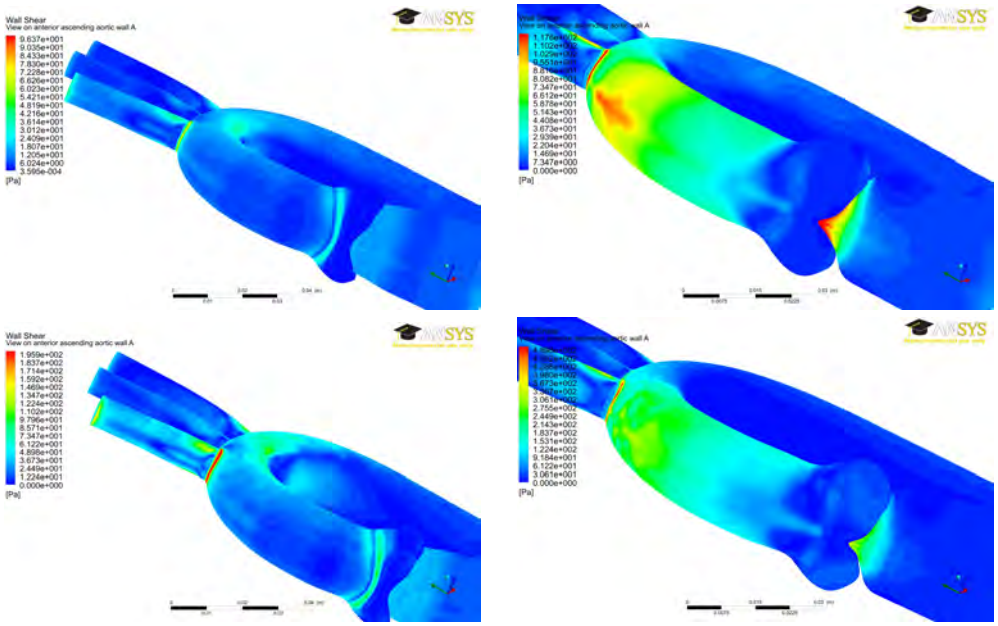

Figure 5.30.: Wall shear stress at $t = 0.18$ s for non-stenotic fully open BAV (tl), Type 0 lateral-ND (tr), non-stenotic fully open BAV-EX (bl) and Type 0 lateral-ND-EX (br)

6. Conclusion

6.1. Conclusion english

By the aid of CFD, it was possible to develop reliable qualitative arterial flow models for completely open (physiologic) and different stenotic bicuspid aortic valve (pathologic) aortic root geometries at rest and exercise. Besides significantly elevated ascending aortic wall pressures on the non-dissected ascending aortic wall, highly increased ram pressures between the already dissected medial layers and wall shear stress could be observed. Limitations concerning the quantitative validity arise from errors and simplifications during the modeling process. Nonetheless, reliable quantitative results could be made by comparing the predictive numerical models with various clinical and biomechanical reference studies. Only validated values where used to answer the questions preliminary stated in chapter 1. Concerning the question, if and how an already existing dissection propagates further in patients with stenotic bicuspid aortic valves, several possible answers where found.

The increase of jet velocity caused by stenotic BAV leads to a significantly increased ram pressure (compared with the fully open physiologic model), which may be a cause or at least a promoting factor of propagation of DeBakey Type I aortic dissection. The effect is less dominant in Type 0 anterior-posterior BAV than it can be observed in Type 0 lateral and Type 1 L/R BAV.

Section E.5, section 5.3 and section 5.2 provided ideas of possible answers on the question of developement of ascending aortic dissection. Arguing from a biomechanical standpoint, the developement of intimal rupture is highly supported by the effect of repeated exposure of the aortic wall to increased dynamic (jet) pressure in stenotic BAV disease, since the physiologic weakening process of aortic tissue is significantly accelerated. Comparison of quantitative interrelations between physiologic and pathologic increased aortic wall stress with tissue weakening processes revealed significantly increased risk of dissection in patients with BAV disease.

6.2. Conclusion german

Durch den Einsatz von CFD war es möglich, zuverlässige qualitative Modelle der Strömung in verschiedenen vergleichbaren Aortenmodellen mit vollständig offenen (physiologische) und stenotisch-bikuspidalen (pathologischen) Aortenwurzelgeometrien in Ruhe und Arbeitsbedingungen zu erstellen. Neben den signifikant erhöhten transmuralen Drücken auf die nicht-dissektierte Wand der aorta ascendens konnten drastisch erhöhte Staudrücke zwischen den schon dissektierten Media-Lamellen und mehrfach erhöhte Wandschubspannungswerte ob-

serviert werden. Limitationen bezüglich der quantitativen Aussagekraft der dargestellten Strömungsmodelle entstanden durch Fehler und Vereinfachungen im Modellierungsprozess, die aus Zeit- und Kostengründen sowie mangels erforderlichem Know-how nicht ausgemerzt werden konnten. Nichtsdestotrotz konnten vertrauenswürdige quantitative Resultate durch Vergleich der numerischen Ergebnisse mit verschiedenen klinischen und biomechanischen Referenzstudien erhalten werden. Nur jene derart validierten Observablen wurden für eine weitere Analyse und Beantwortung der in Kapitel 1 aufgeworfenen Fragen verwendet.

Bezüglich der Frage, ob und wie eine schon ausgebildete Dissektion in Patienten mit stenotischen bikuspidalen Aortenklappen weiter propagiert konnten einige mögliche Antworten gefunden werden. Die stark erhöhte Strömungsgeschwindigkeit durch die pathologisch verengte Klappe (Jetwirkung) führt im Vergleich zur vollständig offenen (gesunden) Klappe zu signifikant erhöhten Staudrücken, was mit hoher Wahrscheinlichkeit der Grund für die weitere (rapide) Propagation der DeBakey Typ I-Dissektion ist. Die Jetwirkung fällt in Typ 0 anterior-posterior bikuspidalen Klappen geringer aus als in Klappen vom Typ 0 lateral und Typ I L/R. Die Berechnung der Kraftspitzen basierend auf den maximalen Staudrücken in Systole und den effektiven Dissektionsflächen, welche die Dissektion weiter auseinander zu reißen trachtet und deren Vergleich mit experimentellen Dissektionskraftwerten aus der Fachliteratur unterstreichen die Signifikanz dieser Vermutungen.

In Kapitel E.5, Kapitel 5.3 und Kapitel 5.2 wurden Ideen entwickelt, um Antworten auf die Frage der initialen Entstehung der Dissektion geben zu können. Argumentiert man aus einem rein biomechanischen Standpunkt heraus, so entsteht der einer Aortendissektion meist vorangehende initiale Riss der tunica intima durch die immer wieder wiederholte Langzeitbelastung der Aortenwand durch den lokal signifikant erhöhten Wanddruck auf die aorta ascendens, welcher ebenfalls ein kausaler Effekt der pathologischen Aortenklappenstenose im bikuspidalen Fall ist. In diesem speziellen pathologischen Fall wird der physiologische Alterungsprozess der Aortenwand beschleunigt. Ein Vergleich von quantitativen Relationen zwischen physiologischen und pathologischen berechneten Wandspannungen mit experimentell gefundenen in vivo und ex vivo Ermüdungserscheinungen des arteriellen Gewebes ergaben ein signifikant erhöhtes Risiko der Ausbildung einer Aortendissektion in Patienten mit stenosierten bikuspidalen Aortenklappen.

A. Mathematical Foundations of Continua

Matter is described as a continuum, more precicely as constitutive material points in Euklidean space. Such material points have to be identifyable. Each material point get´s a unique (in a mathematical sense) 'marker' $\vec{X}$ ('it´s name'). Later on this marker will be called vector. A body B is denoted as a connected compact quantity of material points. The boarder of this point set (the surface of B) is called ∂B. After defining a coordinate system (e.g. cartesian coordinate frame, cylindrical coordinate frame) and setting a point of reverence within this system, the location of all material points can be defined by marking them with a position vector $\vec{x}$ (which arises from the point of reverence). Matter is described as a continuum, more precisely as constitutive material points in Euclidean space. Such material points have to be identifiable. Each material point get´s a unique (in a mathematical sense) 'marker' $\vec{X}$ ('it´s name'). Later on this marker will be called vector. A body B is denoted as a connected compact quantity of material points. The boarder of this point set (the surface of B) is called ∂B. After defining a coordinate system (e.g. Cartesian coordinate frame, cylindrical coordinate frame) and setting a point of reverence within this system, the location of all material points can be defined by marking them with a position vector $\vec{x}$ (which arises from the point of reverence). In a special frame of reverence, like the Cartesian or the cylindrical, the configurations $\vec{x}$ are getting the meaning of vectors or tensors:

- $\vec{x} = (x_1, x_2, x_3)^T$ (position vector $\rightarrow$ Euler coordinates: a supervisor sits fixed at a position $\vec{x}$ and sees, how a material particle $\vec{X}$ passes by)
- $\vec{X} = (X_1, X_2, X_3)^T$ (vectorial markers of the material points $\rightarrow$ Lagrange coordinates: a supervisor follows the material particle $\vec{X}$ on its way through time and space)

If ϕ is a physical quantity of a material point (e.g. pressure, velocity) which can be specified all time, one can define two kinds of descriptions:

- Material description: $\phi = \phi(X_1, X_2, X_3, t; \tau) = \phi(\vec{X}, t; \tau) \rightarrow$ It describes the value of ϕ for a particular material point $\vec{X}$ at time t
- Field description: $\phi = \phi(\vec{X}(\vec{x}, t; \tau), t; \tau) \rightarrow$ It describes the value of ϕ at position $\vec{x}$ at time t

A scalar quantity ϕ, describing a particular physical quantity of a body B in general changes it´s value in time. The material derivative (time dependent change of ϕ for a material particle) $\dot{\phi}$ of this quantity can be derived in the following way:

$$\dot{\phi}(\vec{X},t) = \lim_{\Delta t \to 0} \frac{\phi(\vec{X},t+\Delta t) - \phi(\vec{X},t)}{\Delta t} = \frac{\partial \phi}{\partial t}(\vec{X},t) \tag{A.1}$$

(Differentiation with respect to time t with fixed $\vec{X}$, since material particles are described by the position of their condition of reference $\vec{X}$)

The same quantity can also be differentiated in an Eulerian description:

$$\dot{\phi}(\vec{x},t) = \lim_{\Delta t \to 0} \frac{\phi(\vec{x}+\vec{v}\Delta t, t+\Delta t) - \phi(\vec{x},t)}{\Delta t} = \nabla\phi(\vec{x},t)\cdot\vec{v}(\vec{x},t) + \frac{\partial \phi}{\partial t}(\vec{x},t) \tag{A.2}$$

For a vector field $\vec{u}$ (e.g. velocity or acceleration of a fluid) the material and the field time-derivative are calculated in a similar way:

$$\dot{\vec{u}}(\vec{X},t) = \frac{\partial \vec{u}}{\partial t}(\vec{X},t) \tag{A.3}$$

in the Lagrangian description and respectively

$$\dot{\vec{u}}(\vec{x},t) = \nabla\vec{u}(\vec{x},t)\cdot\vec{v}(\vec{x},t) + \frac{\partial \vec{u}}{\partial t}(\vec{x},t) \tag{A.4}$$

in the Eulerian description.

Mathematically, continuum physics is based on the field- concept (Eulerian description). Macroscopic bodies (such as blood vessels or flowing blood) are said to be a huge collection of infinitesimal material particles. Such a material particle within the continuum approximation contains a large amount of molecules to authorize the continuum description. All quantities and forces acting on these material particles are described by smooth and well defined mathematical functions of spatial coordinates and time. In every point, where such a material particle is placed, a real-valued function of space and time (the field) represents the value of a physical quantity (e.g. force, pressure, velocity,...).

The most important governing equation of motion in continuum mechanics is Newton´s second law, which is the fundamental dynamic equation. It states, that mass times acceleration equals force. Forces can be idealized as single forces with a infinitesimal small point of action. In nature, this assumption no longer holds true, since forces, for example the gravitational force are acting on a finite volume of a body or on the other hand on a finite surface of a body (e.g. forces of friction, viscous forces, pressure forces). Forces in continuum dynamics are therefore separated into volume forces and surface forces. Concerning surface forces it is therefore inevitable to regard the distribution of the force over the surface. A helpful expression which regards this, is the definition of stress. Stress is the force $\Delta\vec{F}$ acting on a unit area $\Delta\vec{A}$, mathematically written as:

$$\sigma = \lim_{\Delta A \to 0} \frac{\Delta \vec{F}}{\Delta \vec{A}} \tag{A.5}$$

For a three dimensional body (e.g. water in a tube, the walls of a tube conducting blood), $\vec{\sigma}$ is a second order tensor with nine components (three components of stress for each direction

in Euclidean space). Examples for stresses are the pressure (acting normal onto a surface, therefore also called 'normal stress') and the shear stress (acting tangential to the surface, therefore called 'tangential stress'). A physical system, also called body B (with a mass m) is a collection of a number N of point particles $(n = 1, 2, 3, \ldots, N)$, where each motion of a single particle is determined by Newton´s second law:

$$m_n \frac{d^2 \vec{x}_n}{dt^2} = \vec{F}_n \tag{A.6}$$

where $\vec{x}_n$ is the instantaneous position of the particle (or body), t is the time and $\vec{F}_n$ is the instantaneous force acting on the particle (or body). Particles (Atoms or molecules, continuous bodies,...) interact with other neighboring particles, so the forces $\vec{F}_n$ may depend on the positions and velocities of all particles within the system. According to Newton´s fundamental dynamic equation and to numerous experiments, three conservation laws (also called 'laws of balance') had been formulated which hold true for solids and liquids:

- Force = Rate of change of (linear) momentum (Conservation of linear momentum)
- Torque = Rate of change of angular momentum (Conservation of angular momentum)
- Power = Rate of change of kinetic energy

The first item together with the stress- strain- formulation and a constitutive equation for a incompressible, viscous, Newtonian liquid and the conservation of mass will lead to the governing equations of motion for incompressible, Newtonian liquids (Navier Stokes Equations). The stress- strain- relationship applied on the conservation of linear momentum plus a material law (Hooke´s law of elasticity) will provide the governing equations of dynamics of a solid structure.

B. Derivation of Governing Equations

In case of general fluid motion, the LEFT SIDE of Newton´s law of motion ($\rho\vec{a} = \vec{f}$) must be separated into a sum of a local acceleration term and a convective acceleration term. The first one contributes to the time rate of change of velocity at constant $\vec{x}$. The convective term describes spatial changes of velocity at constant time. This task can be fulfilled by answering the question, how fast the velocity changes for a *particular* piece of fluid. Watching a fluid particle on it´s way through the fluid, one observes, that it moves $\Delta x = v_x \Delta t,\ \Delta y = v_y \Delta t,\ \Delta z = v_z \Delta t$ in a small time interval Δt and changes it´s velocity from $\vec{v}(x, y, z, t)$ at time t and spatial coordinates x, y, z to the new value $\vec{v}(x + v_x\Delta t, y + v_y\Delta t, z + v_z\Delta t)$ during this movement. A taylor expansion yields:

$$\begin{aligned}\vec{v}(x + v_x\Delta t, &y + v_y\Delta t, z + v_z\Delta t) \\ &= \vec{v}(x, y, z, t) + \frac{\partial\vec{v}}{\partial x}v_x\Delta t + \frac{\partial\vec{v}}{\partial y}v_y\Delta t + \frac{\partial\vec{v}}{\partial z}v_z\Delta t + \frac{\partial\vec{v}}{\partial t}\end{aligned} \tag{B.1}$$

The difference of this velocities divided by the time interval Δt gives the total time rate of change (local and convective) of the particles velocity:

$$\frac{\Delta\vec{v}}{\Delta t} = \frac{D\vec{v}}{Dt} = \frac{\partial\vec{v}}{\partial x}v_x + \frac{\partial\vec{v}}{\partial y}v_y + \frac{\partial\vec{v}}{\partial z}v_z + \frac{\partial\vec{v}}{\partial t} = \frac{\partial\vec{v}}{\partial t} + (\vec{v}\cdot\nabla)\vec{v} \tag{B.2}$$

which is also known as the "substantial derivative" of a moving fluid particle. The convective term is nonlinear in $\vec{v}$, where $\nabla\vec{v}$ is a second-order tensor $(u = v_x, v = v_y, w = v_z)$:

$$\nabla\vec{v} = \begin{pmatrix} \frac{\partial u}{\partial x} & \frac{\partial u}{\partial y} & \frac{\partial u}{\partial z} \\ \frac{\partial v}{\partial x} & \frac{\partial v}{\partial y} & \frac{\partial v}{\partial z} \\ \frac{\partial w}{\partial x} & \frac{\partial w}{\partial y} & \frac{\partial w}{\partial z} \end{pmatrix} \tag{B.3}$$

The RIGHT SIDE of Newtons equation of motion is determined by the sum of forces acting on the moving fluid particle. In particular this forces are:

- *Pressure force:* Pressure forces are acting on all surfaces of a fluid element. In Hydrostatics, these forces balance out exactly and leave the element in a resting position. In Hydrodynamics, acceleration of a fluid element is obtained by a nonzero pressure gradient between two points in space. These pressure forces must balance the forces due to friction for a uniform movement with constant velocity. They would lead to an acceleration only if they exceed frictional forces. If a (infinitely) small peace of fluid in

a streaming liquid is virtually taken out to draw all acting stresses on it´s surface, one can see (for example in x- direction) that there is a small difference in pressure (normal stress) between the left surface and the right surface, which in good approximation can be described by a taylor expansion in x- direction. This pressure difference between the surfaces accounts for the translational acceleration of the fluid particle in x- direction. The equilibrium condition of forces acting on the fluid element in three dimensional space leads to:

$$f_{p_x} = -p\Delta y\Delta z - \frac{\partial p}{\partial x}\Delta x\Delta y\Delta z - \ldots \; + p\Delta y\Delta z = -\frac{\partial p}{\partial x}\Delta x\Delta y\Delta z \tag{B.4}$$

$$f_{p_y} = -p\Delta y\Delta z - \frac{\partial p}{\partial x}\Delta x\Delta y\Delta z - \ldots \; + p\Delta y\Delta z = -\frac{\partial p}{\partial x}\Delta x\Delta y\Delta z \tag{B.5}$$

$$f_{p_z} = -p\Delta y\Delta z - \frac{\partial p}{\partial x}\Delta x\Delta y\Delta z - \ldots \; + p\Delta y\Delta z = -\frac{\partial p}{\partial x}\Delta x\Delta y\Delta z \tag{B.6}$$

Divided by the Volume of the fluid element $\Delta V = \Delta x\Delta y\Delta z$, a subsequent $lim_{\Delta V \to 0}$ gives the net pressure force acting on the fluid element in three dimensions. A vector notation yields:

$$\vec{f_p} = \begin{pmatrix} \frac{-\partial p}{\partial x} \\ \frac{-\partial p}{\partial y} \\ \frac{-\partial p}{\partial z} \end{pmatrix} = -\nabla p \tag{B.7}$$

- *Gravitational forces:* The gravitational field of the earth is a potential field ϕ which accounts for a body force $\vec{f_g} = -\rho\nabla\phi$.

- *Forces due to friction:* In a fluid, such shearing forces (acting tangential on a surface) are resulting from a experimentally checked phenomenon called 'viscosity' of a fluid. Viscous forces are coming from the interaction between fluid molecules (attracting and repelling forces, forces due to collisions of the molecules,...). Macroscopically speaking, this is nothing but friction between two neighboring fluid layers. Fluid flows. It gives way, even when the acting shear stress on it is very small. Although there can be shearing forces as long one pushes at the fluid. The shear stress (e.g. in the x-y-plane) is proportional to the rate of change of shear strain:

$$S_{xy} = \eta(\frac{\partial v_y}{\partial x} + \frac{\partial v_x}{\partial y}) \tag{B.8}$$

η is called the first coefficient of viscosity (unit). In a situation of two parallel plates with water in between, where one of them is kept stationary while pulling on the other one, the force per area which is required to pull the plate is proportional to the ratio of velocity and distance between the two plates. Another observation within this experiment is, that the velocity of the fluid in between the plates tends to go to zero at the surface of the plates. This phenomenon can also be seen on airplane wings, where dust won´t be blown off, even when the plane flies with it´s maximum speed. The condition of fluid movement at the wall boundary is therefore stated as 'no slip

condition'. In the general case of three dimensional (i=x,y,z;j=x,y,z), compressible flow, equation B.8 becomes:

$$S_{ij} = \eta(\frac{\partial v_i}{\partial x_j} + \frac{\partial v_j}{\partial x_i}) + \eta' \delta_{ij}(\nabla \cdot \vec{v}) \tag{B.9}$$

with η' as the second coefficient of viscosity, which appears only in compressible flow. δ_{ij} is the Kronecker delta (1 if i=j and 0 if $i \neq j$). The viscous force per unit volume $f_v\vec{i}sc$ on a small cubic volume element is the resultant of forces on it´s six surfaces. Using index notation and Einstein´s convention of sums (the sum is always taken over double occuring indices), the viscous force reads:

$$\begin{aligned}\frac{\partial S_{ij}}{\partial x_j} =& \frac{\partial}{\partial x_j}\{\eta(\frac{\partial v_i}{\partial x_j} + \frac{\partial v_j}{\partial x_i})\} + \frac{\partial}{\partial x_j}\{\eta' \delta_{ij}\}\frac{\partial v_k}{\partial x_k} \\ =& \eta(\frac{\partial^2 v_i}{\partial x_j^2} + \frac{\partial^2 v_j}{\partial x_i \partial x_j}) + \eta' \frac{\partial^2 v_k}{\partial x_i \partial x_k} \\ =& \eta\{\Delta\vec{v} + \nabla(\nabla \cdot \vec{v})\} + \eta' \nabla(\nabla \cdot \vec{v}) = \eta \Delta \vec{v}\end{aligned} \tag{B.10}$$

The penultimate reshaping of B.10 is only possible, if η and η' are indipendent of the spatial coordinates (as it is in Newtonian fluids). The last reshaping uses de definition of incompressible flow, where $\nabla \cdot \vec{v}$ (the divergence of the velocity field) is zero throughout the fluid.

Applying B.2 (acceleration of the fluid) to the left side and Equations B.7, B.10 and the force due to gravitation ($\vec{f_g} = -\rho \nabla \phi$) to the right side (sum of forces acting on the fluid) of Newton´s equation of motion, we finally arrive at the linear momentum equation for three dimensional incompressible fluid flow in the special case of newtonian fluids in the cartesian frame of reference:

$$\begin{aligned}\rho(\frac{\partial \vec{v}}{\partial t} &+ (\vec{v} \cdot \nabla)\vec{v}) \\ &= -\nabla p - \rho \nabla \phi + \eta \Delta \vec{v} + (\eta + \eta')\nabla(\nabla \cdot \vec{v}) \\ &= -\nabla p - \rho \nabla \phi + \eta \Delta \vec{v}\end{aligned} \tag{B.11}$$

Together with equation 2.2 (Continuity equation for incompressible fluid flow), equation B.11 (Navier Stokes Equations) determine every thinkable macroscopic motion of a fluid in time and space. For reasons which will be discussed later, the gravitational force drops out from equation B.11 from now on. Since they are vector equations (a set of three plus one equations in a three dimensional space), it is very useful to write them down in vector-element notation, substituting $u = v_x, v = v_y, w = v_z$ (the convective term can be rewritten by performing a matrix multiplication):

$$\frac{\partial u}{\partial x} + \frac{\partial v}{\partial y} + \frac{\partial w}{\partial z} = 0 \tag{B.12}$$

$$\rho(\frac{\partial u}{\partial t} + u\frac{\partial u}{\partial x} + v\frac{\partial u}{\partial y} + w\frac{\partial u}{\partial z}) = -\frac{\partial p}{\partial x} + \eta(\frac{\partial^2 u}{\partial x^2} + \frac{\partial^2 u}{\partial y^2} + \frac{\partial^2 u}{\partial z^2}) \tag{B.13}$$

$$\rho(\frac{\partial v}{\partial t} + u\frac{\partial v}{\partial x} + v\frac{\partial v}{\partial y} + w\frac{\partial v}{\partial z}) = -\frac{\partial p}{\partial y} + \eta(\frac{\partial^2 v}{\partial x^2} + \frac{\partial^2 v}{\partial y^2} + \frac{\partial^2 v}{\partial z^2}) \tag{B.14}$$

$$\rho(\frac{\partial w}{\partial t} + u\frac{\partial w}{\partial x} + v\frac{\partial w}{\partial y} + w\frac{\partial w}{\partial z}) = -\frac{\partial p}{\partial z} + \eta(\frac{\partial^2 w}{\partial x^2} + \frac{\partial^2 w}{\partial y^2} + \frac{\partial^2 w}{\partial z^2}) \tag{B.15}$$

C. Special Flow Regimes

C.0.1. Steady Flow

If $\frac{\partial \vec{v}}{\partial t} = 0$ in the Navier Stokes equations, the flow field keeps uniform in time. Streamlines (Analog to the electrical field- lines in Electrodynamics; field lines of the flow are always tangential to the velocity field) are equal to the particle tracks $\vec{r}$ (the track observed by following a defined fluid particle on it´s way through the flow field). Consider a car driving along a road. Whether the road goes up and down, left or right, the car´s driving path (= particle track) will always coincide with it´s predefined road (= streamline). The car will have to go up a hill, where it get´s slower (convective acceleration) and will go downhill, where it get´s faster (convective decceleration), but the driving path of the car will always be the same as the leading road.

C.0.2. Unsteady Flow

If $\frac{\partial \vec{v}}{\partial t}$ is not equal to zero, the streamline will no longer be equal to the particle track. Changes of the velocity field with respect to time will lead to new phenomenas of the flow (e.g. pressure gradient changes). Now the car driving the same road in the morning. In the afternoon, some road men are quick at work and change the direction of the road (= velocity field) in some way. Next morning, the driver of the car (= the fluid particle) will be surprised, that he has to go another direction.

C.0.3. Laminar Flow

Streamlines don´t mix up, that means, they don´t cross each other. The flow profile is characterized as a parabola. The nonlinear term in the equations of fluid motion (Navier Stokes equations) is negligible small. Such a flow field always occures, if the viscous forces are big due to the acceleration forces. Most likely, perfect laminar flow occures in fluid motion between two parallel plates or in a long, uniform tube of cylindrical diameter. If two plates are positioned and all nonlinear and nonsteady terms are neglected and a pressure gradient is acting only in z- direction, the following equation determines the flow field in the x-z- Plane (cartesian coordinates):

$$\frac{\partial p}{\partial z} = -\eta \frac{\partial^2 w}{\partial x^2} \tag{C.1}$$

It leads to

$$w = w_{(x)} = -\frac{x^2}{2\eta}\frac{dp}{dz} + c_1 x + c_2 \tag{C.2}$$

by double integration over x. Constitution of the prevalent boundary conditions determines c_1 and c_2 (integration constants) in this 2D- Problem:

- The flow is symmetric:

$$\frac{\partial u}{\partial x}|_{x=0} = 0 \rightarrow \ c_1 = 0 \tag{C.3}$$

- No slip on the wall of the plates:

$$u_{(x=d)} = u_{(x=-d)} = 0 \ \rightarrow \ c_2 = \frac{d^2}{2\eta}\frac{dp}{dz} \tag{C.4}$$

The analytical term of the (perfectly laminar) velocity field between two parallel plates can now be written down as:

$$w_{(x)} = \frac{(d^2 - x^2)}{2\eta}\frac{dp}{dz} \tag{C.5}$$

Therefore, for constant viscosity, the velocity field is determined by the distance between the two plates and the pressure gradient in z- direction.

C.0.4. Inviscid Steady Flow

In this purely mathematical flow behavior (fluids are always viscous in nature), $\eta = 0$. If fluid enters the room between the two plates described above with a velocity component only in z- direction (w), no changes of velocity in x or y- direction will occur, simply by applying Newton´s second law of motion (no forces, no acceleration $\rightarrow$ no change of direction) on this special case of fluid flow. Here, the nonlinear terms of the Navier Stokes equations get important to describe the fluid flow in a correct way. Since turbulence is a phenomenon only taking place in viscous fluids, the nonlinear term makes no mathematical problems. Projecting the problem onto the x-z- direction (pressure gradient only in z- direction), the equations of motion turn out to be:

$$-\frac{\partial p}{\partial z} = \rho w \frac{\partial w}{\partial z} \tag{C.6}$$

In absence of viscous forces between the fluid laminae and the contact region of fluid with the wall, the flat entrance velocity profile remains flat between the two parallel plates. The right term of equation C.6 can be rewritten by using the product rule of differentiation:

$$w\frac{\partial w}{\partial z} = \frac{\partial}{\partial z}(w^2) - \frac{\partial w}{\partial z}w \ \rightarrow 2w\frac{\partial w}{\partial z} = \frac{\partial}{\partial z}(w^2) \ \rightarrow w\frac{\partial w}{\partial z} = \frac{1}{2}\frac{\partial}{\partial z}(w^2) \tag{C.7}$$

Integration yields the analytic expression of the velocity field in implicit form:

$$\frac{1}{2}\rho w^2 + p = const. = p_0 \tag{C.8}$$

which is well known as 'law of Bernoulli'. Together with the continuity equation (also known as 'Leonardos law' in one-dimensional flow: crossectional area times the streamline velocity in

place A equals crossectional area times the streamline velocity in place B), this law governs inviscid, steady fluid motion. It is valid throughout the whole fluid domain, but must be applied onto one particular streamline ranging from a location A to a location B, if the flow field and the pressure field A and B is not uniform over the crossection at location $z = z_A$ and $z = z_B$. The first term of Bernoullies law denotes the dynamic pressure of a moving fluid (density of kinetic energy), the second term is called static pressure of the fluid. Equation C.8 is a conservation equation. p_0 keeps constant on a streamline while the fluid particles move through time and space. In a closed system (no fluid dissapears), total pressure will always be constant. Therefore, if fluid flows from a place A to a place B with a narrower crossection than A (where the fluid must flow faster due to Leonardos law of conservation of mass $\rightarrow$ higher dynamic pressure in B), static pressure tends to drop down. If equation C.8 is formulated for a streamline which extends from A to B:

$$\frac{1}{2}\rho w_1^2 + p_1 = \frac{1}{2}\rho w_2^2 + p_2 \tag{C.9}$$

the pressure difference $\Delta p = p_2 - p_1$ (applying Leonardo's law on the crossections depicted in figure (?) with areas F_A and F_B: $v_A F_A = v_B F_B$) yields:

$$\Delta p = \frac{1}{2}\rho w_1^2 (1 - \frac{F_A^2}{F_B^2}) \tag{C.10}$$

If $F_A = F_B$, it becomes clear, that in this case no pressure gradient is needed for inviscid fluid motion. In other words, no pressure gradient establishes between A and B. If F_A is bigger than F_B, the fluid runs through a convective acceleration, which leads to a lowering of static fluid pressure.

C.0.5. Inviscid Unsteady Flow

The governing equation in the special case of flow between two plates in the z-x- plane (pressure gradient only in z- direction, entrance velocity in z- direction) reads:

$$-\frac{\partial p}{\partial z} = \rho\frac{\partial w}{\partial t} + \rho w\frac{\partial w}{\partial z} \tag{C.11}$$

The pressure gradient get´s higher, when acceleration of the fluid is higher. If $F_A = F_B$, the velocity w won´t change along the z- direction (w is not dependent on z). Therefore, the last term in equation C.11 drops out. Since the velocity is uniform throughout one particular crossection, a z- integration of the equation left behind with boarders z_A and z_B gives:

$$\rho\int_{z_A}^{z_B}\frac{\partial w}{\partial t} = \rho(z_B - z_A)\frac{\partial w_A}{\partial t} = p_A - p_B \tag{C.12}$$

That means, a large acceleration gives a large negative pressure gradient (or vice versa) from A to B. If a velocity gradient is present between A and B (e.g. in case of a narrower crossection in B rather than in A), the nonlinear term in equation C.11 must be taken into

account. Changing it in the same manner as in the discussion of inviscid steady flow (product rule of differentiation), the governing equation of flow finally looks like:

$$\rho\frac{\partial w}{\partial t} = -\frac{\partial p}{\partial z} - \rho\frac{1}{2}\frac{\partial}{\partial z}(w^2) = -\frac{\partial}{\partial z}(\rho\frac{1}{2}w^2 + p) \tag{C.13}$$

D. Dimensional Analysis: Determining Flow Behavior

A correct mathematical model of a certain fluid motion always connects and combines all relevant influencing variables of the problem in a way, that the solution is 'dimensionally correct' (the physical dimensions on the right side must be equal the dimensions on the left side of the governing equations). By the help of the so called 'Pi- Theorem' it is possible, to distinguish between possible (dimensionally correct) and impossible (dimensionally incorrect) combinations of the influencing variables governing a physical problem (e.g. fluid flow). This is even possible, when the correct formulation of the physical problem is not by hand and only the influencing variables are known. A physical variable consists of a value (e.g. {X}=32), a unit ([X]=kg) and a dimension (X)=M (mass). The Pi- Theorem uses basis dimensions like the length L, the time T, the mass M and derived dimensions like the velocity V, the density which are potential products of basis dimensions. Definition of the Pi- Theorem: Given a implicit functional relation of n influencing variables a_i (i=1,2,3,...,n) with m basis dimensions:

$$f(a_1, a_2, \cdots, a_n) = 0 \tag{D.1}$$

This problem has the solution:

$$F(\Pi_1, \Pi_2, \cdots, \Pi_{n-m}) = 0 \tag{D.2}$$

if f is the only functional relation between the influencing variables and if f is independent of the units, in which the influencing variables are measured. Π_i are dimensionless products of the influencing parameters. These products (e.g. the Reynolds number in steady fluid flow through a uniform pipe) define flow behavior, for example if a certain flow tends to be laminar or turbulent. Because of the absence of dimensionality, there is no noticeable difference in flow behavior, no matter how big the influencing parameters within a dimensionless parameter are, as long as the governing dimensionless parameter retains a fixed value. Without the explicit mathematical formulation of the physical problem, the Pi- Theorem only gives back the minimal set of dimensionless parameters describing the problem. It cannot determine the explicit form of the parameters. If a problem is governed by 5 influencing variables consisting of 3 basic dimensions, m-n=5-3=2 dimensionless parameters have to be found for solving a problem. An Example: If a physical flow problem is fully determined by 5 variables (e.g. flow in a straight tube of diameter D), the implicit functional formulation reads: $f(\tau_w, D, u, \rho, \eta) = 0$, where τ_w is the wall shear stress, u the velocity, ρ the density of the fluid and η the first coefficient of viscosity. Here, n=5 and and m=3 (length L, time T and mass M), therefore 2 dimensionless parameters Π_1 and Π_2 describe the problem. If

nothing is known about the determining equations of the problem, one can 'try' to find a solution by combining the variables of influence:

$$\Pi_1 = \frac{\tau_w}{\rho u^2},\ \Pi_2 = \frac{\rho u D}{\eta} \tag{D.3}$$

In this example, a problem with an implicit function f of 5 variables at the beginning was transformed into a reduced problem with an implicit function F of 2 parameters. To solve such a problem, one must only find the functional connection F between Π_1 and Π_2. Π_1 factorized by 8 is called 'tube friction coefficient' λ_R, Π_2 is named after Osborne Reynolds and called 'Reynolds number' Re. As a result, $F(\lambda_R, Re) = 0$, or $\lambda_R = \lambda_R(Re)$. If such a functional connection suffices to correctly outline a physical problem (in this case the full-blown stationary flow in a cylindrical tube) can only be answered by comparison with reality. In reality it turns out, that laminar flow in a tube is fully determined only by one dimensionless parameter, since:

$$\lambda_R = \lambda_R(Re) = \frac{64}{Re} \tag{D.4}$$

On the other hand, for turbulent pipe flow, two parameters and their functional connection only suffice for the special case of smooth pipe walls. Experimentally checked, the roughness of the wall plays an important role in turbulent flow. If the roughness exceeds a certain limit, the solutions for pipe flow won´t lie on a common curve $\lambda_R(Re)$. Therefore, the roughness constant of the pipe wall must be added to the variables of influence of the physical model $f = 0$ (which results in a new set of n-m=6-3=3 dimensionless parameters). If now a physical phenomenon can be determined by a set of governing equations of motion (as it is the case in fluid flow), the transformation of these equations into a dimensionless form happens by consequently perform the following steps:

1. Search for variables of influence in the governing equations of motion. Such variables usually are problem relevant quantities like the diameter of the tube, or the inlet velocity. The numerical value of the dimensionless parameters built up from a suitable set of these reverence quantities represents the meaning of the terms containing the parameters (e.g. the convectional term or the local acceleration term). In case of the Navier Stokes Equations, these quantities are: $t;\ x,\ y,\ z;\ u,\ v,\ w;\ p;\ \rho;\ \eta$.

2. Make all variables of the governing equations dimensionless (define relations between the variables of influence, the reverence values of the physical problem and dimensionless variables signed by a tilde, $r \ldots$ reverence):

$$t = \tilde{t}\frac{L}{U};\ x = \tilde{x}L,\ y = \tilde{y}L,\ z = \tilde{z}L;\ u = \tilde{u}U,\ v = \tilde{v}U,\ w = \tilde{w}U \tag{D.5}$$

$$p = \tilde{p}p_r;\ \rho = \tilde{\rho}\rho_r;\ \eta = \tilde{\eta}\eta_r \tag{D.6}$$

3. Plug in these new dimensionless variables into the equations (substitute the variables of influence by the above defined relations) and search for dimensionless products. The nondimensionalization of the linear momentum equation gives (without proof):

$$Sr\rho\frac{\partial \vec{v}}{\partial t} + \rho(\vec{v}\cdot\nabla)\vec{v} = -Eu\nabla p + \frac{1}{Re}\eta\Delta\vec{v} \tag{D.7}$$

with the following dimensionless products:

- The *Strouhal- number* is a measure for the transient (time- dependent) behaviour of fluid motion:

$$Sr \equiv \frac{\tilde{L}}{\tilde{U}\tilde{T}} \tag{D.8}$$

  A quasi- stationary fluid motion is characterized by Sr$\ll$1. Stationary boundary conditions are a essential but not sufficient criterion for a stationary motion, since fluid flow can get unstable as a consequence of turbulence (inherent non-stationary fluid motion). With Sr$\approx$1, the motion is non- stationary (transient).

- The *Euler- number*:

$$Eu \equiv \frac{\tilde{p_r}}{\tilde{\rho_r}\tilde{U^2}} \tag{D.9}$$

  get´s important in fluid motion, where forces due to pressure and acceleration are dominant.

- The *Reynolds number*:

$$Re \equiv \frac{\tilde{U}\tilde{L}\tilde{\rho_r}}{\tilde{\eta_r}} \tag{D.10}$$

  The Reynolds- number is a measure for the ratio between inertial forces and friction forces. If Re$\ll$1, the flow regime is called 'creeping flow', where the convective terms (nonlinear terms) of the Navier Stokes Equations can be linearized. If Re$\approx$1, the complete set of the Navier Stokes equations must be solved. Inertial forces, pressure forces and forces due to friction (viscosity) are of the same order of magnitude. For solutions of the governing equations of fluid motion in the limit of high Reynolds numbers (Re$\gg$1), the boundary layer theory suffices (Aerodynamics). If the Reynolds number exceeds a certain limit, denoted as the critical Reynoldsnumber Re_c, fluid motion skips from laminar to turbulent (chaotic) flow.

Flow regimes of quasi- stationary flows thus can be characterized by the term 'laminar' if the laminae of the fluid don´t cross each other and by 'turbulent' if the laminae cross each other and the fluid behaves in a chaotic, (mathematically) nonlinear way. Between this two flow-phases, flow is said to be 'transitional' or 'disturbed', meaning, that flow is neither perfectly laminar nor perfectly turbulent.

E. Structural Analysis in Aortic Flows

E.1. Foundations of Elasticity Theory

Per definition, stress equals force per unit area. A three dimensional infinitesimal small body like a dice or a small volume cut out of a cylindrical tube (e.g.: blood vessel) can be loaded with stresses on each surface. Conveniently, stress on a surface is an unidirectional vector consisting of three components in three dimensional space, which can be separated into a tangential (t) component (shear stress):

$$\tau = \lim_{\Delta A \to 0} \frac{\Delta \vec{F}_t}{\Delta \vec{A}} \tag{E.1}$$

and a normal (n) component (normal stress, pressure):

$$\sigma = \lim_{\Delta A \to 0} \frac{\Delta \vec{F}_n}{\Delta \vec{A}} \tag{E.2}$$

According to the three dimensional space, three stress vectors

$$t^{(\vec{n})} = \lim_{\Delta A \to 0} \frac{\Delta \vec{F}}{\Delta \vec{A}} \tag{E.3}$$

define the entire stress state of the body (index n denotes the orientation of the surface element $\Delta \vec{A}$ on which the force $\Delta \vec{F}$ is acting). All nine components of this three vectors form the Cauchy Stress Tensor, which is a tensor of second order. The kinetic relations (governing equations of motion) for a deformable solid body can be obtained by applying Newtons law of motion (fundamental law of dynamics) onto a infinitesimal volume element [23]. Therein, the resultant of all forces acting on the element (only surface forces, since body forces like gravity are neglected in this study) which are responsible for the inertial forces the element comprises is defined by the gradient of Cauchy´s stress tensor. If the body is forced to maintain a fixed position by certain outer constraints (e.g.: fixations due to surroundings), the kinetic relations merge into a set of equilibrium conditions. Kinetic relations formulated in a cylindrical frame of reference can be found in [23,25]. Deformation is usually described in terms of strain, the ratio of change in a given dimension to its original value in the unstressed state [22]. Normally, kinematic deformations are calculated by means of two different geometrical relations, namely Green´s strain tensor (E_{ij}) and Almansi´s strain tensor (e_{ij}). A measure for the deformation of a body is the change of an infinitesimal small distance

between two certain points within the body before stressing it (reference configuration X_i, infinitesimal distance dX_i) and after applying stress on it (instantaneous configuration x_i, infinitesimal distance dx_i). Both tensors measure deformation as the difference between the square of the distance between the two points in reference and instantaneous configuration ($ds^2 - dS^2$). Almansi´s strain tensor measures deformation with respect to Eulers coordinates (instantaneous, deformed configuration), whereas Green´s strain tensor is defined and derived by Lagrange coordinates (deformation in reference configuration). Strain tensors in both formulations and their linearized counterparts (only valid, if all derivatives of displacement small against one) in a cylindrical coordinate frame can be found [23,25]. The Stress tensor in Cauchy´s formulation is defined upon surfaces of the volume element in the instantaneous configuration using Euler´s coordinates [23]. If for example the original circumference ($C = 2\pi R$) of the tube at zero stress state (reference configuration) is denoted by C_{rc} and after imposition of stress is denoted as C_{ic}, principal stretch ratios can be defined between stretched radius and unstretched radius of the tube:

$$\lambda_\theta = \frac{C_{ic}}{C_{rc}} \tag{E.4}$$

which link circumferential (or radial and longitudinal) Cauchy stresses σ, Lagrange-Piola stresses T and Kirchhoff stresses S in the following way:

$$S_\theta = \frac{1}{\lambda_\theta} T_\theta = \frac{\rho_{rc}}{\rho_{ic}} \frac{1}{\lambda_\theta^2} \sigma_\theta \tag{E.5}$$

with ρ_{ic} and ρ_{rc} beeing the density of initial and reference configuration. According to the assumed incompressibility of the aortic wall, the ratio between these densities per definition remains exactly 1. Principal circumferential (or radial and longitudinal) Green strains are defined as:

$$E_\theta = \frac{1}{2}(\lambda_\theta^2 - 1) \tag{E.6}$$

whereas principal circumferential (or radial and longitudinal) Almansi strains are calculated by:

$$e_\theta = \frac{1}{2}(1 - \frac{1}{\lambda_\theta^2}) \tag{E.7}$$

Experimental data is variantly presented either in Euler-Green-Cauchy- formulation or in Lagrange-Almansi-Piola-Kirchhoff- formulation. All 6 kinematic relations and the 3 kinetic equations oppose 15 unknown physical quantities. The lack of six equations to be capable of fullfilling the equivalence of unknowns and equations (closing of the equation system) is eliminated by constitutive relations. Constitutive relations account for special material properties and express, that deformations of a body uniquely depend on instantaneous stresses. They can either be formulated in Lagrange coordinates ($E_{ij} = F(S_{kl})$) or in Euler coordinates ($e_{ij} = G(\sigma_{kl})$), in both cases depending on theoretically, experimentally and empirically found material laws. A special case of such a relation, formulated for small displacements and derivatives of displacement, can be written as:

$$e_{ij} = D_{ijkl}\sigma_{kl} \tag{E.8}$$

where D_{ijkl} - the tensor of elastic constants - can on one hand consist of stress dependent components where the material responses on stresses are non-linear and on the other hand consist of constant components in the special case of a linear elastic stress response. The latter case, known as generalized Hooke´s law ($\sigma_{ij} = D^{-1}_{ijkl} e_{kl}$), was used to calculate the approximate stress-strain- relationship caused by fluid-structure- interaction in the actual aortic flow model. Hooke´s law in a cylindrical reference frame can be found in [23,25]. Elasticity is the ability of a material to return to its original shape and dimension after deformation [23]. If a body is stretched beyond a certain limit, a permanent elongation is produced. If a body is called isotropic and homogenous, the elastic properties are independent of the directions and locations in which a stress is applied.

E.2. Strategy of Durability Approval in Aortic Flow Models

Blood vessels consist of several different tissues, either physiological active (smooth muscle) or passive (endothelial cells, connective tissue, bands of elastin and fibers of collagen) in their mechanical behavior. Both types consist of bioviscoelastic solids like actin, elastin, collagen, ground substance in various ratios and amounts, repsonsible for their complicated non-linear elastic behavior. Besides their nonlinear stress-strain relationship, blood vessels are mechanically characterized by the existence of hysteresis, a creep under constant stress, a relax under a constant strain, non-homogenousity and anisotropic mechanical behaviour with respect to spatial coordinates [22]. Arteries are said to be incompressible with a poission ratio of $\mu = 0.5$ [22]. Focusing only on the pure mechanical behavior, kinematic, kinetic and constitutive relations are sufficient to determine all components of displacement, deformation and stresses of an elastic body [24].

According to it´s geometrical shape, the human ascending aorta can be approximately seen as a thick-walled circular 90-degree- bend [22,23]. To obtain the approximate stress-state at the outer portion of the ascending aortic wall, where most frequently aortic dissections are located, solutions of equations gained from linearized elasticity theory are used. To account for nonlinear elastic behavior of the aortic wall under internal load, the linear solutions (stress equals strain times a constant modulus of elasticity, generalized Hooke´s law) are successfully splitted into stepwise incremental solutions with stress-dependent moduli of elasticity (Young´s modulus). The thick-wall approach is prefered in the case of aortic walls, since the ratio between wall thickness and radius of the tube should not exceed 0.1 in the thin wall theory, which is but the case in aortic walls [22]. Wall shear stress (WSS) - though an important factor in cell-scale mechanics and physiology/pathology (endothelial cell remodeling,...) [21,22,25,45] - is neglected in structural analysis, since the stress values of normal stress (transmural static and dynamic pressure) acting on the vessels wall are approximately 2 (according to the values obtained in the simulation) to 4 [22] magnitudes higher than WSS. A healthy artery is observed to be not stress free in a load free (without applying internal pressure) configuration, since an arterial ring springs open when cut in radial direction (non zero residual stress). This circumstance alters the circumferential stress

distribution in a way, that the negative slope of σ_c between inner and outer aortic radius decreases (σ_c at the intima decreases, while σ_c at the adventicia slightly increases). Arterial residual stress is neglected in the ongoing discussion.

Three of the originally six kinematic relations suffice to describe the rotationally symmetric case of a closed cylindrical tube loaded with uniform internal pressure [23]:

$$E_r = \frac{\partial u}{\partial r}, E_\theta = \frac{u}{r}, E_z = \frac{\partial w}{\partial z} \tag{E.9}$$

with u denoting the displacement in radial and w the displacement in axial direction, respectively. The generalized Hooke´s law for stress and strain principle axes (shear-stress- free axes) in a cylindrical coordinate frame serves as a link between stresses and strains:

$$\sigma_r = \frac{Y_r(1-\mu))}{(1+\mu)(1-2\mu)}[E_r + \frac{\mu}{1-\mu}(E_\theta + E_z)] \tag{E.10}$$

$$\sigma_\theta = \frac{Y_r(1-\mu))}{(1+\mu)(1-2\mu)}[E_\theta + \frac{\mu}{1-\mu}(E_z + {}_r)] \tag{E.11}$$

$$\sigma_z = \frac{Y_z(1-\mu))}{(1+\mu)(1-2\mu)}[E_z + \frac{\mu}{1-\mu}(E_r + E_\theta)] \tag{E.12}$$

with Y_r, Y_z denoting Youngs modulus (modulus of elasticity) in radial and axial direction, accounting for the anisotropy of arterial structures. [22] reports, that incremental elastic moduli of the thoracic aorta in live dogs are $5 \cdot 10^6$ dyn/cm^2 = 50 MPa for the radial axis, $7 \cdot 10^6$ dyn/cm^2 = 70 MPa for the radial axis, $10 \cdot 10^6$ dyn/cm^2 = 100 MPa for the radial axis, implying a ratio of $Y_r/Y_\theta/Y_z = 1/1.4/2$. Ex vivo measurements of stress-strain behavior in several aortic tissue [27,28,63] of middle-aged patients ($\approx$ 30-50 years) reveal stress-dependent radial Young´s moduli of Y_r = 0.2 MPa (from 0 to 8000 Pa transmural blood pressure), Y_r = 0.5 MPa (8133 Pa - 10600 Pa), Y_r = 0.7 MPa (10800 Pa - 13332 Pa), Y_r = 1 MPa (13465 Pa - 16265 Pa), Y_r = 1.5 MPa (16400 Pa - 18664 Pa), Y_r = 2.5 MPa (18800 Pa - 21331 Pa), Y_r = 10 MPa (21464 Pa - 27730 Pa) and Y_r = 500 MPa (27864 Pa - 52000 Pa) which are used in all further stress and strain analysis (although Young´s moduli can vary in a wide range, depending on age and intrinsic factors of the tissue). It has been found out, that the arterial wall is cylindrically orthotropic (elastic symmetry in the planes perpendicular to the r, θ, z axes), which means, that a good approximation of wall behavior can be obtained by measuring only the radial and longitudinal strains [22]. It should be noted, that a subdivision into two independent Youngs moduli determining elasticity of each principle axis is only an approximation, since a rigorous treatment of anisotropy in arteries leads to a more complex geometric situation. Theory and modelling strategies of anisotropy in arteries can be found in [25]. For the sake of simplicity, longitudinal Young´s modulus is (heeding the ratio of $Y_r/Y_\theta/Y_z = 1/1.4/2$) substituted twice as high as radial modulus in the stress-strain-equations. Above defined kinematic relations plus Hooke´s law and the equilibrium conditions for rotational symmetry:

$$\frac{\partial \sigma_r}{\partial r} + \frac{\sigma_r - \sigma_\theta}{r} = 0 \tag{E.13}$$

$$\frac{\partial \sigma_z}{\partial z} = 0 \tag{E.14}$$

together with the following boundary conditions at $r = r_a$:

$$\sigma_r = -p_a = 0 \tag{E.15}$$

at $r = r_i$:

$$\sigma_r = -p_i \tag{E.16}$$

and at $z = \pm\frac{h}{2}$:

$$\sigma_z = \sigma_0 = \frac{p_i r_i^2}{(r_a^2 - r_i^2)} \tag{E.17}$$

lead to relations for the displacements u and w:

$$u = \frac{r}{Y_r}\left\{\frac{\left[(1-\mu) + (1+\mu)\left(\frac{r_a}{r}\right)^2\right] p_i}{\left(\frac{r_a}{r_i}\right)^2 - 1} + \mu\sigma_0\right\} \tag{E.18}$$

and

$$w = -\frac{z}{Y_z}\left[2\mu\frac{p_i}{\left(\frac{r_a}{r_i}\right)^2 - 1} + \sigma_0\right] \tag{E.19}$$

The resulting stresses can be derived by:

$$\sigma_r = -\frac{p_i\left[\left(\frac{r_a}{r}\right)^2 - 1\right]}{\left(\frac{r_a}{r_i}\right)^2 - 1}, \tag{E.20}$$

$$\sigma_\theta = \frac{p_i\left[\left(\frac{r_a}{r}\right)^2 + 1\right]}{\left(\frac{r_a}{r_i}\right)^2 - 1}, \tag{E.21}$$

and

$$\sigma_z = \sigma_0 = \frac{p_i r_i^2}{(r_a^2 - r_i^2)} \tag{E.22}$$

since σ_z is a constant throughout the entire length of the tube. The strains are then easily obtained by substituting the above derived displacements u and w into equation E.9:

$$E_r = \frac{1}{Y_r}\left\{\frac{\left[(1-\mu) - (1+\mu)\left(\frac{r_a}{r}\right)^2\right] p_i}{\left(\frac{r_a}{r_i}\right)^2 - 1} - \mu\sigma_0\right\} \tag{E.23}$$

$$E_\theta = \frac{1}{Y_r}\left\{\frac{\left[(1-\mu) + (1+\mu)\left(\frac{r_a}{r}\right)^2\right] p_i}{\left(\frac{r_a}{r_i}\right)^2 - 1} - \mu\sigma_0\right\} \tag{E.24}$$

$$E_z = -\frac{1}{Y_z}\left[2\mu\frac{p_i}{\left(\frac{r_a}{r_i}\right)^2 - 1} - \sigma_0\right] \tag{E.25}$$

If the tube is curved, stress at the inner radius is higher than the stress at the outer radius of the curvature. Considering a thin-walled curved tube under uniform internal pressure, the value of σ_z matches the value in the straight tube, while σ_r and σ_θ are given as:

$$\sigma_\theta = \frac{p_i r_i \left(\frac{R}{2r_i} + 0.25 \sin\theta\right)}{h \left(\frac{R}{2r_i} + 0.5 \sin\theta\right)} \tag{E.26}$$

where R is the radius of the curvature (see Pic...) and h stands for the thickness of the wall. As compared with the stress value at $0°$ and $180°$:

$$\sigma_\theta(0°) = \sigma_\theta(180°) = \frac{p_i r_i}{h} \tag{E.27}$$

the value at $90°$ (the outer portion of the curve):

$$\sigma_\theta(90°) = \frac{p_i r_i \left(\frac{R}{2r_i} + 0.25\right)}{h \left(\frac{R}{2r_i} + 0.5\right)} \tag{E.28}$$

is approximately 0.875 $\sigma_\theta(0°)$ when R = 0.03 m (approximate radius of the geometric aortic model used for simulations). According to equation E.26, stress at the inner portion of the curvature (at $-90°$) is approximately 1.25 $\sigma_\theta(0°)$. [16] states, that stress on the inner curvature of the aortic arch is much larger than on the outer curvature. Therefore, to maintain the constant state of stress between outer and inner curvature, the artery would be expected to have a larger wall thickness on the inner curvature than on the outer curvature (stress is force per unit area). In case of the aortic arch, it has been observed that the wall is much thicker at the bottom of the arch than at the top, leading to a more or less constant stress distribution around the circumference of an aortic cross section. According to that, stresses are calculated for a straight tube with constant wall thickness, keeping in mind, that wall stress is very sensitive to changes in aortic wall thickness (see equation E.21).

The stress-strain- relationship of the physiological blood-pressure- loaded aortic wall is highly non-linear. Therefore, an incremental elastic modulus, determined from observations of relatively small changes of pressure and vessel diameter should be used to detect the non-linear behavior of the material. A non incremental (constant) elastic modulus calculated only once in a single measurement of the increased diameter of the vessel does not account for nonlinearities in the stress-strain- curve which are apparent in blood vessels. Nevertheless, the mechanical behavior of the aortic wall can in some borders approximated by a linear elastic theory. The high distensibility in the low strain region is assumed to be a result from low elastic moduli of smooth muscle and elastin. As the diameter is increased due to an elevation of transmural pressure (stress), more and more collagen fibers (relatively stiff) are engaged, making the vessel less compliant (elevating the elastic modulus) [22]. According to that theory, the components of the vessel wall are arranged in parallel in such a way, that strain is transferred successively from elastin to muscle to collagen as the vessel is distended further and further [22]. The elastic modulus of arterial walls for absolute strains

greater than approximately 1.6 approaches that of collagen, which is itself non-linear in mechanical behavior (Youngs modulus of collagen Y_{col} ranges widely from $30 \cdot 10^6$ dyn/cm^2 (= 300 MPa) - $100 \cdot 10^6$ dyn/cm^2 = (= 1000 MPa) [21,22]) within a certain range of strain. It can be observed, that linearity (and therefore a constant Youngs modulus) is only given in a certain range of stress-strain- ratios. Especially in physiological regions up to a pressure of 120 mmHg and regions with considerably high stress, the curve can be approximated by a linear function $\sigma = Ye + \sigma_i$ with constant Youngs moduli (Y) for each of the two regions. σ_i denotes the initial stress defining the pre-stressed state in instantaneous configuration (Eulers coordinates). The value of (constant) Y_{max} is (for reasons discussed above) approximated by the maximum Youngs modulus of collagen (500 MPa). To obtain an accurate stress-strain-relationship which accounts for aortic nonlinear elastic behavior, distensibility, anisotropy and incompressibility, a incremental calculation procedure was written in commercial Microsoft Excel software. Physically the calculation is based on the mechanism, how the aortic wall responses the continous elevation of blood pressure during the cardiac cycle (pumping action of the heart). Mathematically, this process can be subdivided into finite (incremental) pressure steps ranging from zero internal pressure to the actual (physiologic/pathologic) systolic pressure level (p_{sys} at t = 0.18 s) in rest or exercise. The artery´s load free configuration (reference configuration, inner aortic diameter $r_{irc} = r_i$, wall thickness $h_{rc} = h$, outer aortic diameter $r_{arc} = r_{irc} + h_{rc}$=$r_a$, actual variable radius of interest r_rc=r, actual length of an arterial segment of interest z_{rc}=z, total lenght of the arterial segment l_{rc}, internal pressure p_i = 0 Pa) is defined by:

$$r_{irc} \leq r_rc \leq r_{arc};\ 0 \leq z_{rc} \leq l_{rc} \tag{E.29}$$

whereas the loaded (deformed, instantaneous) configuration ($r_{iic} = r_i$, $h_{ic} = h$, $r_{aic} = r_{irc} + h_{rc} = r_a$, actual variable radius of interest r_rc=r, length of an arterial segment of interest z_{rc}=z, total lenght of the arterial segment l_ic, incremental pressure step Δp_i = 133.32 Pa) is defined as:

$$r_{iic} \leq r_ic \leq r_{aic};\ 0 \leq z_{ic} \leq l_{ic};\ 0 \leq \Delta p_i \leq p_{sys} \tag{E.30}$$

Deformations in cylindrical coordinate frames are described my means of principal stretch ratios (see also section E.1):

$$\lambda_{r_{ic}}(r_{rc}) = \frac{\partial r_{ic}}{\partial r_{rc}} = \frac{r_{rc}}{r_{ic}\lambda_z};\ \lambda_\theta(r_{rc}) = \frac{r_{ic}}{r_{rc}}; \lambda_z = \frac{z_{ic}}{z_{rc}} \tag{E.31}$$

and related to Green strains by:

$$E_i = \frac{1}{2}(\lambda_i^2 - 1), i = r_{ic}, \theta_{ic}, z_{ic} \Rightarrow \lambda_i = \sqrt{1 + 2E_i} \tag{E.32}$$

The assumption of incompressibility of aortic tissue implies, that during the deformation process, the wall volume is preserved. With $r_a = r + h$ and $r_i = r - h$, wall thickness, aortic radius and the ratio $(r_a/r)^2$ (required for stress and strain calculation) in the deformed

configuration can be determined by the aid of following considerations ($V = const. = c$):

$$V = c = (r_a^2 - r_i^2)\pi z = (r^2 + hr + \frac{h^2}{4} - r^2 + hr - \frac{h^2}{4})\pi z = 2\pi hrz \rightarrow$$

$$2\pi h_{ic} r_{ic} z_{ic} = 2\pi h_{rc} r_{rc} z_{rc} \rightarrow \frac{h_{ic}}{h_{rc}} = \frac{r_{rc} z_{rc}}{r_{ic} z_{ic}} \Rightarrow$$

$$h_{ic} = h_{rc} \underset{\theta z}{1}; \; r =_\theta r_{rc}; \; (\frac{r_{aic}}{r_{ic}})^2 = (\frac{r_{ic} + h_{ic}}{r_{ic}})^2 = (1 + \frac{h_{ic}}{r_{ic}})^2 \quad \text{(E.33)}$$

Successfully, h_{ic}, r_{ic} and $(r_a/r)^2$ for an internal pressure of $p_i = 133.32\ Pa$ are calculated by applying the first pressure increment $\Delta p_i = 133.32\ Pa$ (substituting Δp_i instead of p_i) onto the strain equations (E.25) which relate the actual deformed state to the former unloaded aortic state (zero internal pressure). Stress values are determined by substituting the values of h_{ic}, r_{ic} and $(r_a/r)^2$ for an internal pressure of $p_i = 133.32\ Pa$ into equations E.20, E.21 and E.22. This procedure makes sure, that the calculation of actual stress values is always based on instantaneous aortic dimensions, which vary continously with increasing internal pressure (step by step, the aorta extends and wall thickness decreases, which directly affects wall stress). In a proceeding step, h_{ic}, r_{ic} and $(r_a/r)^2$ for 266.66 Pa internal pressure are derived by substituting a second pressure increment $\Delta p_i = 133.32\ Pa$ onto the strain equations, which now relate the former deformed configuration for $p_i = 133.32\ Pa$ to the actual deformed configuration at pressure level 266.66 Pa (E_r, E_θ, E_z consequently are calculated by substituting h_{ic}, r_{ic} and $(r_a/r)^2$ obtained from the last preceding incremental pressure level). This procedure can be carried out iteratively to finally yield aortic radii, wall thickness, absolute stress and strain values for p_{sys} gained from CFD simulations (see proceeding sections).

Since all actual pressure values in the simulation are referenced to the pressure outlet boundary condition ($p_{out}^{static} = 0$ mmHg), a comparable physiologic pressure value (as the values in the experiment are) must be obtained by adding the systolic value (p_s^0) to each simulated pressures at systole (see section 5.2). Unstressed inner ascending aortic radius is set to $r_{irc} = 0.01$ m (to be comparable with the values gained from the simulations), unstressed outer ascending aortic radius was derived from the average measured unstressed (unloaded) ex vivo aortic wall thickness gained from [27,28]: $r_{arc} = r_{irc} + h_{rc} = 0.01$ m + 0.0026 m = 0.0126 m. Deviations from these geometric definitions (e.g.: aortic dilation) are mentioned explicitely in the ongoing sections.

E.3. Stresses and Strains at Rest

Table E.1 depicts stress and strain values at peak systole for each simulated aortic model without dissection. All values are calculated at the inner wall radius (inner radius in unloaded conditions: $r = r_i = 0.01$m), where circumferential and radial stresses have their maximum.

The ascending aortic pressure p_{asc} is substituted as maximum p_i in all calculations (please see section E.2 for fundamental considerations).

Quantity	**Non-Stenotic**	**Type 0 l.**	**Type 0 a.-p.**	**Type 1 L/R**
p_{asc}	16131	20531	17598	19998
σ_r	16131	20531	17598	19998
σ_θ	110906	169001	141425	164043
σ_z	47387	58809	57223	58578
σ_{res}	140043	180115	153574	175332
e_r	-0.2669	-0.2843	-0.2741	-0.2828
e_θ	0.2647	0.2816	0.2716	0.2801
e_z	-0.1245	-0.1333	-0.1281	-0.1325
h_{sys}	0.001765	0.001719	0.001746	0.001723
r_i	0.013010	0.013238	0.013103	0.013219

Table E.1.: Stress and strain values for non-stenotic fully open BAV model, type 0 lateral-ND model, type 0 anterior-posterior-ND model and Type 1 L/R-ND model at peak systole (t = 0.18 s). All stresses in [N/m^2 = Pa], strains in [m], pressures in [N/m^2 = Pa].

Table E.1 shows, that the unloaded wall thickness (h = 0.0026 m) at p = 0 mmHg decreases with increasing transmural pressure to a peak systolic (physiological) value of h_{sys} = 0.001719 m. The pathologic values of h are slightly lower. The resultant of the three principal stresses straining the arterial wall is σ_{res} = 140043 Pa in the physiological case, 180115 Pa in Type 0 lateral, 153574 Pa in Type 0 anterior-posterior and 175332 Pa in Type 1 L/R model. The location of maximum circumferential stress is found at r_i. Therefore, an initial tear is always located at the inner layer of the aorta (intima). Aortic tissue is known to withstand tensile stresses which are 8 times higher than physiologic stresses. Thence, stresses and strains computed for all three pathologic BAV models loaded with elevated transmural pressure resulting from peak systolic blood flow (physiologic blood pressure plus dynamic pressure from the jet) are far to low to directly disrupt the aortic wall. But since all preliminar results are based on aortic flow prediction using physiological boundary conditions at rest, transmural pressure in extreme exercise conditions probably boosts those stresses towards a critical level (see section 5.3). Additionally - even if only the pathologic pressure values in resting conditions are taken into account - these elevated stress and strain values burden the aortic wall every second, day in, day out. Like steel and aluminium used in mechanical engineering or special rubber mixtures used in highly pressurized wheels (up to a pressure of 10 bar = 1000000Pa) for high performance road bikes which are built to withstand a certain (high) amount of stress and strain, biological tissue (elastin, collagen, smooth muscle,...) weakens further and further in time when repeatedly loaded dynamically from minimum to maximum stress (see section ??).

E.4. Stresses and Strains in Exercise Conditions

If the same procedure of analytic structural analysis performed in section E.2 is applied on these new flow conditions, wall stresses at peak systole are found to be elevated approximately twofold (non-stenotic fully open BAV-EX model) and respectively 2.5-fold (Type 0 lateral-ND-EX model) in comparison with flow conditions at rest. What´s more, the ratio between σ_{res} in pathologic (Type 0 lateral model) exercise conditions and physiologic resting conditions is approximately 3.2. A numerical comparison of stress and strain values between non-stenotic fully open BAV (tl), Type 0 lateral-ND (tr), non-stenotic fully open BAV-EX (bl) and Type 0 lateral-ND-EX (br) is given in table E.2. The change in inner aortic radius and aortic wall thickness strongly decreases with increasing wall stress, since parallely the tissues Young´s modulus runs through a massive boost. This increase in arterial stiffness primarily is caused by straightening of collagen fibers at high stresses, which resist the applied load strongly (details to the nonlinear behavior of arterial walls can be found in section E.2 or [60] and [22]).

Quantity	**Non-Sten. Rest**	**Type 0 Rest**	**Non-Sten. Ex.**	**Type 0 Ex.**
p_{asc}	16131	20531	34251	52160
σ_r	16131	20531	34251	52160
σ_θ	110906	169001	286824	437751
σ_z	47387	58809	59946	59987
σ_{res}	140043	180115	295017	444922
e_r	-0.2669	-0.2843	-0.2915	-0.2917
e_θ	0.2647	0.2816	0.2884	0.2886
e_z	-0.1245	-0.1333	-0.1368	-0.1370
h_{sys}	0.001765	0.001719	0.001700	0.001699
r_i	0.013010	0.013238	0.013333	0.013336

Table E.2.: Stress and strain values at rest and exercise for non-stenotic fully open BAV model, type 0 lateral-ND model, non-stenotic fully open BAV-EX and type 0 lateral-ND-EX model at peak systole ($t = 0.18$ s). All stresses in [N/m^2 = Pa], strains in [m], pressures in [N/m^2 = Pa].

As all stress and strain values in table E.1 and table E.2 are gained from a self - developed unproofed analytic procedure (section E.2) with adapted Young´s moduli, by the aid of experimental data was made to assess partially verification. This was done by applying the analytic incremental calculation onto various published in vivo (echocardiographic assessment of aortic radius, wall thickness and elastic properties) and ex vivo (biaxial strength testing, inflation tests, FE simulations) experiments which depict the relations between transmural aortic pressure, circumferential and longitudinal stresses, strains, instantaneous aortic radii and aortic wall thickness. Inflation tests in the pig aortic root [61] for example (unloaded inner aortic radius $r_i = 11.64$ mm) yield mean inner aortic radii of $r_i = 14.38$ mm at a inner pressure of $p_i =$ 80-100 mmHg, $r_i = 15.4$ mm at $p_i =$ 100-150 mmHg and $r_i = 16.3$ mm at $p_i =$ 200-240 mmHg. Using the unloaded inner aortic radius from [61] to compute stresses and strains

with the self-developed procedure (unloaded wall thickness h = 0.003 mm) at 90 mmHg, 125 mmHg and 220 mmHg yields r_i = 14.50 mm, r_i = 15.25 mm and r_i = 15.6 mm respectively. In this case, measurements and calculation are compareable until a pressure of 200 mmHg is reached. At higher pressures, strains get underestimated by using Young´s modulus of collagen in the analytic calculations. Echocardiographic measurements of diastolic and systolic aortic radii in normal TAV patients and BAV patients in [64] gained diastolic radii of 11.9 mm, systolic radii of 13.75 mm in TAV patients and diastolic/systolic radii of 15 mm/16.3 mm in BAV patients. Diastolic values applied onto the calculation (unloaded wall thickness of h = 0.0025 mm for TAV and h = 0.002 mm for BAV) yields systolic radii of 13.2 mm in the TAV case and 16.25 mm in the BAV case. A second echocardiographic study [26] monitored diastolic/systolic aortic radius of 9.35 mm/10.85 mm and pressure (60 mmHg/102 mmHg) in a 26 year old patient with tricuspid aortic valve. Diastolic values applied onto the calculation yields systolic radii of 9.98 mm, indicating, that Young´s modulus used in the calculation is too high (overestimation of aortic wall stiffness) for modeling aortic wall behavior of very young patients with highly elastic arterial properties or unloaded aortic wall thickness is overestimated (but fits well in BAV patients, as the above mentioned example allows to suggest). Simulated circumferential Cauchy stress of about 300000 Pa in systole [66] (unloaded aortic radius: 14.2 mm, unloaded wall thickness: 2.57 mm, systolic pressure: 135 mmHg) fits the actual calculated value of 297911 Pa almost perfectly. These examples show, that the analytically found values of instantaneous stress, strain and aortic wall thickness fit experimental values gained out of stiffer (older patients) aortic specimen. In a certain range of patient age, stress values, aortic diameters and absolute strains yielded from the analytic incremental procedure are a reliable measure of the enormous burdens on aortic tissue in pathologic exercise conditions.

[28] reports failure stresses of aortic tissue in ex vivo tensile testing experiments of σ_{fail} = 2.04 MPa (approximately 18 times the physiologic systolic stress value at rest) in ascending aortic tissue taken out of younger patients (mean value of all patients younger than 55 years) and σ_{fail} = 1.35 MPa (approx. 12 times the physiologic value) in older patients (mean value of all patients older than 55 years). An older ex vivo tensile test [68] on passive human aortic tissue denotes dynamic (tests where carried out with a certain strain rate to model the periodic pumping action of the heart) failure stresses of σ^c_{fail} = 7 MPa (circumferential) and σ^l_{fail} = 3.2 MPa (longitudinal) for aortic tissue taken out of a 25 year old patient, σ^c_{fail} = 4.5 MPa (circumferential) and σ^l_{fail} = 2.8 MPa (longitudinal) (49 years old), σ^c_{fail} = 2.4 MPa (circumferential) and σ^l_{fail} = 2.8 MPa (longitudinal) (60 years old) and σ^c_{fail} = 1.9 MPa (circumferential) and σ^l_{fail} = 1.2 MPa (longitudinal) (87 years old). Quasistatic (very low strain rate) tensile tests in [62] yielded failure stresses which are approximately only half as those values gained from dynamic testing (quasistatic tests out of [62] are comparable with failure stresses out of [28]), indicating, that aortic tissue can burden higher stresses at dynamic physiologic strain rates than quasistatic tensil tests predict. No additional failure stress data of human aortic tissue was found during literature research.

Comparison of failure stresses in [28] and quasistatic failure stresses in [62] with maximum stresses out of the actual calculation done for Type 0 lateral-ND-EX model (see table E.2, failure stresses are 2.5- fold higher in older patients data and approx. 4 times higher in

younger patients data. Comparison with dynamic tests [62] predicts safety values against circumferential rupture (ratio between failure stresses versus maximum stresses gained from Type 0 model) of 9 for 25 year old patient, 5.6 (49 year old patient), It should be noticed, that above given ratios are slightly overestimated, since failure tests in [28] and [62] where carried out separately either in circumferential or in longitudinal direction. If aortic tissue (and certainly every other kind of tissue) is stressed by a combination of (high) circumferential and (lower) longitudinal stress (always the case in physiologic conditions), failure stress in circumferential direction will be decreased by a certain amount, which is dependent on the value of longitudinal stress. Nevertheless, direct rupture of healthy aortic tissue only because of a single heart beat in total pressures which arose from simulated BAV exercise conditions will most probably not occure in vivo (healthy aortic tissue in this sense means, that all failure characteristics of the aortic wall shown in [28] and [62] are referred to monitored systolic and diastolic pressure values with no additional dynamic pressure caused by a high velocity jet from severe stenotic bicuspid aortic valve). This holds true, even if the velocity jet (unchanged geometry of the aortic valve) acts on slightly dilated aortic geometry, e.g.: $r_i = 0.0145$m in unloaded configuration (taken from BAV patients younger than 55 years in [27], unloaded wall thickness: $h = 0.0028$ m), where stress values undergo a massive boost (maximum systolic stress value of pathologic Type 0 lateral-ND-EX model $\sigma_{res} \approx 800000$ Pa; results from younger patients where used to be comparable with the incremental law, since Young´s moduli data where taken from a younger patient). With respect to the physiologic reference model (non-stenotic fully open BAV at rest), stresses in Type 0 lateral-ND-EX model are increased approximately 9- fold. By the by, a thinner unloaded aortic wall ($h = 0.0021$ m, undilated aortic diameter) would have the same effect on aortic wall stress as above described aortic dilation.

Besides, stresses, instantaneous aortic radius and wall thickness calculated in [27] ($r_i = 0.023$ m, $h = 1.5$ mm, $\sigma_\theta = 237000$ Pa) for a systolic pressure of 121 mmHg can be predicted quite well within the incremental law used in this study ($r_i = 0.021$ m, $h = 1.59$ mm, $\sigma_\theta = 223275$ Pa). Additionally to physiologic systolic stress values at rest, maximum stress (peak systole) in Type 0 lateral-ND model (with dilated aortic geometry) at rest ($\sigma_\theta = 304271$ Pa at $p_{sys} = 154$ mmHg) is nearly twice as high than in undilated geometry (see table E.1) and approximately 3 times higher than σ_θ in the physiologic reference model.

The unpredictability of aortic dissection formation by means of the methods of instantaneous structural analysis (for one maximum pressure value of a single heart beat) illustrates the necessity of long life fatigue strength testing, to consider the effect of 70 heart beats per minute, 4200 per hour, 100800 each day, 36792000 per year and 1839600000 heart beats until an age of 50 years.

E.5. Methods of long Life Fatigue Strength Testing

In 50 years with bicuspid aortic valve disease with severe stenotic orifice area, the ascending aortic wall was burdened at least 1839600000 times with higher stresses (1.3 times higher in Type 0 lateral model with an inner ascending aortic radius of $r_i = 0.01$ m and even 2.2

times higher in Type 0 lateral model with dilated radius r_i = 0.0145 m) and strains shown in table E.1 as compared with the physiologic reference model (r_i = 0.01 m). As expected, appropriate experimental long life strength data for healthy and/or diseased ascending aortic tissue could not be found in literature. In such a test, aortic tissue would have to be exposed to dynamic oscillating internal pressure several days or weeks to mimic the pulsatile pumping action of the heart. In mechanical engineering, long life fatique strength testing of steel (as an illustrative example) yields (depending on the experimental setup) on one hand the maximum stress, which the material barely withstands during a dynamic oscillating charge of at least 10^7 repeatings until it finally breaks and on the other hand the weakening of the material during oscillating charge in terms of decreasing absolute failure stress. Partially, the second kind of information can be extracted from [28] and [62], since therein, failure stress values of aortic tissue are obtained from aortas out of patients with a broad range of age. Clearly, this kind of data is not of the same uniqueness and reliability as strength testing data gained from experiments with one single geometrically and structurally well defined peace of steel, but it may serve as a guiding example (which should be handled with care), how aortic tissue weakens further and further each single heart beat. As mentioned in section 5.3, dynamic circumferential failure stresses [62] are σ^c_{fail} = 7 MPa for aortic tissue taken out of a 25 year old patient, σ^c_{fail} = 4.5 MPa (49 years old), σ^c_{fail} = 2.4 MPa (60 years old) and σ^c_{fail} = 1.9 MPa (87 years old) for physiologic conditions (diastolic/systolic arterial pressure 80/120 mmHg). These values can be substituted into a diagram of failure stress (ordinate) versus age (abscissa). Before the age of 25 (first assessable experimental data point) and back to the day of birth, failure stress is linearly continued from σ^c_{fail} = 7 MPa (25 years) with the same slope as between 25 years and 49 years. As for the lack of further experimental data points, the same (linear continuation from 87 years till latest observed death of a person in physiologic conditions) must be done for the time between 87 and approximately 130 years (arbitrary assumption). This procedure yields failure stresses of approximately σ^c_{fail} = 9.8 MPa at the day of birth and 1 MPa at an age of 130 years. This curve represents aortic failure stresses for the reference physiologic systolic stress value of σ_{res} = 140043 Pa (see table E.1). A second requirement to finally obtain estimated failure stress values for the pathologic case with boosted transmural pressure and/or dilated aortic geometry for each year is a function of reference. Assuming, that with zero transmural pressure values (zero pressure means zero stresses and strains) from birth to death, the aortic tissue would not weaken at all, the reference curve is a horizontal line (σ^0_{fail} = 9.8 MPa from birth to death). According to that, failure stress values for the pathologic cases (σ^{pat}_{res} = 180115 Pa for Type 0 lateral-ND with r_i = 0.01 m and σ^{pat}_{res} = 304271 Pa for Type 0 lateral-ND with r_i = 0.0145 m) can be obtained by following formula:

$$\sigma^{pat}_{fail} = \sigma^0_{fail} - \frac{\sigma^0_{fail} - \sigma^c_{fail}}{\sigma_{res}} \sigma^{pat}_{res} \tag{E.34}$$

Consequently, σ^{pat}_{fail} for σ^{pat}_{res} = 180115 Pa at an age of 25 years is 6.2 MPa, at 49 years 3.1 MPa, 0.28 MPa at an age of 60 years and (virtually) -0.36 MPa at 87 years. Intimal rupture occurs, if the failure stress deceeds the residual aortic wall stress σ^{pat}_{res} = 180115 Pa. The year (a_{AD}) when an intimal tear occures and the aortic dissection (AD) begins to develop,

can be predicted by linear interpolation ($x = \Delta x(y-d)/\Delta y$) of failure stresses between 60 ($\sigma^{pat}_{fail}(60)$) and 87 ($\sigma^{pat}_{fail}(87)$) years:

$$a_{AD} = a_0 + \Delta a \frac{\sigma^{pat}_{res} - \sigma^{pat}_{fail}(60)}{(\sigma^{pat}_{fail}(60) - \sigma^{pat}_{fail}(87))} \tag{E.35}$$

With Δa = -27 years and a_0= 60 years, the intimal tear occurs at an age of 64.21 years, which is slightly above the age where aortic dissections most frequently occur (see section 3.2.2).

σ^{pat}_{fail} for σ^{pat}_{res} = 304271 Pa at an age of 25 years is 3.7 MPa, at 49 years (virtually) -1.5 MPa. This leads to an intimal tear in pathologic Type 0 lateral BAV in combination with aortic dilatation at an age of 34.33 years.

At this juncture, the above derived absolute results should be relativized, since they predict aortic dissection in every single person with semi- severe arterial hypertrophy at an age of 64.21 or 34.33 years, respectively. This would clearly be a fatal overestimation of the true yearly incidence of this disease (see section 3.2.2. By definition, a model as it was used to derive the actual stress and strain values in this study cannot give absolute values as they are found in physiologic conditions. Besides all assumtiones which where made in the CFD process concerning the aortic geometry, wall behavior and many others (section 4.2), calculated stress and strain values are based on application of a stepwise linear elasticity theory on a straight, thick- walled cylindrical tube without any further surroundings. The same is true for ex vivo experimental data used to validate calculated stresses and strains and to obtain failure stress values of aortic tissue. Both, calculation and experiments neglect the additional active stress response of smooth muscle cells, which act against a dilation due to transmural pressure in physiologic conditions. The effect of this active response on aortic tissue is a less dominant increase in strain, which goes hand in hand with lower residual stresses and a less dominant decrease of aortic wall thickness. What´s more, both methods neglect the additional support and integrity of connective tissue surrounding the aorta inside the human body. How big the sum of discrepancies may be, could not be assessed within the study and the preliminary literature research and should be one of the major objectives in future studies.

Appart from this relativation, the CFD model in combination with structural analysis served as a tool to gain more insight in a complex disease. Rather relying on relative tendencies and ratios between physiologic and pathologic conditions than accounting too much on above derived absolute values, sections 5.2, 5.3 and **??** may illustrate some causes of aortic diseases appart from the controversal discussion concerning the role of altered hemodynamics and/or histologic causes of aortic dilation, aneurysm formation and dissection formation.

There are some major diseases and their formations which partially can be explained by the preliminary sections:

- Aortic dissections in bicuspid aortic valve disease with severe valve stenosis without aortic dilation are mainly caused by further and further weakening of aortic tissue during repeated exposure to altered transmural pressure (high velocity jet). The highest boosts in transmural pressure on the ascending aortic wall can be observed in Type 0 lateral and Type 1 L/R BAV models, exposing the patient to a higher risk of DeBakey

Type 1 aortic dissection than in Type 0 anterior-posterior BAV. The intimal rupture and a further propagation of dissection downstream often is orientated in circumferential direction (perpendicular to the flow, see section 3.2.2). Intuitively, an intimal tear should develope in longitudinal direction, like it can be observed in sausages boiled in hot water (there, longitudinal stress is approximately half as high as circumferential stress). The main difference in stress-strain-behavior between sausages and arteries is caused by anisotropy of arterial tissue. The total failure stress of aortic tissue in circumferential direction ist twice as high as in longitudinal direction (most probably, the walls of sausages are distinguished with an isotropic characteristic). If longitudinal stress is half of circumferential stress and the longitudinal failure stress is more than a half time smaller than that in circumferential direction, intimal rupture will develope in circumferential direction. Consequently, longitudinal rupture should be more likely in the actual pathologic models, since circumferential stresses are approximately three times higher than their longitudinal counterpart. According to this idea, circumferential rupture should be more likely in dilated aortic tissue in combination with normally functioning valves. There, longitudinal stresses at physiologic systolic blood pressures are approximately half of circumferential ones.

- Bicuspid aortic valve patients with severe valve stenosis and aortic dilation are exposed to a far higher risk of aortic dissection.

- As noted in section 5.2, severe stenotic BAV boosts transmural pressure at the ascending aortic wall up to a value found in hypertrophic patients. Hypertrophy is found appart from stenotic valve and BAV disease in normally sized and dilated ascending aortas. Hypertrophy is discussed to be the most important factor causing AD (see section 3.2.2). From stress and strain analysis and the weakening behavior of aortic tissue it becomes clear, that this is mainly due to slightly increased wall stress acting over years.

- Depending on how much the outer layers of the ascending aorta where weakened and injured during the long lasting burden, ascending aortic aneurysm (AAA) may occure as an alternative disease to AD. Most probably it depends on the intrinsic structure of different aortic layers and the way, how pressure acts on the arterial wall weather AD propagates without aneurysm formation, AAA developes without intimal rupture or a combination of both diseases takes place (dissecting aortic aneurysm). From a mechanical standpoint, high longitudinal wall stress with respect to circumferential stress will promote aortic dissection (with a tear most likely in circumferential direction), high circumferential stress (caused by locally altered hemodynamics) in combination with lower longitudinal stress ascending aortic aneurysm (because circumferential stress tends to blow up a tube and longitudinal stress tends to tear it appart). Mechanically, a combination of both diseases (dissecting aortic aneurysm) seams very likely in arteries with normally functioning BAV or TAV (without velocity jet), where structural weakening caused by altered transmural pressure lead to intimal rupture. Intimal rupture always leads to a local increase of stress (see [16] or every standard textbook on stress and strain analysis), which thereafter blows up the artery.

The cause of each disease (AD, AAA, dissecting aortic aneurysm) may be various. Weather in BAV and aortic dilation coexist without altered hemodynamics, in aortic dilation causally caused by stenotic orifice area or intrinsic histologic malformations of the aortic wall or in aortic dilation in normally functioning or stenotic tricuspid aortic valves, arterial hypertrophy and many others more, the determining process is always (the more or less rapid) weakening of arterial tissue driven by physical and physiological parameters (aortic diameter, wall thickness, pressure, Young´s modulus, tensile strength, active cell remodeling, smooth muscle behavior, strain rate,...) which variantly are predefined by histologic abnormalities and/or causally caused by altered pulsatile blood flow.

Bibliography

[1] Paul W.M. Fedak, Subodh Verma, Tirone E. David, Richard L. Leask, Richard D. Weisel and Jagdish Butany. Clinical and Pathophysiological Implications of a Bicuspid Aortic Valve. *Circulation* 106:900-904, 2002.

[2] C. Ward. Clinical significance of the bicuspid aortic valve. *Heart* 83:81-85, 2000.

[3] Nikolaos Tzernos, Judith Therrien, James Yip, et al. Outcomes in Adults With Bicuspid Aortic Valves. *JAMA* 300(11):1317-1325, 2008.

[4] Heynric B. Grotenhuis, Jaap Ottenkamp, Jos J.M. Westenberg, Jeroen J. Bax, Lucia J.M. Kroft, and Albert de Roos. Reduced Aortic Elasticity and Dilatation Are Associated With Aortic Regurgitation and Left Ventricular Hypertrophy in Nonstenotic Bicuspid Aortic Valve Patients. *J. Am. Coll. Cardiol.* 49:1660-1665, 2007.

[5] Nuran Yener, G. Levent Oktar, Dilek Erer, M. Murat Yardimci and Ali Yener. Bicuspid Aortic Valve. *Ann Thorac Cardiovasc Surg* 8:264-267, 2002.

[6] Anja Kumme. *Klassifikation bikuspider Aortenklappen*. Inauguraldissertatioin, Universität zu Lübeck, 2007.

[7] Hans-H. Sievers and Claudia Schmidtke. A classification system for the bicuspid aortic valve from 304 surgical specimens. *The Journal of Thoracic and Cardiovascular Surgery* 133: 1226-1233 , 2007.

[8] Alex J. Barker, Craig Lanning and Robin Shandas. Quantification of Hemodynamic Wall Shear Stress in Patients with Bicuspid Aortic Valve Using Phase-Contrast MRI. *Annals of Biomedical Engineering* 3: 788-800, 2010.

[9] Matthias Bauer, Henryk Siniawski, Miralem Pasic, Beate Schaumann and Roland Hetzer. Different Hemodynamic Stress of the Ascending Aorta Wall in Patients with Bicuspid and Tricuspid Aortic Valve. *J Card Surg* 21: 218-220 , 2006.

[10] Mauro Paes Leme, Tirone E. David, Jagdish Butany, Diponkar Banerjee, Eduardo S. Bastos, Sylvio C. Provenzano, Leoncio A. Feitosa, Henrique Murad and Monica M. Ferreira Magnanini. Molecular evaluation of the

great vessels of patients with bicuspid aortic valve disease. *Rev Bras Cir Cardiovasc* 18(2): 148-156 , 2003.

[11] Diana Bonderman, Elisabeth Gharehbaghi-Schnell, Gregor Wollenek, Gerald Maurer, Helmut Baumgartner and Irene M. Lang. Mechanisms Underlying Aortic Dilatation in Congenital Aortic Valve Malformation. *Circulation* 99: 2138-2143 , 1999.

[12] Mauro de Sa, Yaron Moshkovitz, Jagdish Butany and Tirone E. David. Histologic Abnormalities of the Ascending Aorta and Pulmonary Trunk in Patients with Bicuspid Aortic Valve Disease: Clinical Relevance to the Ross Procedure. *Thoracic and Cardiovascular Surgery* 118: 588-596 , 1999.

[13] P. Martijn den Reijer, Denver Sallee III, Petra van der Velden, Eline R. Zaaijer, W. James Parks, Senthil Ramamurthy, Trevor Q. Robbie, Giorgina Donati, Carey Lamphier, Rudolf P. Beekman, Marijn E. Brummer. Hemodynamic predictors of aortic dilatation in bicuspid aortic valve by velocity-encoded cardiovascular magnetic resonance. *Journal of Cardiovascular Magnetic Resonance* 12:4 http://www.jcmr-online.com/content/12/1/4, 2010.

[14] Martin G. Keane, Susan E. Wiegers, Ted Plappert, Alberto Pochettino, Joseph E. Bavaria and Martin G. St. John Sutton. Bicuspid Aortic Valves Are Associated With Aortic Dilatation Out of Proportion to Coexistent Valvular Lesions. *Circulation* 102: III-35-III-39 , 2000.

[15] Michael D. Hope, Thomas A. Hope, Alison K. Meadows, Karen G. Ordovas, Thomas H. Urbania, Marcus T. Alley, Charles B. Higgins. Bicuspid Aortic Valve: Four-dimensional MR Evaluation of Ascending Aortic Systolic Flow Patterns. *Radiology* 1: 53-61, 2010.

[16] Mano J. Thubrikar. *Vascular Mechanics and Pathology*. Springer Science+Business Media, 2007.

[17] R. Erbel (Chairman), F. Alfonso, C. Boileau, O. Dirsch, B. Eber, A. Haverich, H. Rakowski, J. Struyven, K. Radegran, U. Sechtem, J. Taylor, Ch. Zollikofer. Internal reviewers: W. W. Klein, B. Mulder and L. A. Providencia. Diagnosis and management of aortic dissection. *European Heart Jornal* 22: 1642-1681, 2001.

[18] Barbara Theresia Weis-Müller, Olga Modlich, Irina Drobinskaya, Derya Unay, Rita Huber, Hans Bojar, Jochen D. Schipke, Peter Feindt, Emmeran Gams, Wolfram Müller, Timm Goecke and Wilhelm Sandmann. Gene expression in acute Stanford type A dissection: a comparative microarray study. *Journal of Translational Medicine* 4:29, 2006.

[19] Katarzyna J. Macura, Frank M. Corl, Elliot K. Fishman, David A. Bluemke. Pathogenesis in Acute Aortic Syndromes: Aortic Dissection, Intramural Hematoma, and Penetrating Atherosclerotic Aortic Ulcer. *AJR* 181: 309-316 , 2003.

[20] Keshava Rajagopal, Craig Bridges, K.R. Rajagopal. Towards an understanding of the mechanics underlying aortic dissection. *Biomechan Model Mechanobiol* 6: 345-359, 2007.

[21] Y.C. Fung. *Biomechanics: Mechanical Properties of Living Tissues*. Springer-Verlag, New York, Berlin, Heidelberg, 1993.

[22] W. Milnor. *Hemodynamics*. Williams Wilkins, 1982.

[23] Herbert Mang, Günter Hofstetter. *Festigkeitslehre*. Springer-Verlag, Wien, New York, 2004.

[24] Heinz Parkus. *Mechanik der festen Körper*. Springer-Verlag, Wien, New York, 2005.

[25] Gerhard A. Holzapfel, Ray W. Ogden. Biomechanical Modelling at the Molecular, Cellular and Tissue Levels. In *CISM Courses and Lectures*, 508, pages 259-344 . International Centre for Mechanical Sciences, 2009.

[26] RM Lang, BP Cholley, C Korcarz, RH Marcus and SG Shroff . Measurement of regional elastic properties of the human aorta. A new application of transesophageal echocardiography with automated border detection and calibrated subclavian pulse tracings. *Circulation* 90: 1875-1882 , 1994.

[27] Ruth J. Okamoto, Haodong Xu, Nicholas T. Kouchoukos, Marc R. Moon and Thoralf M. Sundt, III. The influence of mechanical properties on wall stress and distensibility of the dilated ascending aorta. *J Thorac Cardiovasc Surg* 126: 842-850, 2003.

[28] RUTH J. OKAMOTO, JESSICA E. WAGENSEIL, WILLIAM R. DELONG, SARA J. PETERSON, NICHOLAS T. KOUCHOUKOS and THORALF M. SUNDT III. Mechanical Properties of Dilated Human Ascending Aorta. *Annals of Biomedical Engineering* 30: 624-635, 2002.

[29] Franz Durst. *Grundlagen der Strömungsmechanik*. Springer Berlin Heidelberg New York, 2006.

[30] Stephan Meyer. *Numerische Simulation der Strömung im Aortenbogen*. PhD thesis, Universität Karlsruhe, 2003.

[31] Eli J. Weinberg, Mohammad Reza Kaazempur Mofrad. Transient, Three-dimensional, Multiscale Simulations of the Human Aortic Valve. *Cardiovascular Engineering* DOI 10.1007/s10558-007-9038-4.

[32] Kenneth Reid. The anatomy of the sinus of Valsalva. *Thorax* 25: 79-85, 1970.

[33] Eli J. Weinberg and Mohammad R. Kaazempur Mofrad. A multi-scale computational comparison of the bicuspid and tricuspid aortic valves in relation to calcific aortic stenosis. *Journal of Biomechanics* doi:10.1016/j.jbiomech.2008.08.006, 2008.

[34] Catherine M. Otto. Valvular Aortic Stenosis: Disease Severity and Timing of Intervention. *J. Am. Coll. Cardiol.* 47: 2141-2151, 2006.

[35] Thomas T. Tsai, Christoph A. Nienaber and Kim A. Eagle. Acute Aortic Syndromes. *Circulation* 112: 3802-3813 , 2005.

[36] J.H. Ferziger, M. Peric. *Computational Methods for Fluid Dynamics*. Springer, Berlin Heidelberg New York, 2002.

[37] http://my.fit.edu/itresources/manuals/fluent6.3/help/html/ug/node1.htm (07.04.2011).

[38] Richard Feynman. *The Feynman Lectures on Physics*. Pearson Addison Wesley, 2006.

[39] Wolfgang Demtröder. *Experimentalphysik 1*. Springer, Berlin Heidelberg New York, 2004.

[40] Bruce R. Munson, Donald F. Young, Theodore H. Okiishi and Wade W. Huebsch. *Fundamentals of Fluid Mechanics*. Wiley, John Wiley Sons, 2010.

[41] Mette S. Olufsen, Charles S. Peskin, Won Yong Kim and Erik M. Pedersen, Ali Nadim and Jesper Larsen. Numerical Simulation and Experimental Validation of Blood Flow in Arteries with Structured-Tree Outflow Conditions. *Annals of Biomedical Engineering* 28: 1281-1299 , 2000.

[42] Benny Lautrup. *Physics of continous matter*. Taylor Francis, 2004.

[43] http://www.claymath.org/millennium/Navier-StokesEquations/navierstokes.pdf (06.04.2011).

[44] S Laurent, X Girerd, JJ Mourad, P Lacolley, L Beck, P Boutouyrie, JP Mignot and M Safar. Elastic modulus of the radial artery wall material is not increased in patients with essential hypertension. *Arterioscler Thromb Vasc Biol* 14: 1223-1231 , 1994.

[45] Ernst Mutschler, Hans-Georg Schaible, Peter Vaupel. *Anatomie Physiologie Pathophysiologie des Menschen*. Wissenschaftliche Verlagsgesellschaft mbH, Stuttgart, 2007.

[46] Heinz Herwig. *Strömungsmechanik: Einführung in die Physik von technischen Strömungen*. Vieweg+Teubner, 2008.

[47] J.R. Womersley. Method for the Calculation of Velocity, Rate of Flow and Viscous Drag in Arteries when the Pressure Gradient is known. *Journal of Physiology* 127: 553-563 , 1955.

[48] http://my.fit.edu/itresources/manuals/fluent6.3/help/html/ug/node985.htm (07.04.2011).

[49] TORSTEN SCHENKEL, MAURO MALVE, MICHAEL REIK, MICHAEL MARKL, BERND JUNG and HERBERT OERTEL. MRI-Based CFD Analysis of Flow in a Human Left Ventricle: Methodology and Application to a Healthy Heart. *Annals of Biomedical Engineering* 3: 503-515, 2009.

[50] Gerard J. Tortora and Bryan Derrickson. *Principles of Anatomy and Physiology*. Wiley, John Wiley Sons, 2009.

[51] Xiao Liu, Fang Pu, Yubo Fan, Xiaoyan Deng, Deyu Li and Shuyu Li. A numerical study on the ?ow of blood and the transport of LDL in the human aorta: the physiological significance of the helical flow in the aortic arch. *Am J Physiol Heart Circ Physiol* 297: H163-H170, 2009.

[52] ARMIN LEUPRECHT, SEBASTIAN KOZERKE, PETER BOESIGER and KARL PERKTOLD. Blood flow in the human ascending aorta: a combined MRI and CFD study. *Journal of Engineering Mathematics* 47: 387-404 , 2003.

[53] Francesca Viscardi, Christian Vergara, Luca Antiga, Sabrina Merelli, Alessandro Veneziani, Giovanni Puppini, Giuseppe Faggian, Alessandro Mazzucco, and Giovanni Battista Luciani. Comparative Finite Element ModelAnalysis of Ascending Aortic Flow in Bicuspid and Tricuspid Aortic Valve. *Artificial Organs* doi:10.1111/j.1525-1594.2009.00989.x.

[54] N. Shahcheraghi, H. A. Dwyer, A. Y. Cheer, A. I. Barakat and T. Rutaganira. Unsteady and Three-Dimensional Simulation of Blood Flow in the Huma Aorti Arch. *Journal* 124: 378-387 , 2002.

[55] Dinesh Mohan and John W. Melvin. Failure Properties of Passive Human Aortic Tissue. I-Uniaxial Tension Tests. *Journal of Biomechanics* 11: 887-902 , 1982.

[56] Gerhard A. Holzapfel. Determination of material models for arterial walls from uniaxial extension tests and histological structure. *Journal of Theoretical Biology* 238: 290-302 , 2006.

[57] L. Segadal and K. Matre. Blood velocity distribution in the human ascending aorta. *Circulation* 76: 90-100 , 1987.

[58] PJ Kilner, GZ Yang, RH Mohiaddin, DN Firmin and DB Longmore. Helical and retrograde secondary flow patterns in the aortic arch studied by three-directional magnetic resonance velocity mapping. *Circulation* 88: 2235-2247 , 1993.

[59] Michael D. Hope, Thomas A. Hope, Alison K. Meadows, Karen G. Ordovas, Thomas H. Urbania, Marcus T. Alley and Charles B. Higgins. Bicuspid Aortic Valve: Four-dimensional MR Evaluation of Ascending Aortic Systolic Flow Patterns. *Radiology* 1: 53-61 , 2010.

[60] Gerhard A. Holzapfel, Ray W. Ogden. Biomechanics of Soft Tissue in Cardiovascular Systems. In *CISM Courses and Lectures*, 441, International Centre for Mechanical Sciences, 2003.

[61] Martins Kalejs and Ludwig Karl von Segesser. Rapid prototyping of compliant human aortic roots for assessment of valved stents. *Interact Cardio Vasc Thorac Surg* 8: 182-186 , 2009.

[62] Dinesh Mohan and John W. Melvin. Failure Properties of Passive Human Aortic Tissue. II-Uniaxial Tension Tests. *Journal of Biomechanics* 1: 31-44 , 1983.

[63] Brian M. Learoyd and Michael G. Taylor. Alterations with Age in the Viscoelastic Properties of Human Arterial Walls. *Circulation Research* 18: 278-292 , 1966.

[64] Stefano Nistri, Jane Grande-Allen, Marianna Noale, Cristina Basso, Paola Siviero, Stefania Maggi, Gaetano Crepaldi, and Gaetano Thiene. Aortic elasticity and size in bicuspid aortic valve syndrome. *European Heart Journal* 29: 472-479 , 2008.

[65] Martin Czerny. One-on-one interview at the Center of Medical Physics and Biomedical Engineering, Medical University Vienna, Austria, 2010.

[66] Ajay Bohra, Thoralf M. Sundt and Ruth J. Okamoto. Three-Dimensional Finite Element Modeling of Dilated Human Ascending Aorta. 1215-1216, 2002.